

Biomechanical Modeling of the Human Heart

Modeling of the Ventricles, the Atria and the
Pericardium and the Inverse Problem of Cardiac
Mechanics

Zur Erlangung des akademischen Grades eines

DOKTOR-INGENIEURS

von der Fakultät für

Elektrotechnik und Informationstechnik

des Karlsruher Instituts für Technologie (KIT)

genehmigte

DISSERTATION

von

Dipl.-Phys. Thomas Fritz

geb. in Heidelberg

Tag der mündlichen Prüfung:	11. Februar 2015
Referent:	Prof. Dr. rer. nat. Olaf Dössel
Korreferent:	Assoz. Prof. Priv.-Doz. Dipl.-Ing. Dr.techn. Gernot Plank

Contents

1	Introduction	1
1.1	Structure of the Thesis	2
<hr/>		
I	Fundamentals	5
<hr/>		
2	Anatomy and Physiology of the Human Heart	7
2.1	The Human Heart	7
2.2	The Cardiac Cycle	9
2.3	Electrial Excitation and Excitation Propagation	10
3	Modeling of Cardiac Electrophysiology and Tension Development	15
3.1	Introduction	15
3.2	Modeling Electrophysiology of Cardiac Cells	15
3.3	Modeling of the Active Tension Development: The Hybrid model by Sachse, Glaenzel and Seemann	17
3.4	Modeling of Cardiac Excitation Propagation: Bidomain Model and Monodomain Simplification	18
3.5	The Electrophysiological Simulation Framework <i>acCELLerate</i>	20
4	Modeling of the Circulatory System	21
5	Nonlinear Continuum Mechanics	23
5.1	Basic Principles of Nonlinear Continuum Mechanics	23

6	Finite Element Analysis	31
6.1	Finite Element Method for Nonlinear Continuum Me- chanics	31
7	Constitutive Models of Cardiac Tissue	39
8	Recent Developments in Electromechanical Modeling of the Heart	41
<hr/>		
II	Methods	45
<hr/>		
9	The Biomechanical Simulation Framework	47
10	Geometrical Model of the Heart	51
11	Modeling of the Electrical Activation and Active Tension Development	55
12	Implementation of the Solver	59
12.1	Parallelization and Domain Decomposition	59
12.2	The Biomechanical Solver	59
13	Implementation of the Circulatory System Model	65
13.1	Modeling of the Intraventricular Pressure	65
13.2	Modeling of Atrial Pressure	69
13.3	Initialization of the Circulatory System model	70
14	Implementation of the Contact Handling	73
15	The Inverse Solver	79
15.1	Introduction	79
15.2	The Algorithm of the Inverse Solver	80
<hr/>		
III	Projects	89
<hr/>		
16	Validation of the Biomechanical Simulation Framework	91
16.1	Validation	91

16.2 Mechanical Benchmark	101
16.3 Discussion	101
17 The Beating Heart within the Pericardium	103
17.1 Introduction	103
17.2 Methods	105
17.3 Simulation and Evaluation	107
17.4 Results	108
17.5 Discussion	112
17.6 Limitations	120
17.7 Future work	121
18 Biomechanical Modeling of the Human Atria	123
18.1 Introduction	123
18.2 Methods	126
18.3 Results	131
18.4 Discussion	136
18.5 Limitations	141
18.6 Future work	142
19 Reconstruction of Left Ventricular Active Tension	143
19.1 Introduction	143
19.2 Methods	145
19.3 Results	147
19.4 Discussion	153
19.5 Limitations	155
19.6 Outlook	156
20 Summary and Conclusions	167
Bibliography	173
List of Publications and Supervised Thesis	187

Chapter 1

Introduction

The development of computers, which become faster and faster and further the development of modern numerical mathematical techniques have let computational modeling become one of the most important tools for science and engineering, which allows to get a better insight into natural mechanisms and processes and moreover to make predictions about them. In science, computational models are used to design and to predict the outcome of experiments and to explain the observations. In engineering, computational model are used during the development and for testing and optimization, e.g. of new cars or airplanes.

The topic of this work is the computational modeling of the human heart with focus on cardiac biomechanics. Cardiac modeling has two main objectives: First, to get a better understanding of the mechanisms of the cardio-vascular system. Here, it can help to improve the understanding of the physiological processes of the heart and moreover, to gain a better insight into cardiac pathologies and their underlying mechanisms. Second, personalized modeling of the heart can be a valuable tool for the cardiologist and support him with diagnosis and treatment planning.

In the course of this work, I have developed and implemented a biomechanical simulation framework which allows to simulate the contraction of the whole human heart. The biomechanical model is based on a continuum mechanical approach using finite element analysis. Input is the active tension development of the myocardium, which is provided by an already

existing multi-scale electrophysiological simulation environment. This had been developed over the last decade at the Institute of Biomedical Engineering at the Karlsruhe Institute of Technology (KIT) and allows to simulate the cardiac electrophysiology on cellular level, the excitation propagation and the active tension development within the myofibrils. Based on this active tension distribution over time, the new biomechanical simulation framework calculates for each time step the corresponding deformation of the heart. Furthermore, the simulation framework contains an inverse solving algorithm (inverse solver), which works in an opposite manner and allows to reconstruct the active tension distribution from provided data of the motion of the heart surfaces, which can for example be extracted from medical imaging data. This allows for a personalization of the model based on clinical data.

This thesis is structured into three parts. The first gives a short summary of the basic fundamentals of anatomy and physiology, nonlinear continuum mechanics and the finite element method as well as of the aspects of cardiac modeling which are related to this work. The second part explains the biomechanical simulation framework and the developed methods. The third part presents the validation of the simulation framework and three selected projects, which had been conducted in context of this thesis. The first project is the simulation of the whole heart and the analysis of the interaction of the ventricles with the atria and of the whole heart with the pericardium. The second project deals with the electromechanical modeling of the atria and analyzes the impact of different ablation scars in the atria on the pumping function of the heart. The third project evaluates the active tension reconstruction algorithm using synthetic data of the motion of the endocardial surfaces, obtained from the simulation of a healthy heart and from simulations with different infarction scar areas in the left ventricle. In the following, the structure of the thesis is given:

1.1 Structure of the Thesis

Part I - Fundamentals

- **Chapter 2** gives an overview of the cardiac anatomy and physiology.

- **Chapter 3** outlines basic aspects of modeling of the cardiac electrophysiology and the active tension development.
- **Chapter 4** briefly deals with the modeling of the circulatory system.
- **Chapter 5** summarizes the basic fundamentals of nonlinear continuum mechanics.
- **Chapter 6** describes how the partial differential equations of continuum mechanics can be handled numerically using the finite element methods.
- **Chapter 7** explains how the mechanical properties of cardiac tissue can be described with a mathematical model.
- **Chapter 8** gives a short overview of the recent publications in the field of electromechanical modeling and parameter estimation techniques for model personalization

Part II - Methods

- **Chapter 9** describes the structure of the biomechanical simulation framework.
- **Chapter 10** explains how the geometrical models were generated.
- **Chapter 11** gives a short summary of the used methods for the electromechanical modeling.
- **Chapter 12** explains the implementation of the biomechanical solvers based on the finite element analysis.
- **Chapter 13** describes the circulatory system model based on a Windkessel model which is strongly coupled with the biomechanical solvers.
- **Chapter 14** gives a description of the contact handling algorithm which is used to model the contact of the heart with the pericardium.
- **Chapter 15** explains the inverse solver which allows to reconstruct the active tension distribution of the heart from the motion of the heart surfaces.

Part III - Projects

- **Chapter 17** presents the validation of the biomechanical simulation framework.
- **Chapter 18** presents the analysis of the interaction of the ventricles with the atria and of the whole heart with the pericardium.
- **Chapter 19** presents the analysis of the impact of ablation scars in the left atrium on the heart performance.
- **Chapter 20** presents the evaluation of the inverse solver using synthetic data of the motion of the endocardial surfaces obtained from a simulation of a healthy heart and three simulations of a heart with different infarction scar areas.

Remark: All figures in this work were created by the author. Some figures were inspired by the work of others, here the source of inspiration is given in the caption.

PART I

FUNDAMENTALS

Chapter 2

Anatomy and Physiology of the Human Heart

2.1 The Human Heart

The job of the human heart is to pump blood through the body. Hereby, oxygen is transported from the lungs to all cells of the body and at the same time carbon dioxide is transported back to the lungs. Moreover, nutrients, hormones, metabolites, body cells and other blood components are transferred between the different organs. The heart consists of four chambers (Fig. 2.1): the left and right ventricle and the left and right atrium. These are connected via the heart valves. The tricuspid valve is located between the right atrium and the right ventricle and the mitral valve between left atrium and left ventricle. The right atrium is connected with the superior vena cava and the inferior vena cava. The left atrium is connected with the left pulmonary veins. The right ventricle is connected with the pulmonary artery via the pulmonary valve and the left ventricle is connected with the aorta via the aortic valve (Martini et al., 2011, ch. 20, fig. 20-6, p. 676). The heart wall consists of three different layers: the epicardium which covers the outer surface of the heart, the myocardium which mainly consists of muscle tissue and the endocardium which covers the inner surface of the heart (Martini et al., 2011, ch. 20, p. 673). The cardiac muscle fibers in the ventricles are arranged as "counter-wound

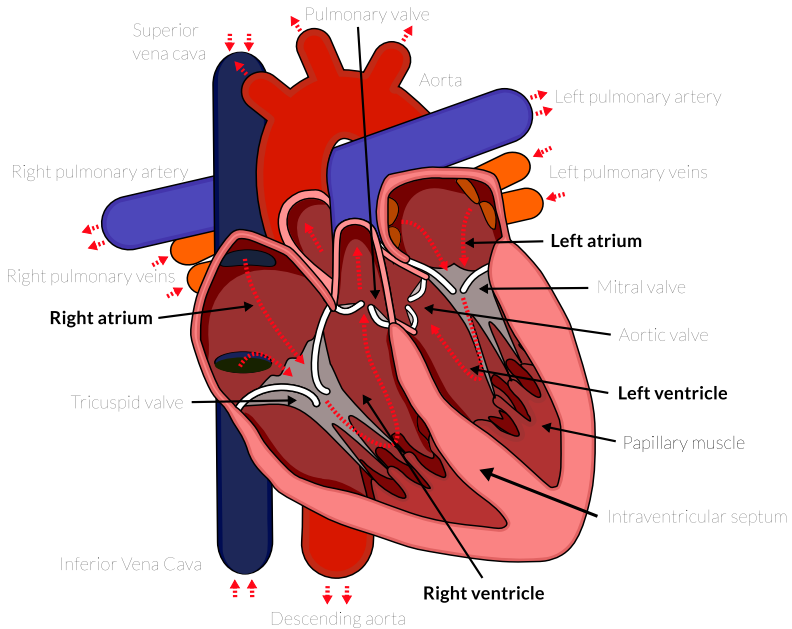


Figure 2.1: Visualization of the human heart, with the atria, ventricles, valves and vessels

helices encircling the ventricular cavities”(Eggen and Swingen, 2009, ch. 20, p. 349), while the fiber orientation depends on its location within the heart wall (Streeter, 1979; Nielsen et al., 1991). The fibers are arranged in sheets and bound together by endomysial collagen, while the sheets themselves are coupled by perimysial collagen (Smaill and Hunter, 1991). This cardiac microstructure is responsible for the anisotropic mechanical properties of cardiac tissue.

The Pericardium

The heart is enclosed by the pericardium. This is composed of two separate layers: the epicardium, also named *visceral pericardium*, which, as mentioned above, covers the outer surface of the heart and the *parietal*

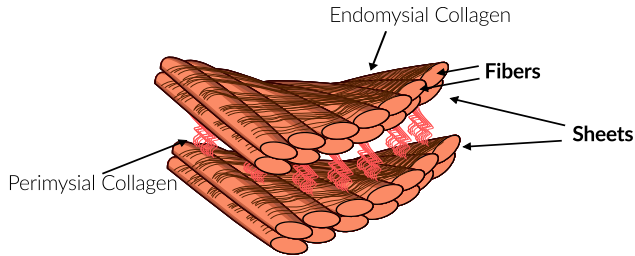


Figure 2.2: Cardiac microstructure: The fibers are arranged in sheets, bound by endomysial collagen. Perimysial collagen couples the sheets (inspired by (Hunter et al., 1997b, sec. 6.2.2, fig. 6.3, p. 176))

pericardium. The space between these two layers is the pericardial cavity, which is filled with the pericardial fluid. The pericardial fluid allows an almost frictionless sliding of these two layers of the pericardium on each other (Martini et al., 2011, ch. 20, p. 671, 672). However, the pericardium constraints the motion of the heart. During the diastole, the pericardium restrains the ventricular filling. During the systole, the pericardium constraints the radial motion of the heart. Since the pericardium surrounds both ventricles, it promotes the interaction of both cavities and thus supports the synchronization of the contraction of both ventricles (Richardson et al., 2009, ch. 8, p.128),(Nielsen et al., 1983).

Some patients have a rare cardiac defect known as congenital absence of pericardium. Their heart often shows an abnormal motion (*pendulum movement*) during the contraction with an abnormal deformation (*teardrop shaped heart*) and an unphysiological variation of the total heart volume (Topilsky et al., 2010; Mantovani et al., 2011; Psychidis-Papakyrtsis et al., 2007).

2.2 The Cardiac Cycle

In the following, the heart cycle of the left ventricle is described. The description for the right ventricle can be obtained by replacing left with right, aorta with pulmonary artery, mitral with tricuspid and pulmonary

veins with venae cavae. At end diastole, the left ventricle is completely filled with blood while the aortic valve is closed, since the pressure in the aorta is higher than the pressure in ventricle. At beginning of the systole, the left ventricle contracts isovolumetrically, whereby the cavity pressure increases rapidly. When the pressure in the ventricle succeeds the pressure in the aorta, the valve opens and the blood is ejected into the aorta. The pressure in the left ventricle further increases until it reaches its maximum. Shortly afterwards, the valve closes again. At that point, the cavity volume has almost reached its minimum. During the contraction of the ventricle, the atrium is filled with blood from the pulmonary veins. Eventually, the left ventricle begins to relax, but since the pressure in the left ventricle is still higher than the atrial pressure, the mitral valve is still closed. Accordingly, no blood can leave or enter the ventricle and the left ventricle relaxes isovolumetrically, while the cavity pressure drops rapidly until it undermines the atrial pressure. At that point, the mitral valve opens again and the ventricle gets filled with blood from the left atrium. The atrium itself also contributes actively to the ventricular filling and therefore contracts at late diastole shortly after the next heart beat has been triggered. (Martini et al., 2011, ch. 20, p. 690-694) A diagram of the left cavity volume and pressure during the contraction is presented in Fig. 2.3. The blood from the right ventricle which is deoxygenated is pumped into the pulmonary circulation where carbon dioxide is exchanged for oxygen. From there, the blood arrives through the left atrium in the left ventricle (Martini et al., 2011, ch. 21, p. 737), where it gets pumped into the peripheral circulation. Here, it sustains the organs with oxygen and nutrients and collects the carbon dioxide. From the peripheral circulation, it finally arrives through the right atrium in the right ventricle. (Martini et al., 2011, ch. 21, p. p.738)

2.3 Electrical Excitation of Cardiomyocytes and Excitation Propagation

The cell membrane encloses the inside of the cell and thereby, it separates the intracellular space from the extracellular space. It contains different

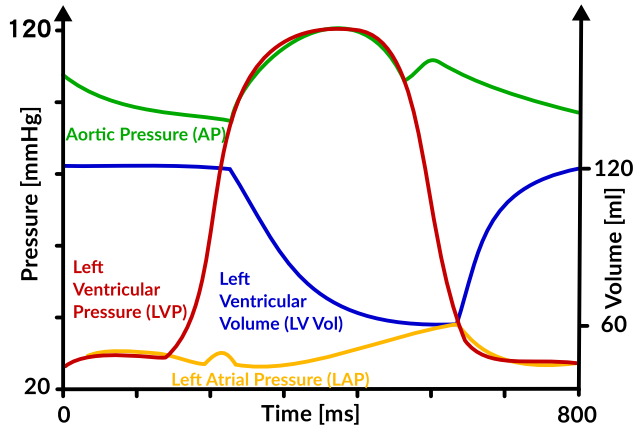


Figure 2.3: Schematic diagram of the left ventricular volume, left ventricular pressure, left atrial pressure and aortic pressure over time (based on (Loushin et al., 2009, sec 18.2, p. 272, fig. 18.1))

selective transport proteins through which ions can pass the cell membrane (Seemann, 2005, sec 2.1.1, p. 7,8) (Fig. 2.4).

Differences in the ion concentration in the extra- and intracellular space result in an electrochemical potential difference across the membrane. In resting state, the transmembrane voltage (also known as *resting potential*, even though it is actually a potential difference) is about -90 mV. (Martini et al., 2011, ch. 20, p. 689).

A myocyte has the ability to become *electrically excited* (electrical activation or depolarization). If the cell depolarizes, the transmembrane voltage increases rapidly and returns to the resting voltage, shortly afterwards. The characteristic voltage time course is the *action potential* (Martini et al., 2011, ch. 20, p. 689). Its formation is a complex interplay of different active and passive ion transport proteins, where the most relevant involved ions are sodium, potassium and calcium. Simplified and briefly summarized, the following happens: The sodium channels are voltage-gated and open if a voltage threshold of about -75 mV across the cell membrane is exceeded (Martini et al., 2011, ch. 20, p. 689). This can be caused by activated adjoining cells or intrinsically, due to a drift of the mem-

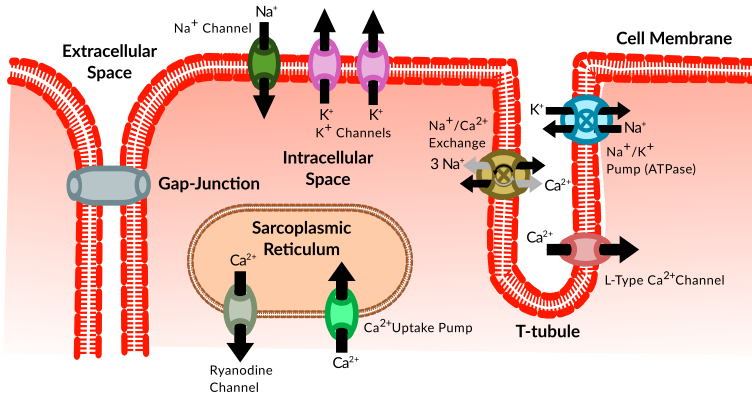


Figure 2.4: Schematic description of the cell membrane of a myocyte (inspired by (Knollmann and Roden, 2008, fig. 2))

brane voltage which is the case in pacemaker cell (Martini et al., 2011, ch. 20, p. 685). Sodium flows into the cell rapidly and the cell membrane depolarizes. Shortly after, the sodium channels close again and the cell starts to pump sodium out of the cell (Na^+/Ca^{2+} -exchanger). At the same time, calcium channels open and due to the calcium influx, the membrane voltage maintains a more or less constant level for a certain time known as the *plateau phase*. Eventually, potassium channels open and the calcium channels close and the cell starts to repolarize. Afterwards, the cell remains unexcitable for a short period (refractory period) (Martini et al., 2011, ch. 20, p.689,690).

In resting state Na^+/K^+ -pumps are responsible for maintaining the resting potential (Seemann, 2005, sec 4.3.2, p. 36,37). The Na^+/Ca^{2+} -exchanger have two modes: A forward mode which is active during the resting state and a reverse mode which is active during the depolarization (Seemann, 2005, sec. 4.3.3, p. 37).

The cardiac cells are electrically coupled with each other internally by gap junctions (Laske et al., 2009, ch. 11, p.167) and externally by the extracellular space (Seemann, 2005, sec. 4.5, p. 41). This allows the

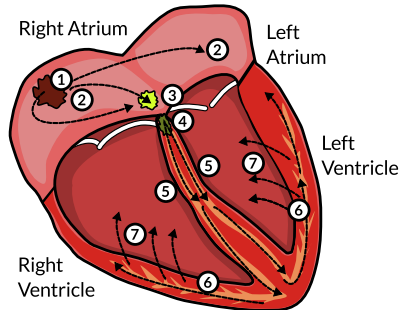


Figure 2.5: (1) Sinus node (2) Activation of the atrial myocardium (3) AV node (4) Bundle of His (5) Bundle branches (6) Purkinje network (7) Activation of the ventricular myocardium (inspired by (Laske et al., 2009, ch. 11, p.164 fig. 11.7 and p. 168, fig. 11.14))

propagation of the electrical activation from cell to cells.

In the normal case, the electrical activation of the heart is triggered in the sinus node which is located in the right atrium (Fig. 2.5). From here, the activation spreads into both atria and initiates their contraction. The next station is the atrioventricular node (AV node), which is the sole electrical link between atria and ventricles. After a delay of about 100 ms the activation arrives at the AV node (Martini et al., 2011, ch. 20, p. 686). From there, the activation propagates through the bundle of His (also called AV bundle), the bundle branches and the Purkinje fiber network. Eventually, the activation arrives in the ventricular myocardium where it initiates the ventricular contraction. At that time, the atrial contraction has already finished and the ventricle is filled with blood (Martini et al., 2011, ch. 20, p. 685, 686),(Laske et al., 2009, sec. 11.2, p. 160-164).

Active tension development

A cardiac muscle fiber is composed of multiple myofibrils, while those consist of repeating sarcomeres. The sarcomere is the contractile unit of the myocardium (Martini et al., 2011, ch. 10, p. 288). The sarcomere itself consists of overlapping actin filaments and myosin filaments (also known as thin filaments and thick filaments) (Fig. 2.6, left side). The myosin

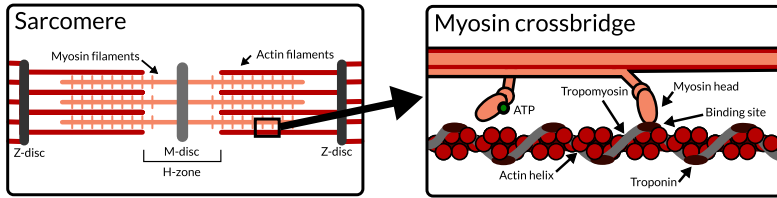


Figure 2.6: Left: The sarcomere consisting of actin and myosin filaments, Right: ATP binds to the myosin head and causes a movement of the myosin head (inspired by (Schmidt and Lang, 2007, sec. 6.1, p. 113, fig. 6.1 and p. 116, fig. 6.3))

filament has several myosin heads which have the ability to bind to special binding sites on the actin filament (Martini et al., 2011, ch. 10, p. 290). However, in resting state this is inhibited by a further protein complex, the tropomyosin, which covers that binding site (Seemann, 2005, ch. 6, p. 83). Each tropomyosin protein has a troponin protein complex at its end, which acts like a switch. When the cell is depolarized, calcium ions enter the cell and trigger a further release of calcium from the sarcoplasmic reticulum. This causes a rapid increase of the intracellular calcium concentration (Seemann, 2005, sec. 4.6, p. 41). If a calcium ion binds to the troponin complex, it causes the tropomyosin protein to change its configuration and thereby, to release the binding site. This opens the chance for a myosin head to bind to the actin filaments. Now the cross bridge cycle can start: ATP binds to the myosin head, dissociates the binding to the actin filament and causes a movement of the myosin head to the next binding site by inducing a change of the protein configuration. Afterwards, ATP is hydrolyzed and the myosin head binds to the binding site and executes a power stroke which results in a relative movement of the actin and myosin filaments (Martini et al., 2011, ch. 10, p. 296-298) (Fig. 2.6, right side). This process repeats as long as enough calcium and ATP is available until either the myosin filament reaches the Z-disc or the actin filament reaches the M-disc (Seemann, 2005, sec. 6.1, p. 84).

Chapter 3

Modeling of Cardiac Electrophysiology and Tension Development

3.1 Introduction

This chapter gives a brief overview of the modeling of cardiac electrophysiology, tension development and excitation propagation. These models provide the input for the biomechanical simulation framework. The cell model describes the de- and repolarization of the cardiomyocytes. The bidomain model allows to simulate the excitation propagation due to the electrical coupling of the cells. The active tension development model describes the tension which is generated by the cardiomyocyte.

3.2 Modeling Electrophysiology of Cardiac Cells

In 1952, Hodgkin and Huxley presented the first electrophysiological cell model. It describes the electrophysiology of a squid axon (Hodgkin and Huxley, 1952). The cell membrane is described as a capacitor in parallel with three different ion current channels for the sodium current and the potassium current and a leakage current which subsumes all the other ion

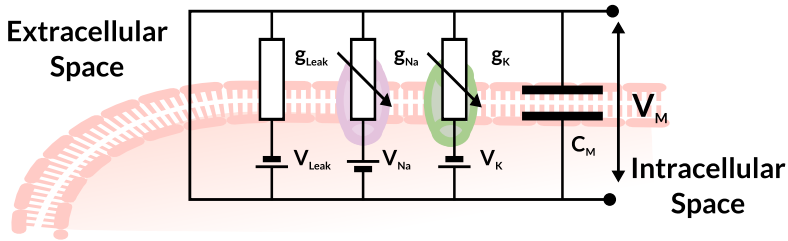


Figure 3.1: The Hodgkin-Huxley model describes the cell membrane as a capacitor in parallel with three different current channels for the sodium current and the potassium current and a leakage current which subsumes all the other ion currents

currents (Fig. 3.1). This results in the equation (Keener and Sneyd, 2009b, sec. 5.1, p. 196,197)

$$C_m \frac{dV_m}{dt} + g_{Na}(V_m - V_{Na}) + g_K(V - V_K) + g_{Leak}(V - V_{Leak}) - I_{ex} \quad (3.1)$$

where g_{Na} , g_K and g_{Leak} are the conductances for the referring currents and V_{Na} , V_K and V_{Leak} are the ion-specific equilibrium potential differences resulting from the concentration gradients across the membrane (Nernst potential) (Keener and Sneyd, 2009b, sec. 2.6, p. 80-82).

An ion current channel can either be open or closed, while there may be different protein configurations for the closed state. Rate constants, which are mostly voltage-dependent, describe the transition between the channel states (Seemann, 2005, sec. 5.1, p. 56). The conductance for a membrane current depends on the fraction of open current channels for that specific current. This is represented by gating variables which are described by first order ordinary differential equations in terms of the rate constants. (Seemann, 2005, sec. 5.4, p. 62-64).

Based on the Hodgkin-Huxley model, different electrophysiological models for cardiac myocytes have been developed. For this work, the following two are relevant:

Ventricular cell electrophysiology: The ten Tusscher *et al.* model

The cell model presented by ten Tusscher *et al.* (2004) is adapted to experimental measurement data of the major ion channels of the human ventricles for epicardial, mid-myocardial and endocardial cells. Moreover, it includes a comprehensive description of the intracellular calcium dynamics based on a Markov model for the calcium-induced calcium release. Apart from that, it considers the fast and slow voltage-gated inactivation of the L-type calcium current.

This makes it attractive for electromechanical simulations, since here the calcium concentration is usually the input for the active tension development model.

Atrial cell electrophysiology: The Courtemanche *et al.* model

Courtemanche *et al.* (1998) published a cell model which describes the electrophysiology of the human atria. Krueger *et al.* (2011) presented an extended heterogeneous version of the model which was adjusted to reproduce the action potential of 13 different regions of the atria.

3.3 Modeling of the Active Tension Development: The Hybrid model by Sachse, Glaenzel and Seemann

The hybrid tension development model (HTD-model) was presented by Sachse *et al.* (2009). The name results from the fact that the model combines parts from different active tension development models. The calcium binding to troponin was taken from (Rice *et al.*, 1999), while the interaction of actin and myosin is based on the work of (Bers, 1991), (Gordon and Regnier, 2001) and (Spudich, 2001). For the transformation changes of tropomyosin, a new approach was presented (Seemann, 2005, sec. 9.1.2, p. 117).

In a nutshell, the model is based on the sliding filament theory and uses three Markov chains to model the physiological processes. The first

Markov chain has two states and describes the binding of calcium to troponin C. The second Markov chain has also two states and describes the configuration changes of the tropomyosin proteins. The third Markov chain has ten states and describes the cross bridge cycle. Input is the calcium concentration, which can be obtained from the electrophysiological cell model. Output is a normalized active tension. (Seemann, 2005, sec 10.6, p.147-160).

3.4 Modeling of Cardiac Excitation Propagation: Bidomain Model and Monodomain Simplification

The bidomain model was presented the first time by Tung (1978). It is a macroscopic model which handles the complex cell microstructure as a homogeneous medium consisting of two coupled domains which represent intra- and extracellular space which occupy the same geometrical Space (Keener and Sneyd, 2009a, sec. 12.3.3, p. 566-568). At each point of that space, a current per volume i_m can flow from one domain into the other. The current per volume density i_m is the source for the current (per surface) density $\mathbf{j}_{(i/e)}$ inside the domains:

$$\nabla \cdot \mathbf{j}_i = \nabla \cdot (\sigma_i \nabla \phi_i) = i_m \quad (3.2)$$

$$\nabla \cdot \mathbf{j}_e = \nabla \cdot (\sigma_e \nabla \phi_e) = -i_m \quad (3.3)$$

$$\Rightarrow \nabla \cdot (\sigma_i \nabla \phi_i) + \nabla \cdot (\sigma_e \nabla \phi_e) = 0 \quad (3.4)$$

All current that leaves one domain enters the other, accordingly the sign of i_m in the second equation has an opposite sign. The subscripts i and e refer to the intra- and extracellular space. The tensors σ_i and σ_e represent the conductivity of extra- and intracellular space, which is usually anisotropic. With the definition of the transmembrane voltage $V_m = \phi_i - \phi_e$ in combination with Eq. 3.2 and Eq. 3.4, we can derive the following two coupled equations (Seemann, 2005, sec. 5.6.3.1, p. 78-80):

$$\nabla \cdot (\sigma_i \nabla V_m) + \nabla \cdot (\sigma_i \nabla \phi_e) = i_m \quad (3.5)$$

$$\nabla \cdot ((\sigma_i + \sigma_e) \nabla \phi_e) = -\nabla \cdot (\sigma_i \nabla V_m) \quad (3.6)$$

An electrophysiological cell model, for example the one of ten Tusscher, can be used to determine i_m . However, the bidomain model is a continuous approach and does not consider the cells as geometrical objects. A factor β which depends on the cells surface to volume ratio has to be introduced in order to convert the ionic and capacitive currents which cross the cell membrane into a current per volume density (Keener and Sneyd, 2009a, sec. 12.3.3, p. 567).

$$i_m = \beta \left(C_m \frac{dV_m}{dt} + I_{\text{ion}} \right) + i_{\text{ex}}. \quad (3.7)$$

The term i_{ex} is added in order to be able to consider an externally induced current. With the simplifying assumption, that extra- and intracellular space have equal anisotropy ratios ($\rightarrow \sigma_i = \alpha \cdot \sigma_e$) the bidomain equations can be merged into one equation (Seemann, 2005, sec. 5.6.3.2, p. 81):

$$i_m = \frac{1}{1 + \alpha} (\nabla \cdot (\sigma_i \nabla V_m)) \quad (3.8)$$

This is called the monodomain model. The equation of the monodomain and bidomain model can be solved numerically using the finite differences method or the finite element method.

Fiber Orientation and Stimulation Profile

The conductivity of cardiac tissue is anisotropic and depends on the fiber orientation. A common rule-based approach to model the fiber orientation in the ventricles is to define the fiber depending on the location in the ventricular wall according to measurements data e.g. of (Streeter, 1979). For the atria, Krueger et al. (2011) presented a semi-automatic approach: First, a set of seed-points has to be assigned manually. These are used by the algorithm to construct a "network of auxiliary lines" which is then used to generate the fiber orientation. The electrical activation is initiated in the atria. From here, it propagates through the Purkinje network into the myocardium. Keller et al. (2009) presented a method to generate a realistic stimulation profile which mimics the electrical activation in the myocardium by the Purkinje fiber system.

3.5 The Electrophysiological Simulation Framework *acCELLerate*

The software framework *acCELLerate* is a modular-designed simulation environment which has been developed and continuously extended over the last decade at the Institute of Biomedical Engineering. It contains implementations for all the models which have been discussed in the chapter and allows to simulate the electrical activation on cellular level, the active tension development of the myofibrils and the excitation propagation for the atria and the ventricles. It includes several cell models which have been adapted to measurement data of experiments with ventricular and atrial cells of different mammals e.g. human, rabbit, canine and considers different transmural and apico-basal heterogeneities (Seemann et al., 2010).

Chapter 4

Modeling of the Circulatory System

The Three-Element Windkessel model

A windkessel model is a lumped element model which describes the flow and pressure in the aorta with an analogous electrical circuit. The electric current represents the blood flow and the voltage represents the pressure in the aorta, thereby. The two-element windkessel model contains a capacitor C , which describes the compliance of the aorta and the large arteries in parallel with a resistor R_1 which represents the peripheral resistance. The three-element model adds a further resistor R_2 in series which describes the flow characteristic resistance of the aorta (Westerhof et al., 1971) (Fig. 4.1). The equation of the three-element windkessel model is given by:

$$\left(2 + \frac{R_2}{R_1}\right) I(t) + CR_2 \frac{dI(t)}{dt} - C \frac{dP_{ar}(t)}{dt} - \frac{P_{ar}(t)}{R_1} = 0 \quad (4.1)$$

where I is the blood flow from the heart cavity and P_{ar} is the aortic pressure.

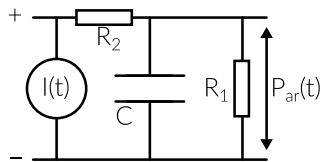


Figure 4.1: Three-element Windkessel model of the circulatory system: I represents the blood flow, C describes the compliance of the aorta and the large elastic arteries, R_1 describes the peripheral resistance. R_2 in combination with C describes the characteristic complex impedance of the aorta

Chapter 5

Nonlinear Continuum Mechanics

5.1 Basic Principles of Nonlinear Continuum Mechanics

Solid matter is not continuous but consists of particles (everyday matter consists of protons, neutrons and electrons) arranged in a specific structure. All mechanical properties of a solid object arise from the arrangement and interaction of these particles. While it is possible to describe the mechanical behaviour of microscopic objects on that level, this is certainly not feasible for macroscopic objects facing the sheer number of particles it consists of. Here, continuum mechanics theory provides a macroscopic description of the mechanical properties and kinematics of solid objects, based on constitutive equations which are usually either of phenomenological nature or are derived from the microscopic picture. In the following, I will give a short and step-by-step summary of all the basic principles of continuum mechanics theory which are relevant for this work. For a detailed description, I recommend the book "Nonlinear Finite Elements for Continua and Structures" by Belytschko et al. (2000). Since we talk about mechanics, it is no surprise, that we start with the Newton's second law of motion which is given by:

$$\mathbf{F}(t) = m \cdot \mathbf{a}(t) \quad (5.1)$$

where the total force \mathbf{F} is the vector sum of all forces acting on an object with mass m which causes an acceleration \mathbf{a} of that object. A solid body at time t can be described as a continuum of points $\mathbf{x}(t)$ where each point has a mass density ρ . For any arbitrary subdomain of that body Eq. 5.1 can be written as,

$$\int_{\Omega} \rho(x) \cdot \mathbf{a}(\mathbf{x}, t) d\Omega = \mathbf{F}(t) \quad (5.2)$$

where \mathbf{F} is the total force acting on the points within the subdomain Ω and is given by (Belytschko et al., 2000, sec. 3.5.5, p. 113)

$$\mathbf{F} = \int_{\Gamma} \mathbf{t} d\Gamma + \int_{\Omega} \rho \mathbf{b} d\Omega \quad (5.3)$$

where Γ is the boundary of Ω , \mathbf{t} is the surface traction (force per surface) and \mathbf{b} is a body force per unit mass.

Lagrangian coordinates, Eulerian coordinates and measures of deformation

The current deformation of an object can be determined by comparing the initial state of that object, in the following referred to as the *reference configuration*, with the current state or *current configuration*. For this purpose, two coordinate system are introduced: the *Lagrangian coordinate system* and the *Eulerian coordinate system* (Belytschko et al., 2000, sec. 3.2.2, p. 77). Each point of an object is identified by its Lagrangian coordinates \mathbf{X} which are the coordinates of its position vector in the reference configuration. The Eulerian coordinates describe the position $\mathbf{x}(X, t)$ of a point \mathbf{X} at time t . $\mathbf{u}(t, X) = \mathbf{x}(X, t) - \mathbf{X}$ is the displacement of point \mathbf{X} at time t .

Accordingly, the Lagrangian coordinates of a point are invariant under deformation, while the Eulerian coordinates describe its trajectory. The Jacobian matrix \mathbf{F} of the Eulerian coordinates with respect to the Lagrangian coordinates is called the *deformation tensor* (Fig. 5.1) and is given by

$$F_{ij} = \frac{\partial x_i}{\partial X_j} \quad (5.4)$$

The deformation tensor is the transformation matrix from the reference coordinates to current coordinates. However, this also means, that it does not just contain the information about the *pure* stretch but also about the rotation. Later we will see, that the constitutive equation is a potential elastic energy density function expressed in terms of a strain measure. Since the potential elastic energy of an object should not depend on its orientation, it is preferable to have a strain measure which is rotation-independent. According to the polar decomposition theorem, \mathbf{F} can be decomposed to (Bonet, 1997, sec. 3.6, p. 68-73):

$$\mathbf{F} = \mathbf{R}\mathbf{U} \quad (5.5)$$

where \mathbf{R} is a unitary rotation tensor and \mathbf{U} contains only information about the stretch. From this follows

$$\mathbf{C} = \mathbf{F}^T \mathbf{F} = \mathbf{U}^T \mathbf{R}^T \mathbf{R} \mathbf{U} = \mathbf{U}^T \mathbf{U} \quad (5.6)$$

where the tensor \mathbf{C} is the Right Cauchy-Green tensor. This strain is rotational invariant. A further commonly used strain measure is the Green-strain tensor (Bonet, 1997, sec. 3.5, p. 65), given by

$$\mathbf{E} = \frac{1}{2}(\mathbf{C} - \mathbf{I}) \quad (5.7)$$

which has the advantage, that it is zero for non-deformation.

Stress measures

The deformation of an elastic object causes mechanical stress which counteracts the deformation. The Cauchy stress $\boldsymbol{\sigma}$ (Fig. 5.2) is defined by the Cauchy's law which states (Belytschko et al., 2000, sec. 3.4, p. 101)

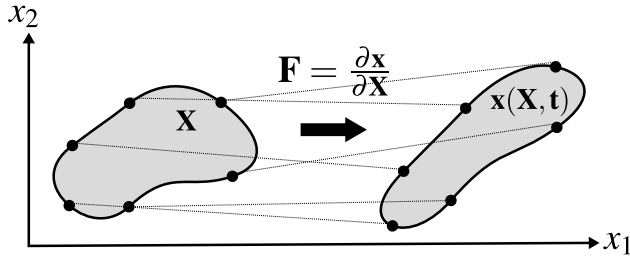


Figure 5.1: The deformation tensor

$$\mathbf{t} d\Gamma = \mathbf{n}\boldsymbol{\sigma} d\Gamma \quad (5.8)$$

Cauchy stress corresponds to the *real* or *physical* stress, since it refers to the current configuration. However, different stress measures can be defined which differ by their frame of reference (see (Belytschko et al., 2000, sec. 3.4, p. 101-104). In this work, the following two stress measures will be considered. The nominal stress tensor \mathbf{P} and the second Piola-Kirchhoff stress tensor (PK2) \mathbf{S} . \mathbf{P} is defined as

$$\mathbf{P} = J\mathbf{F}^{-1}\boldsymbol{\sigma} \quad (5.9)$$

where $J = \det(\mathbf{F})$. Accordingly the stress tensor \mathbf{P} can be used to express the current force $d\mathbf{f}$ acting on a surface Γ in terms of the normal vector \mathbf{n}_0 and that surface in the reference configuration Γ_0

$$d\mathbf{f} = \mathbf{n}_0\mathbf{P}d\Gamma_0 \quad (5.10)$$

The second Piola-Kirchhoff stress tensor \mathbf{S} is defined as

$$\mathbf{S} = J\mathbf{F}^{-1}\boldsymbol{\sigma}\mathbf{F}^{-T} \quad (5.11)$$

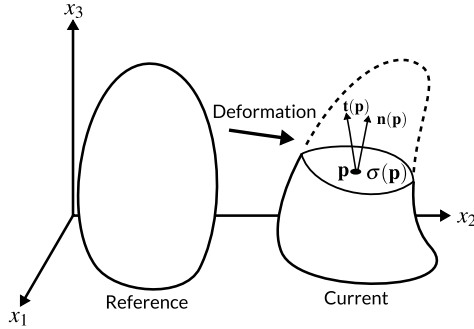


Figure 5.2: The Cauchy stress tensor (inspired by (Bonet, 1997, sec 4.2.1, p. 101, fig. 4.4))

Constitutive Models

A material for which the work does not depend on the load path is defined to be hyperelastic (Belytschko et al., 2000, sec. 5.4.7, p. 235). In that case, a potential Ψ_E in terms of \mathbf{E} or if preferred likewise in terms of \mathbf{C} , where $\Psi_E(\mathbf{E}) = \Psi_C(2\mathbf{E} + \mathbf{I})$, can be defined for the stress

$$\mathbf{S} = \frac{\partial \Psi_E}{\partial \mathbf{E}} = 2 \frac{\partial \Psi_C}{\partial \mathbf{C}} \quad (5.12)$$

This potential represents the stored energy per undeformed volume and hence is also called *energy density function*. Since Ψ defines the mechanical properties, it is also called *constitutive model* or *constitutive material law*.

Incompressibility

Many materials in particular biomaterials are incompressible. A common approach to incorporate incompressibility into the material law is to use a penalty term in form of a volumetric energy density $U(J)$ which is added to the distortional component $\hat{\Psi}(\mathbf{C})$ (Bonet, 1997, sec. 5.5.3, p. 131,132)

$$\Psi(\mathbf{C}) = \hat{\Psi}(\mathbf{C}) + U(J) \quad (5.13)$$

where J is the determinate of the deformation tensor \mathbf{F} . A simple approach for $U(J)$ is

$$U(J) = \frac{1}{2} \kappa (J - 1)^2 \quad (5.14)$$

where κ is the penalty parameter.

In that case, the second Piola-Kirchhoff tensor is given by

$$\mathbf{S} = 2 \frac{\partial \hat{\Psi}_C}{\partial \mathbf{C}} + p J \mathbf{C}^{-1} \quad (5.15)$$

$$\text{where } p = \frac{dU}{dJ} = \kappa (J - 1) \quad (5.16)$$

The value of p is the hydrostatic pressure and κ can be identified as the bulk modulus of the material.

Neo-Hookean Material and Mooney-Rivlin Material

In general, the potential Ψ of an incompressible and isotropic material can be expressed as a series expansion in terms of the first invariant I_1 and second invariant I_2 of \mathbf{C} (Belytschko et al., 2000, sec. 5.4.11, p. 239)

$$\Psi(I_1, I_2) = \sum_{i=0}^n \sum_{j=0}^n c_{ij} (I_1 - 3)^i (I_2 - 3)^j \quad (5.17)$$

$$\text{where } c_{00} = 0 \quad (5.18)$$

where c_{ij} are material constants.

The Mooney-Rivlin model is a hyperelastic model which was originally developed to describe large deformations of rubber. Mooney and Rivlin showed that the form (Belytschko et al., 2000, sec. 5.4.11, p. 239,240).

$$\hat{\Psi}(I_1, I_2) = c_1 (I_1 - 3) + c_2 (I_2 - 3) \quad (5.19)$$

matches well to experimental results. For incompressible materials the following modified Mooney Rivlin model can be used

$$\Psi = \hat{\Psi} + p_0 \ln(I_3) + \frac{1}{2} K (\ln(I_3))^2 \quad (5.20)$$

where p_0 is chosen so that the components of \mathbf{S} are zero for the reference configuration. K is a penalty parameter, which must be on the one hand large enough so that the compressibility is negligible small but on the other hand, not too large, since this would result in numerical ill-conditioning (Belytschko et al., 2000, sec. 5.4.11, p. 240).

Balance of linear momentum equation

Substituting Eq. 5.8 in Eq. 5.3 and invoking Gauss's theorem gives (Belytschko et al., 2000, sec. 3.5.5, p. 113)

$$\mathbf{F} = \int_{\Omega} \operatorname{div} \boldsymbol{\sigma} + \rho \mathbf{b} \, d\Omega \quad (5.21)$$

Substituting this in Eq. 5.2 gives

$$\int_{\Omega} \rho \mathbf{a} - \operatorname{div} \boldsymbol{\sigma} - \rho \mathbf{b} \, d\Omega = 0 \quad (5.22)$$

This holds for any arbitrary subdomain of our solid body. Accordingly, we can derive the *Balance of linear momentum equation* or just momentum equation (Belytschko et al., 2000, sec. 3.5.5, p. 114)

$$\rho \mathbf{a} - \operatorname{div} \boldsymbol{\sigma} - \rho \mathbf{b} = 0 \quad (5.23)$$

This is the fundamental equation which describes the mechanical behaviour and kinematics of a solid body. For static problems where the momentum is zero or for problems where loads are applied so slowly that the inertial forces can be neglected, Eq. 5.23 can be reduced to (Belytschko et al., 2000, sec. 3.5.6, p. 115)

$$\operatorname{div} \boldsymbol{\sigma} = -\rho \mathbf{b} \quad (5.24)$$

Chapter 6

Finite Element Analysis

Finite Element Analysis for Nonlinear Continuum Mechanics

6.1 Finite Element Method for Nonlinear Continuum Mechanics

In this chapter we transform Eq. 5.23 into a discrete form using the finite element analysis. The content of this chapter and the indices notation are in parts based on (Belytschko et al., 2000, sec. 4.7,4.8 and 4.9, p. 193-201). Einstein's summation notation is used for all equations.

Total Lagrangian Weak Form of the Linear Moment Equation

We start with the linear moment equation Eq. 5.23 with indices notation in terms of the displacement \mathbf{u}

$$\rho \ddot{u}_i - \frac{\partial}{\partial x_j} \sigma_{ji} - \rho b_i = 0 \quad (6.1)$$

where $\ddot{u} = a$. Our aim is to find a solution displacement u_i . However, this equation has often, depending on the kind of problem, no analytical

solution, or it is tough to find one. The basic idea of the finite element method is to approximate u_i in the domain of interest Ω with a trial function \tilde{u}_i consisting of a defined finite set of suitable basis function N_I called element shape function, which vanish on the displacement boundaries.

$$u_i \approx \tilde{u}_i = u_{iI} N_I \quad (6.2)$$

The notation u_{iI} has to be read as component i ($i = 1, 2$ or 3) of node I of the discretized domain. Then we transform the examined partial differential equation in such a way, that we finally obtain a set of equations for the coefficients u_{iI} .

Since \tilde{u}_i is an approximation, we obtain the residual R

$$R = \rho \frac{d^2}{dt^2} \tilde{u}_i - \frac{\partial}{\partial x_j} \sigma_{ji}(\tilde{u}_i) - \rho b_i \quad (6.3)$$

The idea of the Galerkin Method of Weighted Residuals is to use an arbitrary weighting function w_i (test function) from the same function space as the trial function and build the inner product with R .

$$w_i = w_{iI} N_I \quad (6.4)$$

The optimal solution \tilde{u}_i is then the one for which this inner product equals zero, since then the residual is orthogonal to the function space of the trial function. For mechanical problems, the test function w_i can also be interpreted as a virtual displacement or first variation of the displacement ($w_i = \delta u_i$) and the inner product as a virtual energy ((Belytschko et al., 2000, sec. 2.3.4, p. 32 and sec. 4.8.1, p. 197)).

$$\int_{\Omega} w_{iI} \left(\rho N_I N_J \ddot{u}_{jJ} - \frac{\partial N_I}{\partial x_j} \sigma_{ji} - \rho N_I b_i \right) d\Omega = 0 \quad (6.5)$$

This equation is the weak form of the linear momentum equation. With the following relations (Belytschko et al., 2000, sec. 4.7.2, p. 195)

$$J\sigma_{ji} = F_{jk}P_{ki} = \frac{\partial x_j}{\partial X_k} P_{ki} \quad (6.6)$$

$$d\Omega = Jd\Omega_0 \quad (6.7)$$

$$\rho b_i = \rho_0 b_i \Omega_0 \quad (6.8)$$

we can transform it into the total Lagrangian form

$$\int_{\Omega_0} w_{il} \left(\rho_0 N_I N_J \ddot{u}_{jJ} - \frac{\partial N_I}{\partial X_j} P_{ji} - \rho_0 N_I b_i \right) d\Omega_0 = 0 \quad (6.9)$$

Now we use the derivative product formula in order to get rid of the derivative of the nominal stress and apply the Gauss's theorem on the result. Then we use that w_i vanishes on the traction boundary and obtain discrete equations of the weak form of the total Lagrangian formulation (see (Belytschko et al., 2000, sec. 4.8.1, p. 196-197, eq. 4.8.3 - 4.8.7 and sec. 4.9 p.198-201, eq. 4.9.9-4.9.15) for details)

$$\delta W = w_{il} \int_{\Omega_0} \rho_0 N_I N_J \ddot{u}_{jJ} d\Omega_0 + w_{il} f_{il}^{int} - w_{il} f_{il}^{ext} = 0 \quad (6.10)$$

$$\text{where } f_{il}^{int} = \int_{\Omega_0} \frac{\partial N_I}{\partial X_j} P_{ji} d\Omega_0 \quad (6.11)$$

$$\text{and } f_{il}^{ext} = \int_{\Omega_0} N_I \rho_0 b_i d\Omega_0 + \int_{\Gamma_0} N_I t_i^0 d\Gamma_0 \quad (6.12)$$

where Γ_0 is the surface on which the traction t_i^0 acts in reference configuration. δW is the virtual work due to the virtual displacement w_i . Accordingly the f_{il}^{int} and f_{il}^{ext} are the equivalent internal and external nodal forces (Belytschko et al., 2000, sec. 4.4.2, p. 154 and sec. 4.9.1, p. 199, 200).

Since this equation applies for arbitrary w_i it follows

$$M_{iJlJ} \ddot{u}_{jJ} + f_{il}^{int} - f_{il}^{ext} = 0 \quad (6.13)$$

$$\text{where } M_{iJlJ} = \delta_{ij} \int_{\Omega_0} \rho_0 N_I N_J d\Omega_0 \quad (6.14)$$

To simplify the notation, we define the displacement vector $\mathbf{d}(t)$ which holds the components of $u_{il}(t)$ and can write Eq. 6.13 in vector notation

$$\mathbf{M}\ddot{\mathbf{d}} + \mathbf{f}_I^{int}(\mathbf{d}(t), t) + \mathbf{f}_I^{ext}(\mathbf{d}(t), t) = 0 \quad (6.15)$$

This is the discretized equation which has to be solved using a time integration scheme (see below) in order to simulate the mechanical behaviour and kinematics of a solid body. The integrals can be evaluated numerically using Gauss's Quadrature (Belytschko et al., 2000, sec. 4.5.3, p. 166, 167). Here the number of quadrature points depends on the order of the shape functions. Eq. 6.15 does not consider any friction. If it is desired to take friction into account, the equation can be extended with a term for damping

$$\mathbf{M}\ddot{\mathbf{d}} + \mathbf{f}_I^{int}(\mathbf{d}(t), t) + \mathbf{f}_I^{ext}(\mathbf{d}(t), t) + \mathbf{C}\dot{\mathbf{d}} = 0 \quad (6.16)$$

One possible damping model is Rayleigh damping

$$\mathbf{C} = \alpha_1 \mathbf{M} + \alpha_2 \nabla \mathbf{f}^{int} \quad (6.17)$$

where α_1 and α_2 are the material depending damping parameters.

If mass inertia is neglected, equation Eq. 6.15 reduces to the equilibrium equation

$$\mathbf{f}_I^{int}(\mathbf{d}(t), t) + \mathbf{f}_I^{ext}(\mathbf{d}(t), t) = 0 \quad (6.18)$$

which can be solved using Newton method (Belytschko et al., 2000, sec. 6.3.4, p. 319).

Linear and Quadratic Tetrahedral Element Shape Function

Many different types of element shape functions exist for the discretization of the volume integrals. For this work, the following are relevant: the four-node tetrahedron ($T4$) and the ten-node tetrahedron ($T10$) (Fig. 6.1)(Belytschko et al., 2000, ap. 3, p. 623, 624) . The shape functions are defined in terms

of the tetrahedral element coordinates ζ_i which are defined as follows

$$\mathbf{x} = \begin{pmatrix} 1 & 1 & 1 & 1 \\ x_1 & x_2 & x_3 & x_4 \\ y_1 & y_2 & y_3 & y_4 \\ z_1 & z_2 & z_3 & z_4 \end{pmatrix} \begin{pmatrix} \zeta_1 \\ \zeta_2 \\ \zeta_3 \\ \zeta_4 \end{pmatrix} = \mathbf{M} \begin{pmatrix} \zeta_1 \\ \zeta_2 \\ \zeta_3 \\ \zeta_4 \end{pmatrix} \quad (6.19)$$

where \mathbf{x} is a point in Cartesian coordinates inside the element and $x_1, y_1, z_1 \dots x_4, y_4, z_4$ are the vertices of the tetrahedron.

T4 Shape Functions

$$N_I(x, y, z) = \zeta_I(x, y, z) \quad I = 1..4 \quad (6.20)$$

The partial derivatives $\frac{\partial}{\partial \mathbf{x}} N_I = \frac{\partial}{\partial \mathbf{x}} \zeta_I$ can be easily determined by inverting the matrix \mathbf{M} . Since the shape functions are linear, this element is also named *linear tetrahedron*.

T10 Shape Functions

$$N_I(x, y, z) = \zeta_I(2\zeta_I - 1), \quad I = 1..4 \quad (6.21)$$

$$N_5(x, y, z) = 4\zeta_1 \zeta_2, \quad N_6(x, y, z) = 4\zeta_1 \zeta_3, \quad N_7(x, y, z) = 4\zeta_1 \zeta_4, \quad (6.22)$$

$$N_8(x, y, z) = 4\zeta_2 \zeta_3, \quad N_9(x, y, z) = 4\zeta_3 \zeta_4, \quad N_{10}(x, y, z) = 4\zeta_2 \zeta_4, \quad (6.23)$$

This element is also named *quadratic tetrahedron*, due to the quadratic shape functions.

Linear and Quadratic Triangle Element Shape Function

For the discretization of the surface integrals the following elements are relevant: the three-node triangle (T3) and the six-node triangle (T6) (Fig. 6.1). The shape functions defined in terms of triangle element coordinates are given by

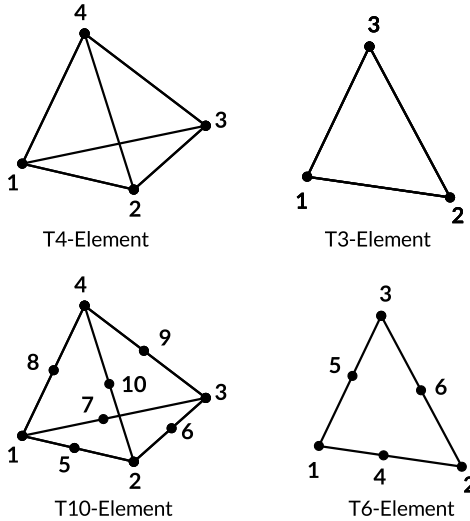


Figure 6.1: Linear tetrahedron (T4), linear triangle (T3), quadratic tetrahedron (T10) and quadratic triangle (T6)

T3 Shape Functions

$$N_I(x, y, z) = \zeta_I(x, y, z), \quad I = 1..3 \quad (6.24)$$

This element is also named *linear triangle*.

T6 Shape Functions

$$N_I(x, y, z) = \zeta_I(2\zeta_I - 1), \quad I = 1..3 \quad (6.25)$$

$$N_4(x, y, z) = 4\zeta_1\zeta_2 \quad (6.26)$$

$$N_5(x, y, z) = 4\zeta_1\zeta_3 \quad (6.27)$$

$$N_6(x, y, z) = 4\zeta_2\zeta_3 \quad (6.28)$$

This element is also referred to as *quadratic triangle*.

Newmark-Beta Time Integration

The linear momentum equation is an initial value problem, where $\mathbf{d}^0 = \mathbf{d}(t = t_0)$ and its first $\mathbf{v}^0 = \mathbf{v}(t = t_0)$ and second time derivate $\mathbf{a}^0 = \mathbf{a}(t = t_0)$ are known. A commonly used time integration method is Newmark-Beta Time integration. It provides two adjusting screws, the parameters β and γ , to control the numerical stability of the solution (Belytschko et al., 2000, sec. 6.3.3, p. 318).

The updated displacements and velocities of the Newmark-Beta scheme are given by

$$\mathbf{d}^{n+1} = \mathbf{d}^n + \Delta t \mathbf{v}^n + \frac{\Delta t^2}{2} (1 - 2\beta) \mathbf{a}^n + \beta \Delta t^2 \mathbf{a}^{n+1} \quad (6.29)$$

$$\mathbf{v}^{n+1} = \mathbf{v}^n + (1 - \gamma) \Delta t \mathbf{a}^n + \gamma \Delta t \mathbf{a}^{n+1} \quad (6.30)$$

where Δt is the chosen time step size.

From this follows

$$\mathbf{a}^{n+1} = \frac{1}{\beta \Delta t^2} (\mathbf{d}^{n+1} - \mathbf{d}^n + \Delta t \mathbf{v}^n + \frac{\Delta t^2}{2} (1 - 2\beta) \mathbf{a}^n) \quad (6.31)$$

Now, we take Eq. 6.15 and replace the second time derivate of \mathbf{d} with the updated accelerations \mathbf{a}^{n+1} and the displacement $\mathbf{d}(t)$ with the updated displacement \mathbf{d}_{n+1} . Then, we obtain a set of nonlinear algebraic equations which we can solve for \mathbf{d}^{n+1} at time step t^{n+1} (Belytschko et al., 2000, sec. 6.3.3, eq. 6.3.7), using the Newton-Raphson method ((Belytschko et al., 2000, ec. 6.3.4, p. 319)).

$$\mathbf{M} \mathbf{a}^{n+1} + \mathbf{f}_I^{int}(\mathbf{d}^{n+1}, t^{n+1}) + \mathbf{f}_I^{ext}(\mathbf{d}^{n+1}, t^{n+1}) + \mathbf{C} \mathbf{v}^{n+1} = 0 \quad (6.32)$$

Chapter 7

Constitutive Models of Cardiac Tissue

Due to its microstructure, cardiac tissue has anisotropic and incompressible hyperelastic mechanical properties (Fig. 7.1). Different constitutive models which give a description of the mechanical behaviour of cardiac tissue have been presented (Costa et al., 1996; Fung, 1993; Smaill and Hunter, 1991; McCulloch, 2000)

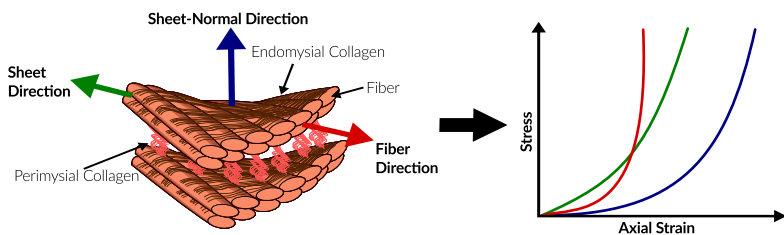


Figure 7.1: Left: cardiac microstructure with the definition of fiber, sheet and sheet-normal direction (inspired by (Hunter et al., 1997b, sec. 6.2.2, fig. 6.3, p. 176)). Right: Typical stress-strain relation for uniaxial loading (based on (Hunter et al., 1997a, sec. 12.4.2, fig 12.9)).

For most applications in this work, the model of (Guccione et al., 1991) was used.

$$W = C(e^Q - 1) + \frac{1}{2}K(\det(F) - 1)^2 \quad (7.1)$$

$$Q = b_1 E_{11}^2 + b_2 (E_{22}^2 + E_{33}^2 + E_{23}^2 + E_{32}^2) + b_3 (E_{12}^2 + E_{21}^2 + E_{13}^2 + E_{31}^2) \quad (7.2)$$

This model is orthotropic with transverse isotropy. Accordingly, it does not take into account the sheet orientation of the ventricular wall. The second term of Eq. 7.1 is a penalty term which accounts for the incompressibility. A comparison and evaluation of different constitutive models can be found in (Schmid, 2006) and in (Holzapfel and Ogden, 2009).

Chapter 8

Recent Developments in Electromechanical Modeling of the Heart

Cardiac modeling of the heart is an active field of research and a lot of progress had been made the recent years. In order to give a short overview, this chapter summarizes a selection of recent publication which are related to this thesis.

Modeling of the Ventricles

- Gurev et al. (2011) from the lab of Natalia Trayanova presented a methodology to generate an electromechanical model of the ventricular contraction using an accurate ventricular geometry based on MRI and DTMRI data. He demonstrated an example simulation of the contraction during sinus rhythm using a model of normal canine ventricles.
- Constantino et al. (2012) showed that computational modeling of the ventricular electromechanics provides a powerful tool to characterize the relationship between electrical and mechanical activation in a heart with dyssynchronous heart failure and how this can help to improve cardiac resynchronization therapy.

- The review article of Trayanova et al. (2011) gives an overview of the latest advancements in three-dimensional electromechanical modeling of the ventricles. In a second article, Trayanova (2011) present general modeling approaches and applications of whole-heart models in cardiac electrophysiology and electromechanics research.
- Krishnamurthy et al. (2012) from the group of Andrew McCulloch and Jeffrey Omens published a method which allowed to create patient-specific models of the ventricular biomechanics of the failing heart. The method was tested using data of five patients with heart failure. They obtained good results for global parameters like ejection fraction and peak value of the cavity pressures and moreover the simulation showed a good match to measured echocardiographic images.
- Hadjicharalambous et al. (2014) analyzed different constitutive laws which are often used in cardiac electromechanical modeling regarding feasibility for parameter estimation using 3D tagging MRI.
- Land et al. (2014) presented a new method to improve the numerical stability of cardiac mechanical simulations.
- Pfeiffer et al. (2014) discussed the biomechanics of cardiac electromechanical coupling and the mechanoelectric feedback.
- Eriksson et al. (2013) presented an analysis of the influence of the myocardial fiber and sheet orientations on the mechanical contraction of the left ventricle.

Modeling of the Atria

- Jernigan et al. (2007) presented a study on the mechanical properties of porcine left atrium which were assessed using uniaxial loading experiments.
- Di Martino et al. (2011a) presented a model of the porcine left atrium. He used that model to analyze the wall stress due to the mitral

valve movement, obtained from raw MDCT data. The mechanical properties were modelled based on biaxial experiments with porcine atrial tissue.

- In the same year, Di Martino et al. (2011b) evaluated how the spatial and temporal stress distribution of the left atrial wall is affected by ventricular tachypacing.
- Bellini et al. (2012) published a detailed characterization of the passive biomechanics of the left human atria based on a Fung-type constitutive model.

Personalized Modeling - Parameter Estimation Techniques

Several different approaches for the estimation of cardiac mechanical parameters have been proposed.

- Moireau and Chapelle (2011) showed how reduced-order unscented Kalman Filtering can be used for the estimation of parameters in large dynamical systems and illustrated the approach using a "test problem inspired from cardiac biomechanics".
- Wang et al. (2009) presented an approach based on sequential quadratic programming which was used to estimate the stiffness of the left ventricular myocardium.
- Delingette et al. (2012) presented a method to determine personalized cardiac motion and contractility from clinical images using variational data assimilation.
- Sermesant et al. (2012) used a personalized electromechanical model of the heart to predict pacing effects in CRT.
- Xi et al. (2011) used reduced-order Kalman filtering to estimate transversely isotropic material parameter.
- Marchesseau et al. (2013a) used the Unscented Transform algorithm to calibrate the parameters of a cardiac electromechanical model from medical image data.

- In a further work, Marchesseau et al. (2013b) used unscented Kalman filtering from regional volumes to estimate the tissue contractility from cardiac cine-MRI. First, global parameters were estimated with an automatic calibration algorithm, again based on the Unscented Transform. Then in all AHA (American Heart Association) zones of the left ventricle, the contractility was estimated using the reduced-order unscented Kalman filtering.
- Wong et al. (2014) presented an approach where they used a velocity-based objective function to identify regional maximum contraction stresses, contraction rates, and relaxation rates. Better results were found for the velocity-based approach than for a position-based approach on synthetic data. Personalized contractility parameters could be identified, which were consistent with the underlying physiologies of the patients and healthy volunteers based on clinical data.

PART II

METHODS

Chapter 9

The Biomechanical Simulation Framework

The *acCELLerate* simulation framework (Sec. 3.5) simulated the electrical activation and active tension development on cellular level as well as the excitation propagation over the heart. In context of this work, I have developed a biomechanical simulation framework, which allows to simulate the mechanical contraction of the heart due to the active tension development that is provided by the *acCELLerate* framework (Fig. 9.1). Apart from that, the biomechanical simulation framework allows to estimate the active tension from measurement data of the heart motion, which allows a personalization of the heart model. The simulation framework has been developed in C++ and makes use of the PETSc library for the matrix vector operations and to solve the arising systems of equations. The biomechanical simulation framework contains a geometrical model, generated from MRI data, which represents the whole heart and the surrounding tissue, in which the heart is embedded and the information about the fiber, sheet and sheet-normal orientation. Two solvers for the biomechanical problem have been implemented: First, the *static* solver, which determines the deformation (steady state solution) for every time step for a given active tension distribution, considering defined boundary conditions and further input variables e.g. external pressure or traction. Second, the *dynamic* solver which uses the Newmark-Beta time integration (Sec. 6.1) and further takes

into account mass inertia and damping. In addition to the displacement, it computes velocity and acceleration vector fields. Further, the framework includes an inverse solver, which I have developed in course of this work. This allows to estimate the active tension distribution from a provided motion of the heart surfaces.

For the finite element discretization, linear and quadratic triangle and tetrahedral elements have been implemented. Different constitutive models which describe the passive mechanical properties of the heart tissue are available. The resulting system of nonlinear equations is solved using the Newton method implementation of the PETSc library (Balay et al., 2012). For that purpose, the solvers provide the nodal forces and the nodal forces Jacobian matrix in terms of the displacement.

All calculations are parallelized using MPI (MPI-Forum, 1994) and the PETSc library. The solvers provide a plugin interface. This allows for their extension through further solver modules without the need to modify the corresponding source code. Among others, a module for modeling the circulatory system and a module for contact handling have been developed. The primary purpose of the contact handling module is to model the contact of the heart surface with the pericardium. In the following, the different aspects of the biomechanical simulation framework are discussed in detail.

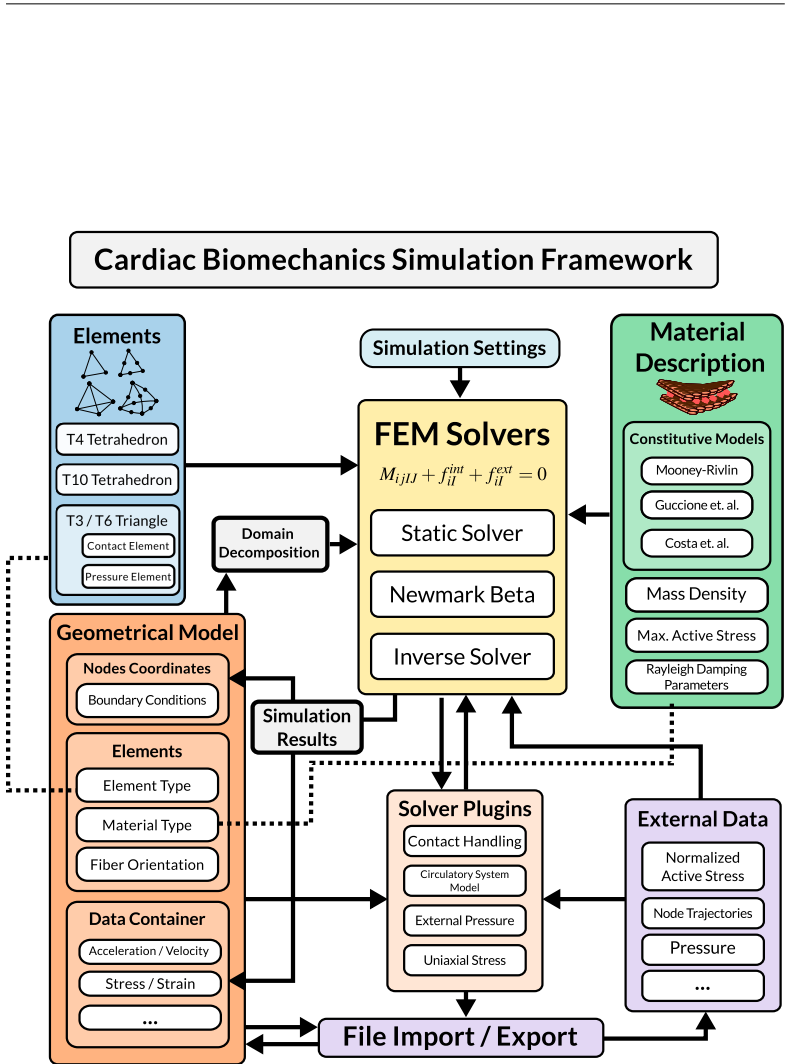


Figure 9.1: Schematic description of the biomechanical simulation framework.

Chapter 10

Geometrical Model of the Heart

The geometrical model, which was used for the different projects of this work, was generated from MRI data of a 33 years old male volunteer (Fig. 10.1 a).

The data was provided by courtesy of the University Hospital of Heidel-

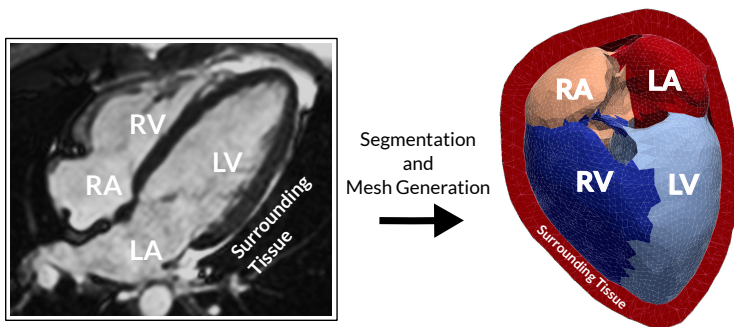


Figure 10.1: (a) MR Imaging data of a 33 years old volunteer (b) Tetrahedral mesh generated from the manually segmented imaging data

Atrial Fiber Orientation [Krueger et al.]

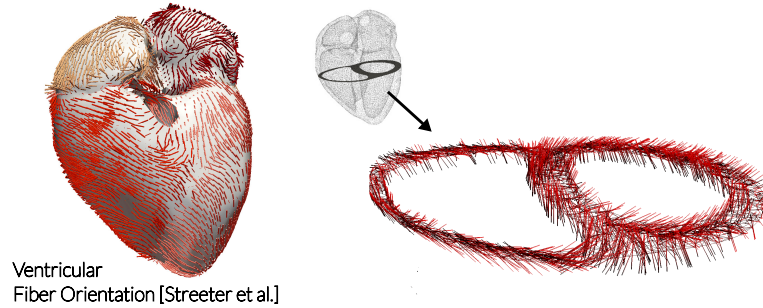


Figure 10.2: (a) Definition of the ventricular fiber orientation according to the measurements of Streeter (1979) and the atrial fiber orientation generated using the method of (Krueger et al., 2011) (b) Fiber twist through the ventricular wall

berg and segmented manually by Bettina Schwab, who worked as student assistant at the institute. Based on the segmented data, two meshes were generated: First, a structured high-resolution hexahedral mesh (0.4 mm resolution). This was generated as input for the electrophysiological and active tension simulation using *acCELLerate*. Second, a T10 tetrahedral mesh was generated for the biomechanical simulations. This consists of the whole heart, including the ventricles and the atria (11 622 elements) and a thin layer (2 696 elements) surrounding the heart, which represents the tissue in which the heart is embedded (Fig. 10.1 b). For this purpose, the heart surfaces were extracted from the segmented data set and post-processed using the 3D modeling software *Blender* (Blender, 2014). Eventually, a tetrahedral mesh was generated using the opensource mesh generator software *TetGen* (Si, 2013). The output of *TetGen* was a four-nodes tetrahedral (T4-elements) mesh. This was converted into a ten-nodes tetrahedral (T10-elements) mesh. The material classes (left ventricle, right ventricle, ...) were assigned to the elements according to the segmented data. The fiber orientation (see Sec. 3.4) of the ventricles was set using a rule-based approach based on the measurement data of Streeter (1979). For both ventricles, the rotating helix angle α_1 changes linearly from 55° (endocardium) to -75.3 (epicardium) through the ventricular wall. The

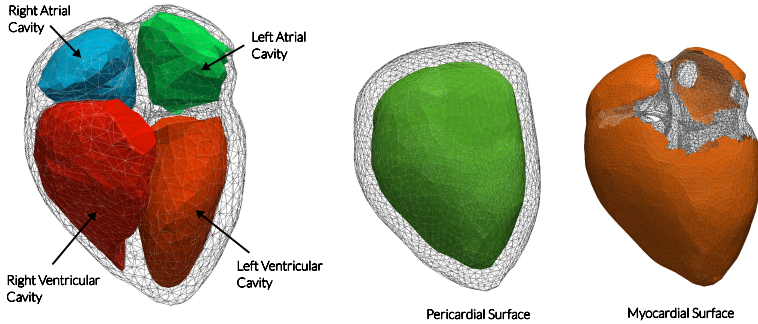


Figure 10.3: (a) Definition of the surfaces of the left and right atrial and ventricular cavities (b) Definition of the contact interface between pericardium and myocardium

transverse angle α_3 is set to a value of -3° (Keller, 2006). For the atria, the fiber assignment algorithm of (Krueger et al., 2011) was used. The fiber orientation for the ventricles and atria was assigned to the elements of the high resolution hexahedral mesh. For the ventricles, the software implementation of David Keller was used, which he had developed in context of his diploma thesis (Keller, 2006). For the atria, the software tool developed by Martin Krueger (Krueger et al., 2011) and his diploma student Viktor Schmidt (Schmidt, 2010) was used. The fiber orientation was mapped from the hexahedral mesh to the quadrature points of the elements of the coarse tetrahedral mesh (Fig. 10.2). The heart cavities are defined by closed triangle surface meshes, which share the same nodes as the tetrahedral mesh, while all openings were closed by triangularization (Fig. 10.3 a). Between the heart mesh and the mesh which represented the surrounding tissue, a contact interface is defined (Fig. 10.3 b). Boundary conditions are defined for the nodes of the mesh at the vessel openings of the atria and the nodes of the apex (Fig. 10.4).

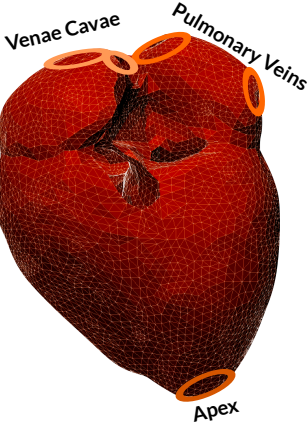


Figure 10.4: Dirichlet boundary conditions for the opening to venae cavae, the opening for pulmonary veins and the apex

Chapter 11

Modeling of the Electrical Activation and Active Tension Development

For the different projects which have been conducted in context of this work, the electrical activation on cellular level, the excitation propagation and the active tension development were simulated using the *acCELLerate* framework (Sec. 3.5). Input were the hexahedral meshes (Sec. 10) of the ventricles and of the atria in diastolic state and the fiber orientation at the nodes of each hexahedral element. No feedback of the mechanical deformation on the electrophysiology was considered. This would involve a strong coupling of the *acCELLerate* with the biomechanical simulation framework which is numerical extremely demanding for simulations of the whole heart. The simulation of the ventricles and atria were conducted independently from each other.

For the modeling of the ventricular electrophysiology on cellular level, the model of ten Tusscher et al. (2004) (see Sec. 3.2) was used. The Rush-Larsen method was used to compute the gating variables using analytical functions. All other differential equations of the ten Tusscher model were solved using forward Euler (Seemann et al., 2010). The cell models were initialized in a single cell environment. A stimulation profile which mimics the electrical activation due to the Purkinje network was created using the

software implementation of Keller et al. (2009) (see Sec. 3.4). The atrial activation was simulated using the heterogeneous Courtemanche model of Krueger et al. (2011) (Sec. 3.2). The active tension development of the ventricles was calculated using the Hybrid tension development model (HTD) of Sachse et al. (2009) (Sec. 3.3). The HTD model is originally adapted to measurement data of the ventricles. Richter (2012) adapted the HTD model to measurement data of Schotten et al. (2002) in context of his diploma thesis, which was supervised by me and Martin Krueger.

The output of the *acCELLerate* framework is normalized active tension for each node of the hexahedral mesh and for each time step (Fig. 11.1). For the biomechanical simulation, the active tension was scaled with a value for the maximal tension and interpolated to the elements of the tetrahedral mesh. The biomechanical model uses adaptive time stepping. For that reason, the active tension was interpolated linearly between the time steps of the *acCELLerate* simulation, if necessary.

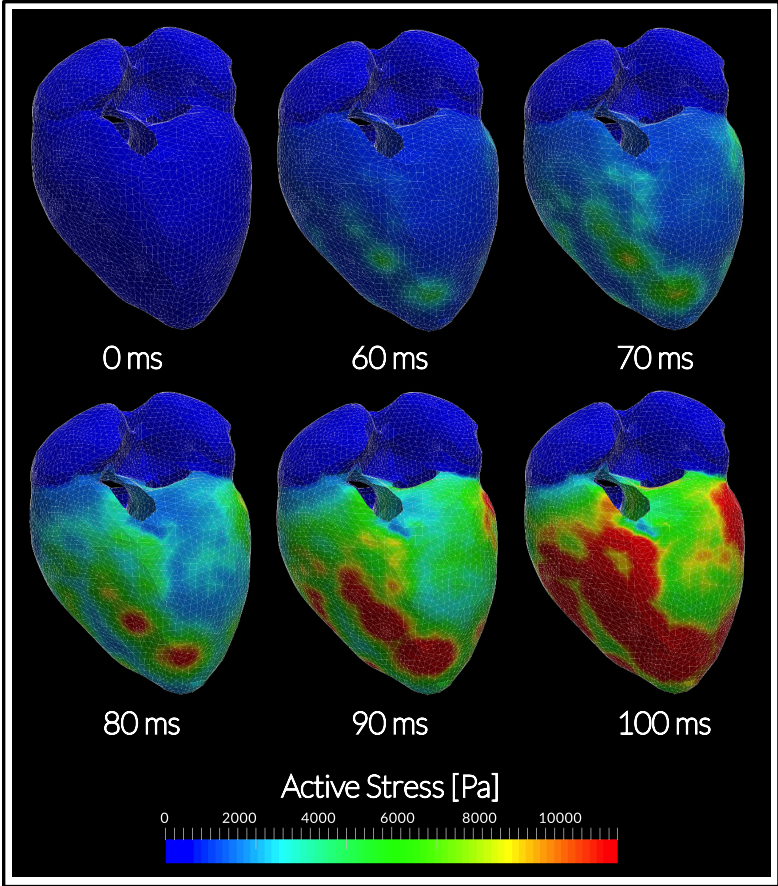


Figure 11.1: The active tension distribution in the ventricles of the first 100 ms, interpolated to the elements of the tetrahedral mesh

Chapter 12

Implementation of the Solver

12.1 Parallelization and Domain Decomposition

The simulation framework supports parallelization through distribution of the computations on multiple processes (multiprocessing). These communicate with each other using MPI (MPI-Forum, 1994). The data is organized in distributed parallel vectors and matrices utilizing the PETSc library (Balay et al., 2012). The nodes of the geometrical model are distributed to the different processes. Eventually, for each element, that process is determined, which contains most of its nodes and the element is passed to that process. For an efficient parallelization, the nodes and elements of the geometrical model should have to be distributed to the processes in such a way, that coherent subdomains of the geometrical model are stored on the processes. For that purpose, the PETSc library allows to calculate an optimal domain decomposition based on the connectivity matrix. Apart from that, the biomechanical simulation framework provides the option to sort the nodes according the first score of the Principal Component Analysis (PCA) of their position vectors.

12.2 The Biomechanical Solver

The discretized total Lagrangian weak form of the equation of linear momentum extended by a term for Rayleigh damping in vector notation is

given by

$$\mathbf{M}\ddot{\mathbf{d}} + \mathbf{C}\dot{\mathbf{d}} + \mathbf{f}_{total}(\mathbf{d}) = 0 \quad (12.1)$$

where the displacement vector \mathbf{d} consists of the entries of the displacement vector u_{iI} (see Sec. 6.1)

$$\mathbf{d} = [u_{11}, u_{21}, u_{31}, u_{12}, \dots, u_{iI}]^T \quad (12.2)$$

The index I indicates the node and i the coordinate. The mass matrix \mathbf{M} and the damping matrix \mathbf{C} as well as the nodal forces vector \mathbf{f}_{total} are filled according to the same indexing scheme. Hereby, the nodal forces vector \mathbf{f}_{total} is the sum of all internal and external nodal forces. Equation Eq. 12.1 is solved by the biomechanical solver, which can be initialized either as static solver or dynamic solver. In the first case, the mass term and the damping term in Eq. 12.1 are neglected and the steady state solution for \mathbf{d} is computed. In the second case, mass inertia and damping are taken into account and velocity and acceleration vector fields are calculated, additionally to the displacement.

Calculation of the Nodal Forces due to the Deformation of the Elements and the Active Tension

The biomechanical simulation framework contains implementations for linear (T4) and quadratic (T10) tetrahedral elements (Sec. 6.1). The derivatives of the shape functions

$$\frac{\partial N_I}{\partial X_j} \quad (12.3)$$

are calculated at the beginning of the simulation for the reference configuration.

For each element, the fiber, sheet and sheet normal orientation are defined at the quadrature points \mathbf{q}_J . For all elements, the deformation tensors are calculated for each quadrature point and transformed into a local orthonormal coordinate system (*fiber coordinate system*) which is defined by the fiber ($\mathbf{b}_f(\mathbf{q}_J)$), sheet ($\mathbf{b}_s(\mathbf{q}_J)$) and sheet normal direction ($\mathbf{b}_{sn}(\mathbf{q}_J)$).

$$\mathbf{B}_J = (\mathbf{b}_f, \mathbf{b}_s, \mathbf{b}_{sn}) \quad (12.4)$$

The deformation tensor transformed in the fiber coordinate system is given by

$$F_{ij}(\mathbf{q}_J) = \frac{\partial N_I(\mathbf{q}_J)}{\partial X_j} x_{iI} \quad (12.5)$$

$$\mathbf{F}_J^* = \mathbf{B}_J^T \cdot \mathbf{F}(\mathbf{q}_J) \cdot \mathbf{B}_J \quad (12.6)$$

The transformed deformation tensors are used to calculate the Second Piola-Kirchhoff stress \mathbf{S} using the chosen constitutive model for the defined material class of the respective element.

For that purpose, the Mooney-Rivlin model (Sec. 5.1, Eq. 5.20) and the Guccione *et al.* model (Sec. 7, Eq. 7.1) have been implemented. The active tension which was obtained from the electrophysiological simulation (using *acCELLerate*) for the respective time step (or interpolated for the respective time step if necessary), is added to the first diagonal element of the Second Piola-Kirchhoff stress. Eventually, the nominal stress is calculated

$$\mathbf{P} = \left(\mathbf{S} + \begin{pmatrix} T_k & 0 & 0 \\ 0 & 0 & 0 \\ 0 & 0 & 0 \end{pmatrix} \right) \cdot \mathbf{F}^T \quad (12.7)$$

Afterwards, the nominal stress is transformed back into the global coordinate system. The nodal forces contribution of the element K to the total nodal forces vector \mathbf{f}_{total} is given by (compare Sec. 6.1)

$$f_{iI}^K = \int_{\Omega_K^0} \frac{\partial N_I}{\partial X_j} P_{ji} d\Omega_K^0 \quad (12.8)$$

where Ω_K^0 is the volume domain of the element. The integral is computed using Gauss quadrature (at one quadrature point for the T4-elements, and four quadrature points for the T10-elements). Eventually, the nodal forces components which result from the deformation and the active tension of

element K are added to the corresponding components of total nodal forces vector \mathbf{f}_{total}

For the calculation of the nodal forces which result from surface traction (usually pressure which acts on a surface), T3 and T6 triangle elements have been implemented (Sec. 6.1). For those, the nodal forces contribution of element K to the nodal forces vector is given by (Sec. 6.1)

$$K f_{il} = \int_{\Gamma_K^0} N_l t_i^0 d\Gamma_K^0 \quad (12.9)$$

where Γ_K^0 is the surface domain of the element.

The Static Solver

The static solver solves for a given active tension under consideration of the boundary conditions and further input variables e.g. blood pressure, the following system of nonlinear equations for the displacement for each time step.

$$\mathbf{f}_{total}(\mathbf{d}) = 0 \quad (12.10)$$

This is done by using the Newton implementation of the PETSc library. For this, the solver has to provide the nodal forces and the Jacobian matrix of the nodal forces also referred to as *tangential stiffness matrix*

$$\mathbf{K} = \frac{\partial \mathbf{f}_{total}}{\partial \mathbf{d}} \quad (12.11)$$

The Jacobian matrix is calculated element-wise using central finite differences. For nodes, which are defined to be fixated (Dirichlet boundary conditions for the displacement), the corresponding entries of \mathbf{f}_{total} are set to zero. In the Jacobian matrix, the respective rows and columns are set to zero and the diagonal element to one. The solver uses adaptive time stepping depending on the convergence of the Newton method. If the static solver does not come to a solution within the defined maximal number of Newton steps, the time step size is divided by two and the computation is

restarted. Otherwise, if the time step size is smaller than a defined maximal time step size and if the solver has converged successfully for a defined amount of successive time steps, the time step size is doubled. All input data e.g. the active tension is updated for each time step and interpolated if necessary.

The Dynamic Solver based on Newmark-Beta Time Integration

The dynamic solver takes into account mass inertia and damping. For that purpose, the mass matrix \mathbf{M}

$$M_{i_j I J} = \delta_{ij} \int_{\Omega_0} \rho_0 N_I N_J d\Omega_0 \quad (12.12)$$

$$(12.13)$$

and the Rayleigh damping matrix \mathbf{C} (see Sec. 6.1).

$$\mathbf{C} = \alpha_1 \mathbf{M} + \alpha_2 \mathbf{K} \quad (12.14)$$

are computed.

For the time integration, the Newmark-Beta scheme is used (see Sec. 6.1). The following nonlinear system of equations

$$\begin{aligned} \mathbf{r}(\mathbf{d}^{n+1}) &= \mathbf{M} \frac{1}{\beta \Delta t^2} (\mathbf{d}^{n+1} - \mathbf{d}^n + \Delta t \mathbf{v}^n + \frac{\Delta t^2}{2} (1 - 2\beta) \mathbf{a}^n) + \mathbf{f}_{total}(\mathbf{d}^{n+1}, t^{n+1}) \\ &+ \mathbf{C} \frac{1}{\beta \Delta t^2} (\beta \Delta t^2 (\mathbf{v}^n + (1 - \gamma) \Delta t \mathbf{a}^n) + \mathbf{d}^{n+1} - \mathbf{d}^n + \Delta t \mathbf{v}^n + \frac{\Delta t^2}{2} (1 - 2\beta) \mathbf{a}^n) = 0 \end{aligned} \quad (12.15)$$

has to be solved for the displacement \mathbf{d}_{n+1} using Newton method. The Jacobian matrix \mathbf{A} is given by

$$\mathbf{A} = \frac{1}{\beta \Delta t^2} (\mathbf{M} + \mathbf{C}) + \mathbf{K} \quad (12.16)$$

Boundary conditions for the nodal displacement are incorporated in the same way as for the static solver. Eventually, the corresponding updated velocity and acceleration for time step t_{n+1} are computed as follows

$$\mathbf{a}^{n+1} = \frac{1}{\beta \Delta t^2} (\mathbf{d}^{n+1} - \mathbf{d}^n + \Delta t \mathbf{v}^n + \frac{\Delta t^2}{2} (1 - 2\beta) \mathbf{a}^n) \quad (12.17)$$

$$\mathbf{v}^{n+1} = \mathbf{v}^n + (1 - \gamma) \Delta t \mathbf{a}^n + \gamma \Delta t \mathbf{a}^{n+1} \quad (12.18)$$

The dynamic solver uses the same adaptive time stepping as the static solver.

Solver Plugins

Different solver modules can be linked to the solver via the plugin interface. This allows to extend the biomechanical solver by coupling it with other modules (e.g. model of the circulatory system) without the need to modify the respective source code. A solver module must provide the additional nodal forces and their Jacobian matrix for a given displacement. These nodal forces are added to the total nodal forces \mathbf{f}_{total} and the entries of the Jacobian matrix are added to \mathbf{K} .

The plugin module must be designed in such a way, that if the same time step is repeated for example because the solver did not converge and hence the time step size was reduced, all state variables which have been updated after the previous execution, are restored.

In the next two chapters, the plugin modules for the modeling of the circulatory system and the contact handling are described.

Chapter 13

Implementation of the Circulatory System Model

13.1 Modeling of the Intraventricular Pressure

The ventricles of the biomechanical model can be coupled with a lumped three-element Windkessel model. For this, a closed triangle surface has to be defined for each cavity which is taken into account. That surface must only consist of nodes of the tetrahedral mesh. All openings have to be closed by triangularization without adding any further nodes. The cavity surfaces are used on the one hand, to determine the respective cavity volume, on the other hand, they are used to calculate the nodal forces which act on the nodes of the respective chamber, due to the pressure. In the following the circulation model for the left ventricle is described. The circulation model of the right ventricle works analogously. The circulatory system model has already been presented in the publication (Fritz et al., 2013). This chapter is in part based on the respective section of that publication.

The equation of the Windkessel model is given by:

$$\left(1 + \frac{R_2}{R_1}\right) I(t) + CR_2 \frac{dI(t)}{dt} - C \frac{dP_{ar}(t)}{dt} - \frac{P_{ar}(t)}{R_1} = 0 \quad (13.1)$$

where I describes the blood flow from the ventricle into the aorta, P_{ar} describes the aortic pressure. Capacitor C describes the compliance of the aorta and the large elastic arteries. Resistor R_2 describes the flow resistance of the aorta and R_1 describes the peripheral resistance.

Four different states of the cardiac cycle are considered:

Isovolumetric Contraction:

All valves are closed. The heart starts to contract, but since no blood can leave or enter the ventricle, this happens isovolumetrically, while the intraventricular pressure increases rapidly. A penalty term (Eq. 13.7) (*Isovolumetric Contraction*) is responsible for retaining the volume (almost) constant during the isovolumetric contraction by applying the needed pressure to the ventricle. The pressure in the aorta is given by Eq. 13.1 while the blood flow into the aorta is zero $I = 0$.

Ejection:

When the ventricular pressure exceeds the pressure in the aorta, the aortic valve opens. Now, ventricular and arterial pressure are assumed to be equal and given by Eq. 13.1. The blood flow into the aorta is the negative first time derivate of the ventricular volume.

$$I(t) = -\frac{d}{dt}V_{ven}(t) \quad (13.2)$$

Isovolumetric Relaxation:

In reality, the aortic valve closes, when the ventricular pressure falls below the aortic pressure. However, in the present model, the aortic and ventricular pressure are equal during the ejection state. Therefore, the valve is defined to close, when the ventricular volume reaches its minimum and the isovolumetric relaxation begins. Then, the aortic pressure is described by Eq. 13.1 while $I = 0$. The ventricular volume is retained almost constant by a penalty term analogously to the isovolumetric contraction Eq. 13.7 (*isovolumetric relaxation*). At that time, the active tension has already passed its peak value declines. This causes a rapid pressure drop in the ventricle.

Filling:

After the ventricular pressure falls below a defined value, the filling phase starts. The atrial valve is open and blood flows from the atrium into the ventricle. The remaining ventricular pressure as well as the passive stress within the myocardium cause that the ventricle returns to its end-diastolic state. The ventricular pressure further declines according to the following equation until a defined end-diastolic pressure is reached. Then the pressure is remained constant until the next contraction begins.

$$\frac{d}{dt}P_{ven} = \begin{cases} -\beta(P_{ven} - P_{res}) - \gamma \frac{d}{dt}V_{ven} & \text{for } P_{ven} > P_{res} \\ 0 & \text{otherwise} \end{cases} \quad (13.3)$$

This equation has no direct physiological correspondence and shall just decrease the remaining pressure until the residual end-diastolic pressure P_{res} is reached. In reality, the pressure conditions are much more complex. On the one hand the ventricle relaxes, since the active tension declines, which causes a rapid pressure drop, but on the other hand blood flows from the atria into the ventricle which counteracts the decrease of pressure. However, since the pressure is rather small (< 15 mmHg), the simplification should be acceptable.

Euler time integration

Equation 13.1 is discretized using an Euler scheme:

$$P_{ar}^{n+1} = P_{ar}^n - \frac{P_{ar}^n \Delta t^{n+1}}{R_1 C} - \left(1 + \frac{R_2}{R_1}\right) \frac{\Delta V^{n+1}}{C} - R_2 \left(\frac{\Delta V^{n+1}}{\Delta t^{n+1}} - \frac{\Delta V^n}{\Delta t^n}\right) \quad (13.4)$$

where

$$\Delta t^n = t^n - t^{n-1} \quad \text{and} \quad \Delta V^n = (V_{ven}^n - V_{ven}^{n-1}) \quad (13.5)$$

during ejection phase. Otherwise it is $\Delta V^n = 0$. The time step size Δt^n is variable since the biomechanical solver uses an adaptive time stepping scheme.

The equation Eq. 13.4 for the pressure decay during the filling phase is discretized analogously.

The volume of the ventricular cavity is represented by a triangle mesh and is calculated as follows:

$$V = \sum_k \frac{1}{3} A_k \mathbf{b}_k \mathbf{n}_k \quad (13.6)$$

where \mathbf{n}_k is the outward-pointing normal vector, \mathbf{b}_k is the centroid and A_k is the area of the surface triangle element k . The updated intraventricular pressure P_{ven}^{n+1} is calculated as follows:

$$P_{ven}^{n+1} = \begin{cases} -K \left(\frac{V(t)}{V_d} - 1 \right) & \text{isovolumetric contraction} \\ P_{ar}^{n+1} & \text{ejection phase} \\ -K \left(\frac{V(t)}{V_s} - 1 \right) & \text{isovolumetric relaxation} \\ P_{ven}^n - \beta (P_{ven} - P_{res}) \Delta t - \gamma \Delta V & \text{filling phase} \end{cases} \quad (13.7)$$

If $P_{ven}^{n+1} < P_{res}$ after the filling phase, then P_{ven}^{n+1} is set to P_{res} until the next contraction starts. The variable V_d and V_s describe the end-diastolic volume and end-systolic volume. These volumes are remained constant during the isovolumetric phases using a penalty approach. The circulatory system model is implemented as a solver plugin module and has to provide for each time step the forces which act on the nodes of the cavities and the nodal forces Jacobian matrix for a given displacement vector. The displacement defines the current volume of the cavity and in combination with the volume values of the previous time steps, it allows to calculate the blood flow $I(t)$ and its first and second time derivative. The nodal forces which are applied to vertex I , as result of the pressure which acts on the cavity surface element k are calculated as follows:

$$\mathbf{f}_{kl} = \frac{1}{3} P_{ven} A_k \mathbf{n}_k \quad (13.8)$$

The Jacobian matrix is given by

$$\frac{\partial \mathbf{f}_{kl}}{\partial X_J} = \frac{1}{3} \left(A_k \mathbf{n}_k \frac{dP_{ven}}{dV} \frac{\partial V}{\partial X_J} + P_{ven} \frac{\partial}{\partial X_J} (A_k \mathbf{n}_k) \right) \quad (13.9)$$

where $\frac{\partial V}{\partial X_J}$ and $\frac{\partial}{\partial X_J} (A_k \mathbf{n}_k)$ were calculated using finite differences and the derivate $\frac{dP_{ven}}{dV}$ is given by

$$\frac{dP_{ven}}{dV} = \begin{cases} -\frac{K}{V_0} & \text{isovolumetric contr.} \\ -(1 + \frac{R_2}{R_1}) \frac{1}{C} - \frac{R_2}{\Delta t^{n+1}} & \text{ejection phase} \\ -\frac{K}{V_1} & \text{isovolumetric relax.} \\ -\gamma \text{ or } 0 \text{ if } P_{ven} \leq P_{res} & \text{filling phase} \end{cases} \quad (13.10)$$

The strong coupling of the Windkessel model and the biomechanical model in one system of nonlinear equation results in a great numerical stability. However, the nodal force which acts on a node of the cavity depends on the pressure in that cavity which itself depends on the volume change and therefore on the displacement of all nodes. Consequently, the strong coupling causes dense blocks for each cavity in the Jacobian matrix which is not so nice from a numerical point of view, when it comes to the solving of the linear system of equations for the Newton steps. The circulatory system model in the present state does only support T3 triangle elements. However, it would be a simple task to extend it to T6 triangle elements, but this has not done yet.

13.2 Modeling of Atrial Pressure

For modeling the atrial pressure, a two element Windkessel model is used (Eq. 13.1 with $R_2 = 0$). In this case, the current I represents the blow flow from the atrium into the ventricle and C can be interpreted as the compliance of that ventricle. The resistor R_1 can be interpreted as the flow

resistance of that ventricle. However, one has to be careful with a direct physical correspondence, In reality, the atrial pressure profile during the whole heart cycle is quite complex, since atria and ventricles interact with each other. In filling phase, the ventricles are deformed due to the blood flow from the atria and the atrial contraction. During the isovolumetric contraction phase of the ventricles, the atrial pressure is temporarily increased. When the ventricular pressure exceeds the aortic pressure, the aortic valve opens and the atrioventricular plane moves downwards the apex which causes a stretching of the atria which increases their volumes and rapidly reduces their pressure. This facilitates the inflow of blood from the venae cavae and the vessels into the atria, which eventually causes an increase in pressure. A complete description of the atrial and ventricular blood pressure with all valve states and the filling of the atria via the pulmonary veins would involve the coupling of a Windkessel model of the atria with a Windkessel model of the ventricles as well as with a model of the blood flow from the vessels. This is a very complex and numerical demanding task. For the projects in this work, I used the following simplification: Since the ventricles are not significantly deformed during the atrial contraction and the atrial pressure during the ventricular contraction is relatively low compared to the ventricular pressure, the ventricular circulatory model is deactivated during the atrial contraction and the atrial model is deactivated during the ventricular contraction. Accordingly, only the afterload during the atrial contraction from the perspective of the atrium can be simulated. Consequently, the atrial contraction has no impact on the intraventricular pressure.

This is a significant limitation and should always kept in mind for the interpretation of the results. However, if the focus lies on the atrial contraction only this simplification can be justified.

13.3 Initialization of the Circulatory System model

The heart in end-diastolic state is not stress-free and a residual pressure is acting on the end-diastolic ventricles. However, applying that pressure to the end-diastolic heart model, which was generated based on the end-diastolic MRI data, would result in an unwanted inflation of the ventricles,

with the result, that the diastolic state of the heart would not match to the MRI data anymore. For that reason, that stress-free configuration of the heart has to be found which deforms to the correct diastolic state when the residual pressure is applied. This is achieved by applying a negative pressure to the ventricles, which causes a slight deflation. Eventually, the resulting geometry is taken as the initial geometry. At the beginning of the simulation, the circulatory system model is in state *isovolumetric contraction*. Accordingly, the circulatory system model generates that pressure which keeps the cavity volume approximately constant and equal to the end-diastolic volume. The volumes of the ventricles in the initial geometry are smaller than the end-diastolic volumes. This results in an initial pressure and an inflation of the ventricles. Eventually, the cavities of the ventricles have the correct volumes and the geometry is almost identical to the end-diastolic state. The negative pressure has to be adapted in such a way that finally the residual pressure in the ventricles has the desired value.

Chapter 14

Implementation of the Contact Handling

As explained in Sec. 17 the pericardium consists of two layers, the epicardium which is connected to the myocardium and the parietal pericardium which can slide on each other. However, in order to make things easier, I will refer to the epicardium in the following as the heart surface of just the heart and to the parietal pericardium just as the pericardium. Accordingly I will say that "the heart slides on the pericardium", even though this is not completely correct according to the definition of the pericardium.

The pericardium restricts the motion of the heart during the contraction but also during the filling phase. Apart from that, it promotes the interaction of the left and right ventricle. Accordingly, the pericardium plays an important role for the cardiac biomechanics which motivates to take it into account for biomechanical simulations.

In order to model the contact of heart and pericardium, I have developed and implemented a contact handling algorithm, which ensures permanent and frictionless contact between the heart and the pericardium based on a classical contact formulation using penalty regularization (see also (Wriggers, 2006)). The pericardium model has already been presented in (Fritz et al., 2013). This chapter is partially based on the respective section of that publication.

As described in Sec. 10, the geometrical model of the heart includes a

tetrahedral mesh, which represents the tissue in which the heart is embedded. The pericardium is represented by the inner surface of that mesh, defined by a closed triangular mesh, while its vertices are the respective surface nodes of the T10 tetrahedral elements (Fig. 14.1). In this sense, the pericardium itself does not have a volumetric representation. However, in the following, I will refer to the mesh of the surrounding tissue in combination with the triangular surface as the pericardium mesh or just the pericardium. The mesh of the heart and the mesh of the pericardium are non-conforming and non-overlapping. The contact interface between the heart and the pericardium consists of two surfaces, the surface of the heart referred to as the *master surface* and the inner surface of the mesh which represents the surrounding tissue named *slave surface*. The triangle elements of the master surface are the *master elements* and the triangle elements of the slave surface are the *slave elements*. In order to determine the contact forces, a contact potential is defined for which the first variation is given by

$$\delta W_C = \delta \left(\frac{1}{2} \int_{\Omega_C} \varepsilon g_N(\xi)^2 d\Omega_C \right) \quad (14.1)$$

where Ω_C is the common contact surface, ε is the penalty parameter and g_N the gap function given by (Wriggers, 2006, sec. 4.1, p. 58-60 and sec. 6.3.2, p. 118)

$$g_N(\xi) = (\mathbf{x}^s(\xi) - \mathbf{x}^m(\xi)) \cdot \mathbf{n}^m(\xi) \quad (14.2)$$

The point \mathbf{x}^m lies on the master surface. Its position is given in surface coordinates ξ . The projection of \mathbf{x}^m in direction of the master surface normal \mathbf{n}^m at \mathbf{x}^m defines \mathbf{x}^s .

All triangles of the inner surface of the pericardium mesh were defined to be the slave elements of the contact interface. Since the contact handling algorithm shall ensure permanent contact, it would not be clever, to take all surface elements of the heart for the master surface, since in that case, the contact condition could either not be fulfilled or result in an unrealistic deformation. For that reason, only those surface elements of

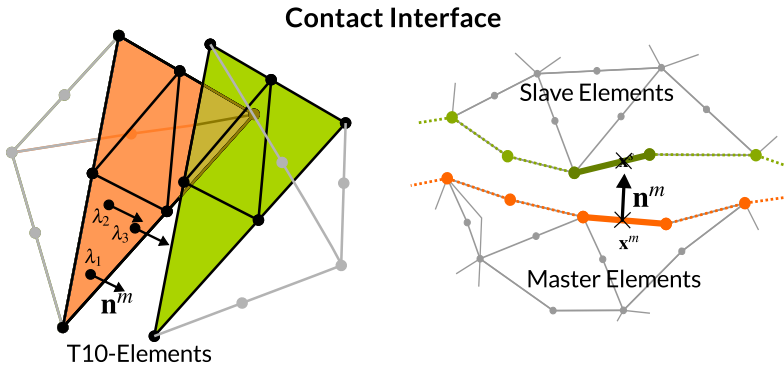


Figure 14.1: The vertices of the T10 elements, which belong to the contact interface define the triangles, which are used to discretized the contact interface

the heart surface, which had contact, or were closer to the slave surface than a defined distance in the reference configuration are considered for the contact interface (Fig. 14.2).

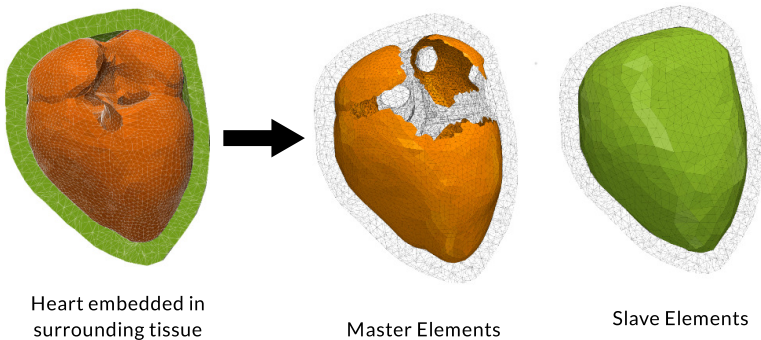


Figure 14.2: The triangles meshes, which define the master and slave contact interface. Only those triangle elements of the heart surface, which are closer than a defined distance, are chosen for the master surface

Equation Eq. 14.1 can be transformed into

$$\delta W_C = \varepsilon \int_{\Omega_C} g_N(\xi) (\delta \mathbf{x}^s(\xi)) \cdot \mathbf{n}^m(\xi) d\Omega_C \quad (14.3)$$

$$\underbrace{\hspace{10em}}_{\text{master contact forces}}$$

$$- \varepsilon \int_{\Omega_C} g_N(\xi) (\delta \mathbf{x}^m(\xi)) \cdot \mathbf{n}^m(\xi) d\Omega_C. \quad (14.4)$$

$$\underbrace{\hspace{10em}}_{\text{slave contact forces}}$$

With the following interpolations

$$\delta \mathbf{x}(\xi) = \sum_I N_I(\xi) \delta \mathbf{x}_I \quad (14.5)$$

$$g_N(\xi) \mathbf{n}(\xi) = \sum_J N_J(\xi) g_{N,J} \mathbf{n}_J \quad (14.6)$$

we obtain the nodal contact force contribution of the master elements (here node I belongs to the master surface) from Eq. 14.1

$$\mathbf{f}_I^m = \varepsilon \int_{\Omega_C} \sum_J N_I N_J g_{N,J} \mathbf{n}_J d\Omega_C \quad (14.7)$$

Linear triangular shape functions are used. The contact integral is computed using Gauss quadrature while the integral is evaluated at three quadrature points. For this, at each of the three quadrature points of the master element, the closest slave element which intersects with a line through the quadrature point in direction of the master element surface normal has to be determined. Accordingly, one master element can interact with up to three slave elements (*partner slave elements*). After determining all partner slave elements, the surface integral for the nodal contact forces of the master element is computed. The computation of the surface integral for the slave elements is not trivial, since the slave elements and the master elements are non-conforming. To solve the integral for the slave elements would involve to create auxiliary sub triangles which describe the overlap of the slave element with the master elements. However, for the purpose of ensuring contact between heart and pericardium it is not essential to obtain an absolutely exact distribution of the contact forces. For that reason, the

contact forces of the slave elements are calculated using the following scheme. For all master elements, for which the respective slave element is a partner slave element, the equivalent nodal contact force is given by

$$\mathbf{f}^K = \frac{1}{3} g_N(\mathbf{q}^K) A^K \mathbf{n}^K \quad (14.8)$$

where \mathbf{q}^K is the position of the quadrature point K , A^K is the area of the element to which K belongs to and \mathbf{n}^K is the normal vector of that element. The forces at the quadrature point K (here K belongs to the set of all the quadrature points of all involved master elements) are distributed to the vertices of its corresponding slave element using the following scheme (Fig. 14.3). The area A^L of the slave element L is subdivided in the sub-areas $a_{I,K}^L$ by connecting the intersection point of the line through the respective quadrature point J of master element in direction of the normal of the master element with the vertices of the slave element. Then the nodal contact force contribution \mathbf{f}_I^L of the slave element L is calculated as follows

$$\mathbf{f}_I^L = \sum_K -\mathbf{f}_J^K \cdot \frac{a_{I,K}^L}{A^L} \quad (14.9)$$

The nodal contact force \mathbf{f}_I^s (I belongs to the slave surface) is the total of all involved slave elements contributions.

$$\mathbf{f}_I^s = \sum_L \mathbf{f}_I^L \quad (14.10)$$

The nodal contact forces Jacobian is calculated using central finite differences.

At the beginning of the simulation, the initial master and slave surfaces do usually not match completely to each other. This results in a slight deformation and a residual contact pressure. If desired, the residual pressure can be removed, by using the resulting mesh as reference configuration and accordingly by recalculating the shape function derivatives the new

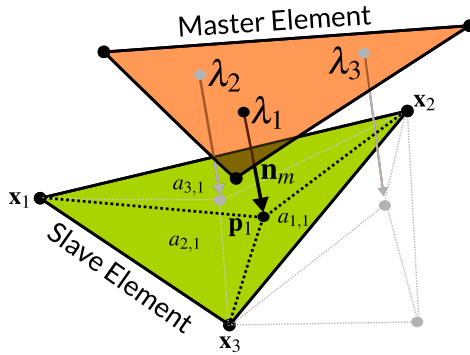


Figure 14.3: Distribution of the contact forces at the quadrature points of the master element to the vertices of the slave element

coordinates of the mesh nodes. End-diastolic contact pressure can be considered in the simulation, by introducing a small gap between the slave elements and master element in the geometrical model. A disadvantage of the penalty method is, that a good value for the penalty parameter has to be found. If the parameter is too small, the contact condition is not fulfilled satisfactorily. But, a too big parameter increases the condition number of the system matrix and therefore might cause numerical problems.

Chapter 15

The Inverse Solver

15.1 Introduction

The static and the dynamic solver calculate the deformation of the heart which results from the active tension distribution. In an opposite manner, the inverse solver, which I have developed and implemented in context of this work, allows to estimate the active tension distribution from the motion of the heart surfaces. The idea is inspired by the work of my dear colleagues Walther Schulze and Danila Potyagaylo, who deal with the *inverse problem of ECG imaging*. Here, the aim is to determine the electrical activity of the heart from the measured electrical activity on the body surface (Farina, 2008). While it is easy to compute the electrical potentials on the body surface which results from the electrical activation of the heart, the other way round is usually an ill-posed problem and regularization is required. The reconstruction of the active tension distribution from measurable data of the heart deformation (e.g. motion of the heart surfaces or strain data) can be compared to the reconstruction of the electrical potentials of the heart from the the body surface potential distribution, which is measured with different electrodes on the body surface. A lead field matrix \mathbf{A} is computed, which allows to determine the potential at the position of the electrodes, resulting from the electrical activity of the heart. This matrix is usually not of full rank and thus not invertible. To solve the inverse problem in order to obtain the electrical activity of the heart, a commonly

used method is Tikhonov regularization (Tikhonov and Arsenin, 1977). In a similar manner, the inverse problem of cardiac mechanics is solved using the algorithm presented in this chapter. However, in contrast to the inverse problem of ECG imaging, this problem is nonlinear. For that reason, the problem has to be solved iteratively. The input data is the motion of defined heart surfaces. For each time step, the active tension, which results in the desired displacement of the heart surfaces is optimized iteratively based on a Tikhonov approach with spatial and temporal regularization. Analogous to the lead field matrix, a linearized matrix, which describes the displacement of the heart surface due to a change of the active tension is computed for each iteration step. A visualization of the work flow is given in figure Fig. 15.1.

15.2 The Algorithm of the Inverse Solver

Input Data

Two data sets have to be provided: namely the *target surface data* and the *source surface data*.

Target surface data

The target surface data is defined by triangle meshes (target elements) and the trajectories of their nodes. They describe the motion of selected heart surfaces e.g. the endocardium of the left and right ventricle. This target surfaces could for example be extracted from 4D cine MRI or 4D cardioechography. Here, it is sufficient, that the target surfaces match to the heart surfaces, while it is not necessary, that the nodes of the target surfaces have the same trajectories as the corresponding *real* points of the heart surface.

Source surface data

The source surface data also consists of triangle meshes (source elements), while their nodes are a subset of the nodes of the tetrahedral mesh which represents the heart geometry. Each source surface has a corresponding

target surface, for example, the source surface which represents the left ventricular endocardium has a corresponding target surface which describes the motion of the left ventricular endocardium. Apart from the target and source surfaces, the solver must be advised for which material classes of the heart geometry we ask it to reconstruct the active tension. Then, the inverse solver determines all elements which have one of the selected material classes (usually the elements of the left and right ventricle). In the following, these elements are defined to be the *elements of interest* and their nodes as *nodes of interest*. The amount of elements of interest is represented by the value M . Apart from that, the inverse solver selects all nodes from the source surfaces which belong to at least one of the elements. These are the *source nodes*. Furthermore, it is necessary to introduce the *evaluation points* which are a subset of the source nodes. The number of evaluation point components (three components per point) is represented by the value N . It would of course be possible to select all nodes of the source surfaces as evaluation points, but we will see that the whole inverse algorithm is very numerical demanding, and therefore it is necessary to reduce the problem wherever it is possible and reasonable. The evaluation points can either be defined manually by providing the indices, or the inverse solver chooses randomly but deterministic (the random number generator is always initialized with the same seed in order to grant the reproducibility) the evaluation points from the source nodes. In this case, it is necessary to check, if the selected evaluation points are more or less evenly distributed.

Inverse solution

Figure 15.1 shows a flowchart of the inverse solver. For each time step t_i , multiple alternating static solver and estimator steps are performed. Thereby, the static solver determines the deformation due to the active tension. Based on the output, the estimator step optimizes the active tension. The respective iteration is indicated by the index n starting with $n = 0$. At the beginning of each time step ($n = 0$), the target surfaces are updated regarding the locations of their nodes. If the locations of the nodes are not available for the respective time step, they are interpolated linearly. First, for each iteration n , a full static solver step is executed.

The intraventricular pressure should be provided by a pressure time curve which is synchronized to the target surface motion. It is also possible to use the Windkessel model, but this will introduce further unknowns. Moreover, it can destabilize the inverse solution.

The following steps are performed for each iteration n until one of the defined stop criteria is fulfilled. For each source triangle which contains at least one of the evaluation points as vertex, the distances of the evaluation points to the corresponding target surface are determined. For this purpose, for each of the evaluation points of the element, the closest target element which is intersected by a line through that point in direction of the normal of the source element is determined and for that element the distance vector between the intersection point and the evaluation point is determined. Most of the evaluation points of the surface mesh belong to more than one triangle. For these points, the average of the distance vectors of all elements it belongs to is calculated. The components of the distance vectors are stored in the vector $\mathbf{g}_{i,n}$. Accordingly, the number of components of $\mathbf{g}_{i,n}$ is three times the amount of evaluation points. Now, it can happen that for some of the evaluation points, no target element can be found. If this is the case, this evaluation point is removed temporarily from the list for the iteration step n . As a matter of course, the vector $\mathbf{g}_{i,n}$ is also that displacement of the evaluation points we would like to see after the optimization of the active tension. For that reason, the aim of the inverse solver is to find an active tension distribution which minimizes $\mathbf{g}_{i,n}$. For that purpose, it is necessary to analyse how $\mathbf{g}_{i,n}$ depends on the active tension \mathbf{T} of the elements of interest.

In general, the linearized relation of a small change of the nodal displacement $\Delta\mathbf{d}$ and the resulting change of the nodal forces $\Delta\mathbf{f}$ is given by

$$\mathbf{K}_d\Delta\mathbf{d} = \Delta\mathbf{f} \quad (15.1)$$

$$\text{where } \mathbf{K}_d = \frac{\partial\mathbf{f}}{\partial\mathbf{d}} \quad (15.2)$$

The vector \mathbf{d} is the displacement from reference configuration to the current configuration and $\Delta\mathbf{d}$ is a displacement from the current configuration $\mathbf{d}' = \mathbf{d} + \Delta\mathbf{d}$. Since we are only interested in the displacement of the nodes

of interest represented by $\Delta\hat{\mathbf{d}}$ and their nodal forces $\hat{\mathbf{f}}$ we can extract the corresponding submatrix from \mathbf{K}_d and obtain

$$\hat{\mathbf{K}}_d \Delta\hat{\mathbf{d}} = \Delta\hat{\mathbf{f}} \quad (15.3)$$

By calculating the inverse of $\hat{\mathbf{K}}_d$, we can approximate the displacement $\Delta\hat{\mathbf{d}}$ of the nodes of interest which results from a change of the nodal forces as follows

$$\Delta\hat{\mathbf{d}} \approx \hat{\mathbf{K}}_d^{-1} \Delta\hat{\mathbf{f}} \quad (15.4)$$

For a small change $\tau_{i,n}$ of the active tension within an iteration n ($\mathbf{T}_{i,n+1} = \mathbf{T}_{i,n} + \tau_{i,n}$), the approximate displacement is given by

$$\Delta\hat{\mathbf{d}} \approx \hat{\mathbf{K}}_d^{-1} \hat{\mathbf{K}}_T \cdot \tau_{i,n} \quad (15.5)$$

$$(15.6)$$

The index i represents the time step t_i and n represents the inverse solver iteration. $\hat{\mathbf{K}}_T$ is a submatrix of \mathbf{K}_T

$$\mathbf{K}_T = \frac{\partial \mathbf{f}(\mathbf{T})}{\partial \mathbf{T}} \quad (15.7)$$

and consists only of those rows and columns of \mathbf{K}_T which are associated to the nodes and elements of interest. The matrix \mathbf{K}_T is calculated using central finite differences.

In general, the calculation of the inverse of a matrix is numerical demanding. But since we are only interested in the displacement $\mathbf{g}_{i,n}$ for the evaluation points, it is sufficient to determine a reduced inverse \mathbf{L} which consists only of those rows of $\hat{\mathbf{K}}_d^{-1}$ which are associated with the evaluation points. The rows $\mathbf{L}_{j,*}$ of the reduced inverse are calculated by solving the following linear system of equations.

$$\hat{\mathbf{K}}_d^T \cdot \mathbf{L}^T_{j,*} = [0, 0, \dots, 1(\text{component } j), \dots, 0, 0]^T \quad (15.8)$$

In total, N rows have to be calculated, three for each evaluation point. This procedure is speeded up by precomputing the LU decomposition of $\hat{\mathbf{K}}_d^T$. In order to decrease the numerical complexity of the estimation step, the implementation of the inverse solver allows to use T10 tetrahedral elements for the static solver step but to use T4 elements for the calculation of the estimation step.

Eventually we obtain the following system of linear equations for $\tau_{i,n}$

$$\mathbf{A} \tau_{i,n} = \mathbf{g}_{i,n} \quad (15.9)$$

where \mathbf{A} is given by

$$\mathbf{A} = \mathbf{L} \cdot \hat{\mathbf{K}}_{\mathbf{T}} [N \times M] \quad (15.10)$$

This problem is usually ill-posed and regularization is necessary. For that purpose, the following Tikhonov based approach has been implemented for the inverse solver, which allows to regularize the solution regarding different aspects:

$$\begin{aligned} & \min(\|\mathbf{A} \tau_{i,n} - \mathbf{g}_{i,n}\|^2 \\ & + \lambda_1 \|\tau_{i,n}\|^2 \\ & + \lambda_2 \|\mathbf{T}_{i,n} + \tau_{i,n}\|^2 \\ & + \lambda_3 \frac{1}{\Delta t} \|\mathbf{T}_{i,n} + \tau_{i,n} - \mathbf{T}_{i-1,n}\|^2 \\ & + \lambda_4 \frac{1}{\Delta t^2} \|\mathbf{T}_{i,n} + \tau_{i,n} - 2\mathbf{T}_{i-1,n} + \mathbf{T}_{i-2,n}\|^2 \\ & + \lambda_5 \|(\Delta_c \tau_{i,n})\|^2 \\ & + \lambda_6 \|\Delta_c(\tau_{i,n} + \mathbf{T}_{i,n})\|^2 \\ & + \lambda_7 \|\Delta_c(\mathbf{T}_{i,n} + \tau_{i,n} - \mathbf{T}_{i-1,n})\|^2) \end{aligned} \quad (15.11)$$

where

$$\Delta t = t_i - t_{i-1} \quad (15.12)$$

The penalty parameter λ_1 controls the regularization regarding the change of $T_{i,n}$ within one iteration. The term with λ_2 regularizes regarding the norm of the active tension $\mathbf{T}_{i,n+1}$. The term with parameter λ_3 regularizes regarding the change of the active tension between two time steps. The term with λ_4 regularizes regarding the second time derivate of the tension development and thus controls the smoothness of the time course of the active tension. The matrix Δ_c is the discretized Laplace operator generated from the connectivity matrix of elements. It considers only the neighborhood relationship of the elements, but not their size and shape. The parameter λ_5 regularizes regarding the spatial smoothness of $\tau_{i,n}$ within one iteration. The parameter λ_6 regularizes regarding the smoothness of the active tension development and λ_7 regularizes regarding the smoothness of the change of the active tension development. If all λ but λ_1 are zero, we obtain 1st order Tikhonov regularization which penalizes the norm $\tau_{i,n}$. If all λ but λ_5 are set to zero we have second order Tikhonov regularization regarding the spatial smoothness of τ . In general, a good value for the penalty parameter has to be found which is not trivial. It makes certainly no sense to set all λ parameter unequal to zero. The optimal combination of regularization terms depends on the problem. For the reconstruction of the ventricular active tension, I obtained good results with the combination of λ_6 (spatial smoothing of the active tension) and λ_4 (temporal smoothing of the active tension time course), while all other parameter were set to zero.

The minimum of Eq. 15.11 is determined by setting the derivative regarding $\tau_{i,n}$ to zero. From this follows

$$\begin{aligned}
 & (\mathbf{A}^T \mathbf{A} + (\lambda_1 + \lambda_2 + \frac{\lambda_3}{\Delta t} + \frac{\lambda_4}{\Delta t^2}) \mathbf{E} + (\lambda_5 + \lambda_6 + \lambda_7) \Delta_c) \tau_{i,n} = \\
 & \mathbf{A}^T \mathbf{g}_{i,n} - \lambda_2 \mathbf{T}_{i,n} - \lambda_3 \frac{1}{\Delta t} (\mathbf{T}_{i,n} - \mathbf{T}_{i-1,n}) - \lambda_4 \frac{1}{\Delta t^2} (\mathbf{T}_{i,n} - 2\mathbf{T}_{i-1,n} + \mathbf{T}_{i-2,n}) \\
 & - \lambda_6 \Delta_c \mathbf{T}_{i,n} - \lambda_7 \Delta_c (\mathbf{T}_{i,n} - \mathbf{T}_{i-1,n})
 \end{aligned} \tag{15.13}$$

This equation is solved for each estimator step and $\tau_{i,n}$ is added to the current active tension.

$$\mathbf{T}_{i,n+1} = \mathbf{T}_{i,n} + \boldsymbol{\tau}_{i,n} \quad (15.14)$$

But beforehand, it is checked if all components of $\mathbf{T}_{i,n}$ and of the difference $\mathbf{T}_{i,n} - \mathbf{T}_{i-1,n}$ will lay within defined boundaries after the addition of $\boldsymbol{\tau}_{i,n}$: The components must be greater than zero and smaller or equal to a maximal value. The absolute value of the difference between two steps must be smaller than a defined maximal value. If this is not the case, the respective components of $\boldsymbol{\tau}_{i,n}$ are adapted in such a way, that these limits are respected.

Eventually, the next iteration is performed. Here, n is increased by one and the static solver computes the displacement due to the updated active tension. From the results, $\mathbf{g}_{i,n}$ is determined and used to further optimize the active tension distribution.

This loop continues until one of the stop criteria is fulfilled. This is the case when

$$\mathbf{g}_{i,n} < \boldsymbol{\varepsilon}_{abs} \vee |\mathbf{g}_{i,n} - \mathbf{g}_{i,n-1}| < \boldsymbol{\varepsilon}_{rel} \vee n \geq n_{max} \quad (15.15)$$

Eventually, the active tension is updated for the next time step:

$$\mathbf{T}_{i+1,0} = \mathbf{T}_{i,n} \quad (15.16)$$

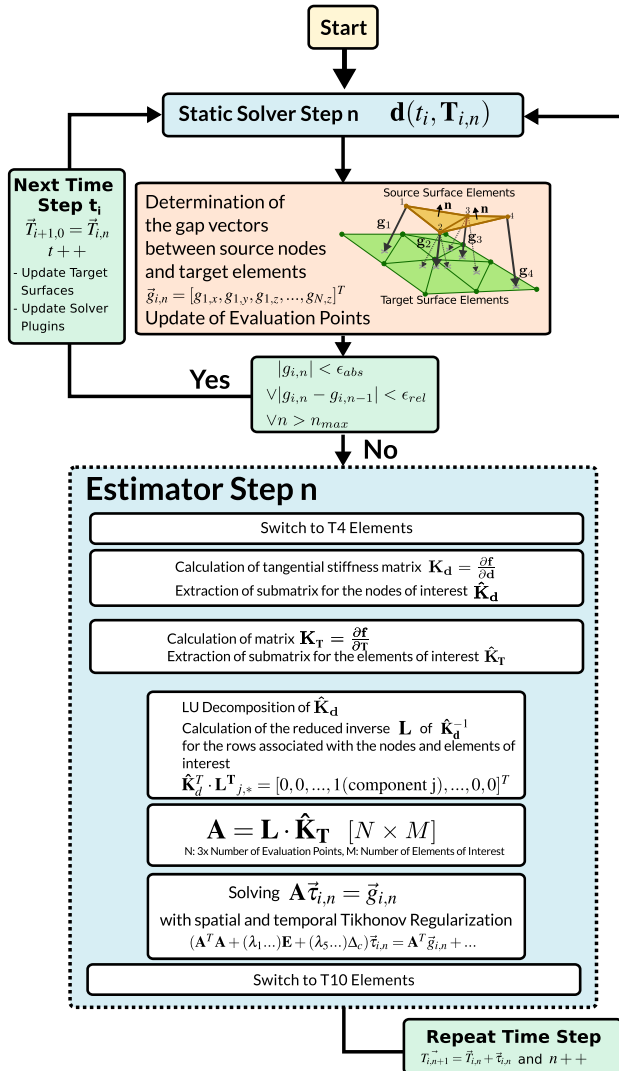


Figure 15.1: Flowchart of the inverse solver

PART III

PROJECTS

Chapter 16

Validation of the Biomechanical Simulation Framework

16.1 Validation

The implementation of the biomechanical simulation framework had been tested and validated continuously during the development process using different test settings. In this chapter, I present four validation tests which cover some of the most important aspects. In order to analyze the convergence of the linear tetrahedral elements and quadratic tetrahedral elements, the bending of a bar due to pressure which is applied to its bottom surface, is simulated for different mesh resolutions.

To validate the implementation of the material models and the calculation of the internal nodal forces, uniaxial stress tests were conducted and the results were compared with the analytical solution. Apart from that, the deformation of a half-ellipsoid due to the application of pressure on its inner surface was simulated using the static solver and the volume-pressure work was compared with the deformation energy. This allows to validate, if the nodal forces which correspond to the applied pressure are calculated correctly. Moreover, it validates that the deformation energy which is stored in the elastic deformed ellipsoid is equal to the volume-pressure work.

In order to validate the implementation of the Newmark-Beta solver, the

same settings were used. But this time, the pressure is switched to zero instantaneously after the ellipsoid has been inflated. This causes a rapid deflation of the ellipsoid. The sum of kinetic energy, deformation energy and energy dissipation due to the Rayleigh damping is compared with the volume-pressure work which was initially done by the pressure in the cavity. This validates that the total energy is conserved and no energy is created or lost due to numerical effects.

Moreover, at the time writing, Lukas Baron and I participate in a benchmark study initiated by Sander Land from the Biomedical Engineering Department of the King's College London. Objective of this study is to compare the results of different simulation frameworks for cardiac mechanics of the participating scientific groups based on a set of defined problems.

Convergence Analysis of Linear and Quadratic Tetrahedral Elements

A bar with the dimension $10 \text{ mm} \times 1 \text{ mm} \times 1 \text{ mm}$ was fixated at one of the small sides and a pressure of 10 Pa was applied to its bottom surface. The resulting deformation is calculated for different mesh resolutions (from 44 nodes to 46529 nodes) using T4 and T10 elements in combination with T3 and T6 surface elements for the pressure, respectively. The resolution is given in terms of nodes and not in terms of elements, since the numerical complexity is mainly determined by the number of nodes. To compare the results, the displacement in z -direction of the lower edge of the unfixated side of the bar is determined. The mechanical properties were described by the Guccione *et al.* model using the parameters given in Tab. 16.1

Table 16.1: Parameters used for the Guccione *et al.* for the convergence analysis

C [Pa]	b_1	b_2	b_3	K [Pa]
1200	26.7	2.0	14.7	$1e4$

In Fig. 16.2 a visualization of the bending simulation is presented. In Tab. 16.2 and Fig. 16.1 the displacement of the lower edge of the free end in z -direction is given for the different mesh resolutions for the T4 and

T10 elements. The T10 elements show a very good performance. Even for the bar with only 189 nodes the result is almost equal to the results of the mesh with the highest resolution consisting of 46529 nodes. If we assume, that the converged solution of the T10 elements is the *correct* result, then the relative error for the mesh consisting of 189 nodes is 0.6%. In contrast to that, the T4 elements showed a very poor convergence behaviour. Here, the relative error for the mesh with 189 is 40.1% while even for the mesh with 46529 nodes, the error is still 1.1%.

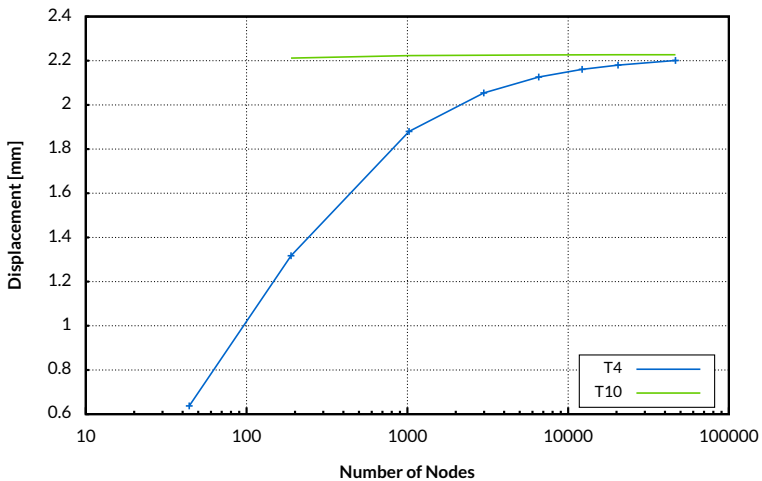


Figure 16.1: Convergence analysis: Results of a simulation of the bending of a bar due to an applied pressure for T4 and T10 elements with different mesh resolutions (in terms of nodes)

Uniaxial Stress Test

For the uniaxial stress test, the stretching and compression of a bar with the dimension $2 \text{ mm} \times 2 \text{ mm} \times 4 \text{ mm}$ was simulated. The geometrical

Table 16.2: Results of the convergence test for T4 and T10 elements. Given is the displacement of the lower edge of the free side of the bar in z-direction

Number of nodes	T4 [mm]	T10 [mm]
44	0.637	
189	1.317	2.212
1025	1.880	2.223
2989	2.054	
6561	2.126	2.226
12221	2.161	
20449	2.180	2.227
46529	2.201	2.227

model consisted of 96 tetrahedral elements (T10). The nodes of one of the small sides of the bar were defined to be fixated in the z-plane while on the opposite side, the displacement of the nodes in z-direction was controlled. The motion of the nodes in x and y direction was unconstrained. The total force of all nodes of the controlled side was calculated and divided by the current surface area in order to obtain the surface traction in direction of the displacement (normal direction of the surface). The traction from the simulation was compared with the analytical solution of the uniaxial stress test. The stress test was conducted using the Guccione *et al.* model with the same parameters as given in Tab. 16.1 but with a bulk modulus of $K = 10^{-7}$ Pa and the Mooney-Rivlin model (Eq. 5.20) with the settings given in Tab. 16.3.

Table 16.3: Parameters used for the Mooney-Rivlin material law for the uniaxial stress test

c_1 [Pa]	c_2 [Pa]	K [Pa]
1000	500	1e6

Analytical solution

The box is stretched (compressed) in x-direction. Since the material properties are incompressible and either isotropic (Mooney-Rivlin) or transverse isotropic with respect to the stretching (compressing) direction (Guccione),

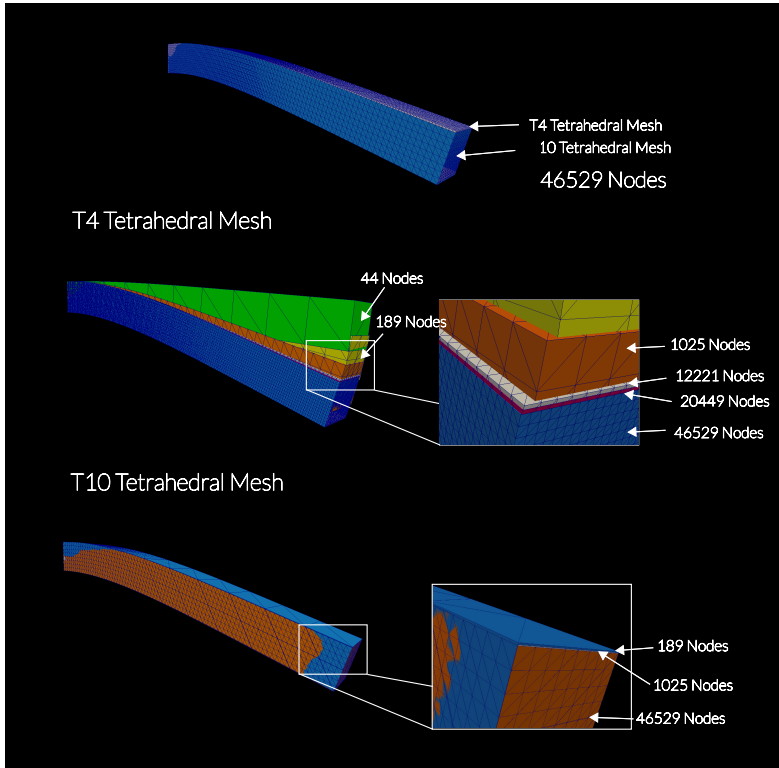


Figure 16.2: Linear tetrahedron versus quadratic tetrahedron: Displacement of the lower edge of the unfixed side of the bar for T4 and T10 elements for different mesh resolutions in terms of nodes

the deformation tensor is given by

$$\begin{pmatrix} \lambda & 0 & 0 \\ 0 & \frac{1}{\sqrt{\lambda}} & 0 \\ 0 & 0 & \frac{1}{\sqrt{\lambda}} \end{pmatrix} \quad (16.1)$$

where λ is the stretch ratio. The surface traction on the controlled surface in direction of the stretching consists of the component C_{11} of the Cauchy stress in x -direction and the hydrostatic pressure due to the incompressibil-

ity.

$$T(\lambda) = C_{11} + p \quad (16.2)$$

The material is either isotropic or transverse isotropic and incompressible. Since it is only the hydrostatic pressure which causes the lateral deformation of the box, the Cauchy stress components C_{22} and C_{33} must be equal to the negative of that pressure. Accordingly the surface traction is given by

$$T(\lambda) = C_{11} - C_{22} \quad (16.3)$$

The results of the uniaxial stress test are given in Fig. 16.3 and Fig. 16.4. The simulated and the analytical curves show an almost perfect match.

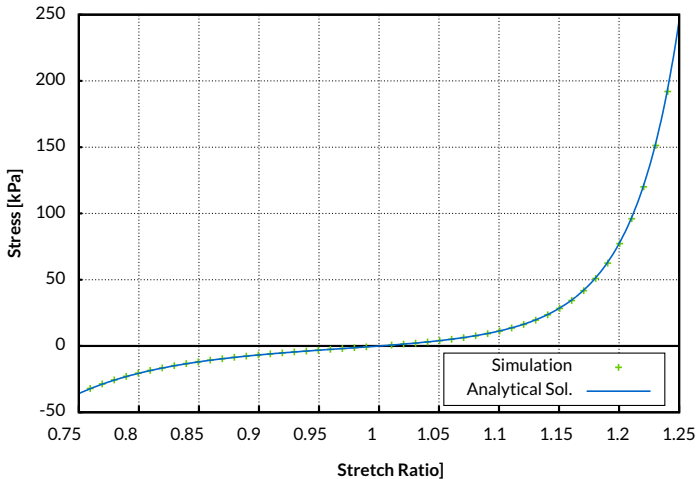


Figure 16.3: Uniaxial stress test with compression and stretching using the Guccione *et al.* material model. Comparison of simulation results and analytical solution

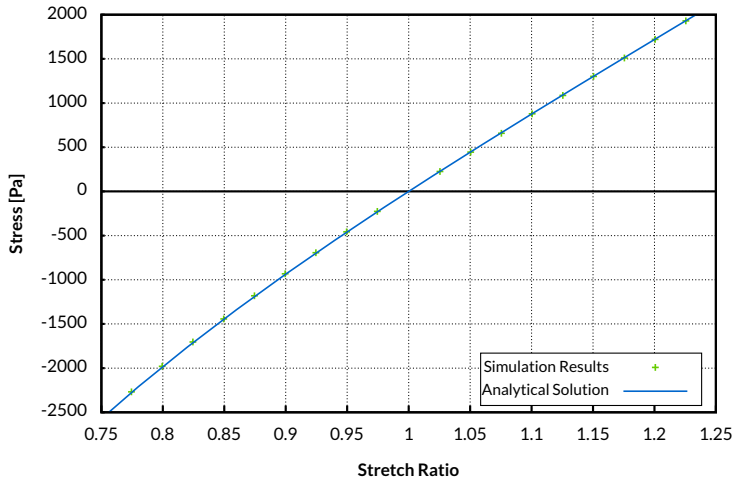


Figure 16.4: Uniaxial stress test with compression and stretching using the Mooney-Rivlin material model. Comparison of simulation results and analytical solution

Comparison of Volume-Pressure Work with Deformation Energy and Kinetic Energy

The geometrical model of the half-ellipsoid had a height of 7.1 mm, an outer radius of 2 mm and an inner radius of 1 mm and consisted of 47976 T10 elements. The nodes of the top surface were defined to be fixated. (Fig. 16.5). Pressure was applied to the surface of the cavity and increased continuously from 0 Pa to 0.350 Pa within 200 ms. The static solver was used to calculate the resulting deformation of the half-ellipsoid. The equivalent nodal forces of the nodes of the cavity surface due to the applied pressure were calculated using the T6 triangle elements. The volume-pressure work was calculated as follows:

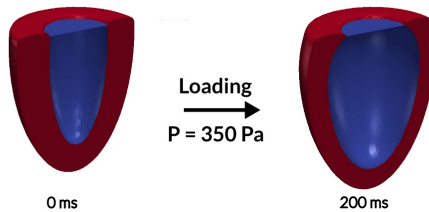
$$W = \sum_n P_n \cdot (V_n - V_{n-1}) \quad (16.4)$$

where V_n is the cavity volume and P_n is the pressure of simulation step n . The material properties of the half-ellipsoid were described by the Guccione *et al.* model using the following parameters given in Tab. 16.4.

Table 16.4: Parameters used for the Guccione *et al.* model for the simulation of the half-ellipsoid

C [Pa]	b ₁	b ₂	b ₃	K [Pa]
100	2	2	2	1e4

Static Solver



Dynamic Solver

Loading P = 350 then pressure is switched off after 200 ms

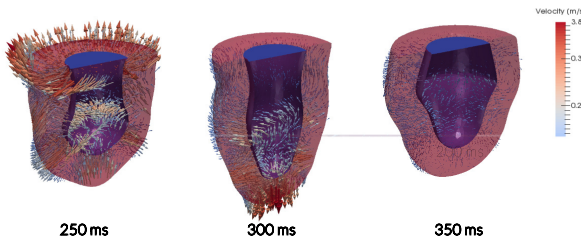


Figure 16.5: Deformation of a half-ellipsoid due to applied pressure, calculated with the static solver (top), Simulation of the same half-ellipsoid using the dynamic solver (bottom). First, the half-ellipsoid is inflated by applying pressure on its inner surface. Eventually, the pressure is set to zero, which results in a damped oscillations.

In Fig. 16.5, the unloaded and the loaded half-ellipsoid of the simulation

with the static solver is shown (top). The resulting volume-pressure work and the total deformation energy of the half-ellipsoid are given in Fig. 16.6. Both curves match almost perfectly to each other. For the next validation

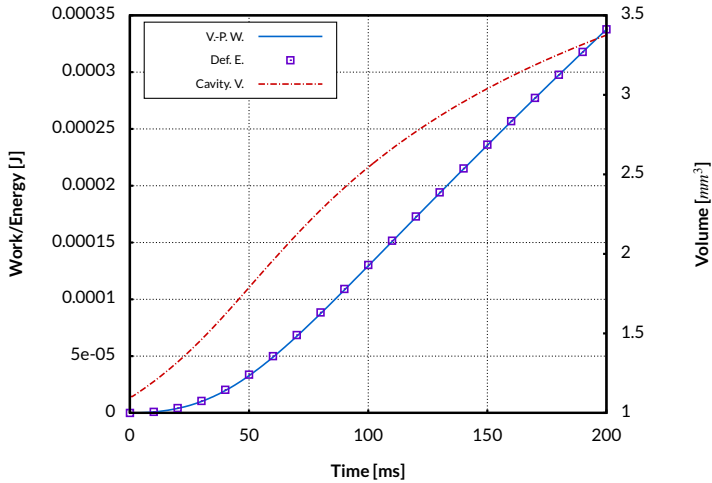


Figure 16.6: Simulation of the half-ellipsoid using the static solver. Time course of volume-pressure work (V-P.W.), stored deformation energy (Def.E.) and the volume of the cavity of the half-ellipsoid (Cavity.V.).

test, the same setting was used, but this time together with the dynamic solver based on Newmark-Beta time integration. The Newmark-Beta parameters were set to $\beta = 0.5$ and $\gamma = 0.25$ in order to obtain a numerically undamped solution. The pressure on the cavity was again increased step-wise from 0 Pa to 350 Pa for 200 ms. Eventually, after the pressure had reached its maximal value, the pressure was set to zero instantaneously. This caused a rapid oscillating motion of the half-ellipsoid which was damped due to the Rayleigh damping. Again volume-pressure work and deformation energy were determined. Additionally, the kinetic energy and the energy dissipation due to the Rayleigh damping were determined. A visualization of the deformation of the half-ellipsoid and the velocity

vector field for three different time steps after the pressure was switched off is given in Fig. 16.5 (bottom). In Fig. 16.7, the time courses of cavity volume, volume-pressure work, deformation energy, kinetic energy and the energy which dissipated due to the Rayleigh damping are given. During the first 200 ms, almost all volume-pressure work is stored as potential energy in the elements of the half-ellipsoid while the kinetic energy is almost zero. However, when the pressure is suddenly switched off, the volume-pressure work done remains constant and the half-ellipsoid begins to oscillate massively. The stored energy swaps between deformation energy and kinetic energy, while the energy slowly dissipates due to the Rayleigh damping. However, the total sum of kinetic energy, deformation energy and dissipated energy remains always constant and equal to the initially volume-pressure work done.

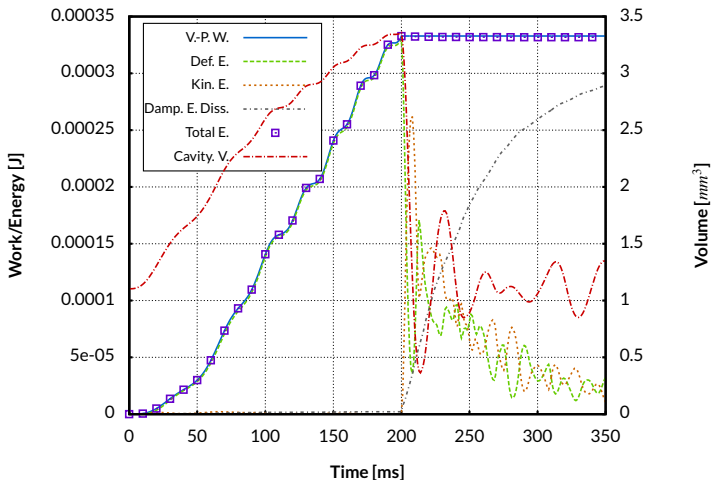


Figure 16.7: Simulation of the half-ellipsoid using the dynamic solver. Time course of volume-pressure work (V-P.W.), stored deformation energy (Def. E.), kinetic energy (Kin. E.), energy dissipated due to Rayleigh damping (Damp. E. Diss.), The total energy (Total. E. = Def. E. + Kin. E. + Damp. E. Diss.) and the volume of the cavity of the half-ellipsoid (Cavity.V),

16.2 Mechanical Benchmark

Three mechanical problems had been prepared by Sander Land for the benchmark study. The first problem was a bar which was bended by applying pressure to its bottom surface. The second problem was half-ellipsoid with homogeneous mechanical properties where pressure is applied to its cavity. The third problem was also a half-ellipsoid, but this time with anisotropic mechanical properties and a defined fiber orientation. Additionally to the pressure, the elements contracted actively along the fiber direction (Fig. 16.8). At the time of writing, the results of the study have not been published yet and therefore can unfortunately not be presented here. But it can already be stated, that our results match very well to the results of the other groups.

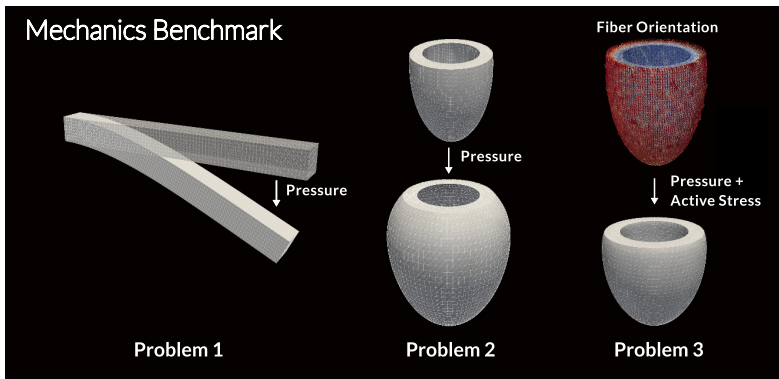


Figure 16.8: Three mechanical problems prepared by Sander Land of the group of Nick Smith (KCL) for the benchmark study

16.3 Discussion

The results of the convergence test show, that T4 and T10 elements converged to the same results. This is a strong hint, that both implementations are correct. Apart from that, the results demonstrate the superiority of

quadratic tetrahedral elements over linear tetrahedral elements for incompressible deformations. The simulated solutions for the uniaxial stress test match almost perfectly to the analytical solution for stretching and compression. While this is first of all a satisfying result, one should not forget that in this case, the box was only deformed along its principal axis. Therefore, it is still thinkable, that for a more complex problem like a bending test (for which it is not so easy or even impossible to calculate the analytical solution), the simulation framework might provide an incorrect result. The validation tests with the half-ellipsoids showed that the volume-pressure work done by the pressure on the cavity was equal to the deformation energy of the half-ellipsoid even for a strong deformation. If for example, the nodal forces were calculated incorrectly due to an incorrect implementation of the T10 or the T6 elements, there would be a high chance, that this would cause a discrepancy of deformation energy and volume-pressure work. The test with the dynamic solver shows, that the Newmark-Beta algorithm does a good job regarding the conservation of energy. These results and in particular the preliminary results of the mechanical benchmark make me confident, that the simulation framework in the current state delivers correct results.

Chapter 17

The Beating Heart within the Pericardium

Finite Element Analysis of a Contact Problem

In this project, the interplay of atria and ventricles and the function of the pericardium is analyzed. For this purpose, the contraction of the heart was simulated with and without contact handling heart and the pericardium and the results are compared to each other. To the best of my knowledge, this is the first presentation of a biomechanical simulation of the whole heart including the atria, the ventricles and the pericardium. This chapter is based on the publication (Fritz et al., 2013).

17.1 Introduction

Boundary conditions are one of the most important aspects for the biomechanical modeling of the heart. The movement of the heart underlies different constraints. The atria and ventricles are connected to vessels, which limit the motion of the heart. Moreover, the motion of the heart is constraint by the pericardium which surrounds the heart (see Sec. 2.1). During the contraction, the heart surface slides on the pericardium. At the same time, the pericardial pressure is decreased which causes that also the

pressure in the atria is lowered. This results in an increase of the pressure gradient from the veins to the atria (Holt, 1970). Tyberg et al. (1986) analyzed the relationship between pericardial pressure and right atrial pressure. He showed that the pericardial pressure is directly proportional and very similar to the right atrial pressure. Apart from the deformation of the heart, also the pericardium and the surrounding tissue are deformed, as it can be found in cine MR images. From this, we concluded that the pericardium in combination with the surrounding elastic tissue has a direct impact on the motion of the heart. Different experiments have revealed, that if the pericardium is removed, the diastolic and systolic function of the heart are altered (Watkins and LeWinter, 1993). Congenital absence of the pericardium is a rare cardiac defect which comes along with cardiac hypermobility (swinging "pendulum" movement of the heart), elongated atria and an abnormal deformation of the heart, often referred to as 'teardrop heart' due to the missing shaping forces of the pericardium. Apart from that, the heart often shows an abnormally large variation of its outer contour in contrast to the normal case, where the outer contour does almost not vary during the contraction (Mantovani et al., 2011; Psychidis-Papakyritsis et al., 2007; Topilsky et al., 2010).

Another aspect of the heart contraction is the atrioventricular plane displacement (AVPD). During the contraction, the atrioventricular plane moves downwards in direction of the apex. This causes an increase of the atrial volume and thereby, supports the filling of the atria. When the heart relaxes, the atrioventricular plane moves upwards again and the ventricles envelop the atrial blood volume. The AVPD is considered to be a major contributor to the ventricular pumping function (Carlsson et al., 2007). A reduced AVPD is strongly related to heart failure (Willenheimer et al., 1997). The interplay of ventricles, atria and the pericardium plays an important role for the cardiac contraction. However, it is usually ignored by the scientific community. Most computational models of the heart include either only the ventricles (Krishnamurthy et al., 2012; Marchesseau et al., 2013a; Kerckhoffs et al., 2007; Gurev et al., 2011) or only the atria (Di Martino et al., 2011a). A common method to apply boundary conditions is to restrict the movement of the atrioventricular plane (Krishnamurthy et al., 2012) and (Gurev et al., 2011). Some models include a simplified approach to con-

sider the impact of the pericardium, e.g. by defining a fixed surface which restricts the radial motion (Marchesseau et al., 2013a; Di Martino et al., 2011a) or by applying a pressure depending on the ventricular volume (Kerckhoffs et al., 2007).

It is necessary to improve the boundary conditions, in order to obtain a more realistic description of the motion of the heart, even if the focus lies only on the ventricles. It has to be considered how the ventricles and the atria influence each other and to take into account the interaction of the ventricles and the atria with the pericardium. Apart from that, it has to be analyzed, how physiologically motivated Dirichlet boundary conditions can be applied.

17.2 Methods

For the simulations, the parameters of the material law for the ventricles and atria were set according to the findings of Omens et al. (1993). They are given in Tab. 17.1. Each ventricle was coupled with a three-element Windkessel model Sec. 13. The parameter were taken from Stergiopoulos et al. (1999) and are given in Tab. 17.2. The geometrical model and the generation of the fiber orientation are described in Sec. 10. The electrophysiology and the active tension development were simulated using the acCELLerate framework as described in Sec. 11. Output was a normalized mechanical tension distribution for each time step. This was scaled with the parameter $T_{max} = 180\text{kPa}$ for the maximal tension. The value was adapted in such a way that the ejection fraction and blood pressure were within a normal range. Experimental data of the mechanical parameters of the pericardium are available (Freeman and Little, 1986; Lee and Boughner, 1985). However, the mesh which represented the pericardium and the surrounding tissue in our model does not contain a real volumetric representation of the pericardium itself. For that reason, this data is not directly applicable. In this project, the Guccione model was also used for the pericardium and the parameters were adapted manually, in order to obtain a deformation which matched the MRI data. The parameters were set $b_1 = b_2 = b_3 = 10$ to obtain isotropic properties. The mesh of pericardium is just a thin layer and the outer surface was fixed. Accordingly, it can hardly deform without

a change in volume and thus the deformability is strongly determined by the bulk modulus K . With a value of $K = 10^3 \text{Pa}$, the deformation of the heart matched qualitatively well to the MRI data. For the biomechanical simulation, the damping coefficients were set to $\alpha = 500 \frac{1}{\text{s}}$ and $\beta = 0.01 \text{ s}$ in order to get a realistic contraction velocity while avoiding unphysiological oscillations. The stop criterion for the Newton algorithm was set to 10^{-6} N . The time step size was adaptive and depended on the convergence of the Newton algorithm, while the maximal time step size was set to 1 ms.

Table 17.1: Parameters used for the Guccione material law for different tissue types

	C [Pa]	b_1	b_2	b_3	K [Pa]
Ventricles & Atria (based on Omens et al. (1993))	1200	26.7	2.0	14.7	$2 \cdot 10^5$
Pericardium	1200	10	10	10	10^3

Table 17.2: Parameters used for the Windkessel model

C	5.16 ml/mmHg
R_1	0.030 mmHg s/ml
R_2	0.63 mmHg s/ml
Initial aortic pressure	67.5 mmHg
Initial pulmonary artery pressure	15.0 mmHg

In the MRI data, the heart in diastolic state was not stress-free. For that reason, a stress-free configuration of the heart geometry had to be found. This has been conducted using as described in Sec. 13.3. The negative pressure, which was used to obtain the stress-free configuration was therefore adjusted in such a way, that in the left ventricle, the end-diastolic pressure was about 5 mmHg and in the right ventricle about 3 mmHg.

17.3 Simulation and Evaluation

In order to evaluate the effect of the pericardium, two simulation had been conducted, one with contact handling of pericardium and heart and one without contact handling. For both simulations, the same geometry containing the whole heart, the pericardium and the surrounding tissue was used. Without contact handling, the motion of the heart was completely independent from the pericardium and the surrounding tissue, accordingly this simulation is named *simulation without pericardium* and the other *simulation with pericardium* in the following. The results were evaluated by assessing and comparing the qualitative deformation of the heart during the contraction, intraventricular pressures, ventricular volumes, atrial volumes and AVPD. Moreover, two slices of the cine MRI data were compared qualitatively with the corresponding slices of the simulation results. To evaluate the contact handling algorithm, the average distance between master and slave surface during the contraction and the amount of Newton steps was analyzed. The AVPD in the simulation was measured as follows: Five triangles representing the atrioventricular plane of the left ventricle were defined and the average initial normal vector, which corresponded to the long axis was calculated. Then the average displacement of the centroids of the triangles in direction of that vector was determined. The result was compared to the measured AVPD obtained from the cine MRI for 22 time steps. Here, the AVPD was measured for each time step for two different cine MRI slices and averaged. The heart rate and dynamics of the simulation were not adapted to match the MRI data, hence a direct comparison was not possible. Therefore, the timing was adapted such as the beginning of the contraction and the end of the relaxation phase of left ventricle of the MRI data and simulation matched to each other. Eventually, the course of time and the maximal value of the AVPD of the MRI data and the simulations were compared.

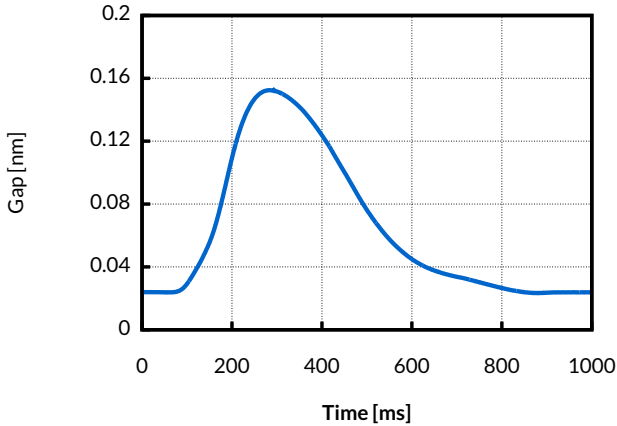


Figure 17.1: The average distance (gap) between master surface and slave surface over time

17.4 Results

The master elements slid smoothly on the slave surface in the simulation with pericardium. The penalty parameter was set to $\varepsilon = 5 \cdot 10^4$ kPa. The maximal average distance between the slave and master surface during the contraction was $d_{max} = 0.15$ mm (Fig. 17.1). The contact handling algorithm did a good job on remaining permanent contact during the heart cycle. The Newton method showed a good convergence. Here the average number of Newton steps was $n = 2$ the maximal number was max: $n = 7$ (no pericardium: 1.3, max: 3). Figures 17.2 and 17.3 show the deformation of the heart with and without pericardium at different time steps of the heart cycle. The contour of the outer surface of the heart in the simulation with pericardium varied only minimally during the contraction although, the ventricles as well as the atria were significantly deformed. The atrioventricular plane moved downwards towards the apex while the atria were stretched. The blood pressure and the ventricular volume curve were considerably affected by the interaction of heart and pericardium. The maximal blood pressure was reduced for both ventricles (left: from 115.6 mmHg

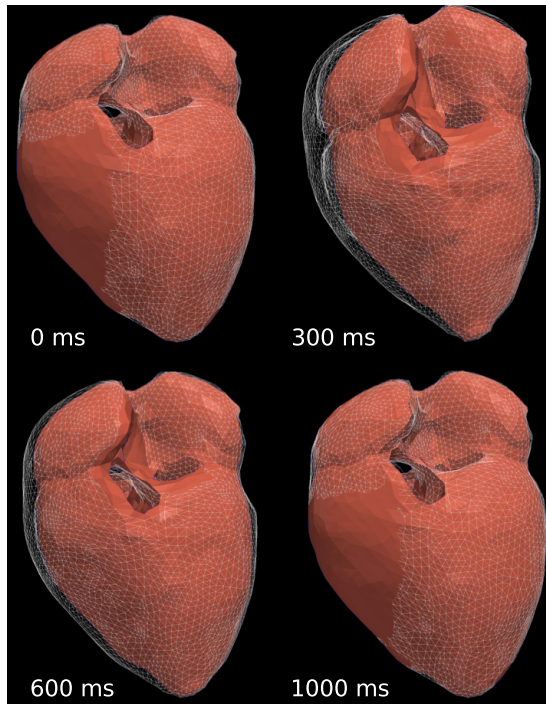


Figure 17.2: Visualization of the deformation of the heart with contact handling of pericardium and heart (white wireframe model) and without contact handling (red model) at different time steps

to 107.3 mmHg, right: from 39.4 mmHg to 29.1 mmHg) (Fig. 17.4), the stroke volume was reduced for both ventricles (left: 97.3 ml to 85.8 ml, right 59.8 ml to 37.5 ml) as well as the ejection fraction (left: from 70.9% to 63.4%, right: from 55.9% to 35.0%, Fig. 17.5) in the simulation with pericardium. For the simulation with pericardium, the time delay between maximal pressure of the right and left ventricle was 1 ms. In contrast to that, the delay was 8 ms for the simulation without pericardium (time resolution of the results: 1 ms). The time course of the blood pressure showed small oscillations for both ventricles when the valves had closed.

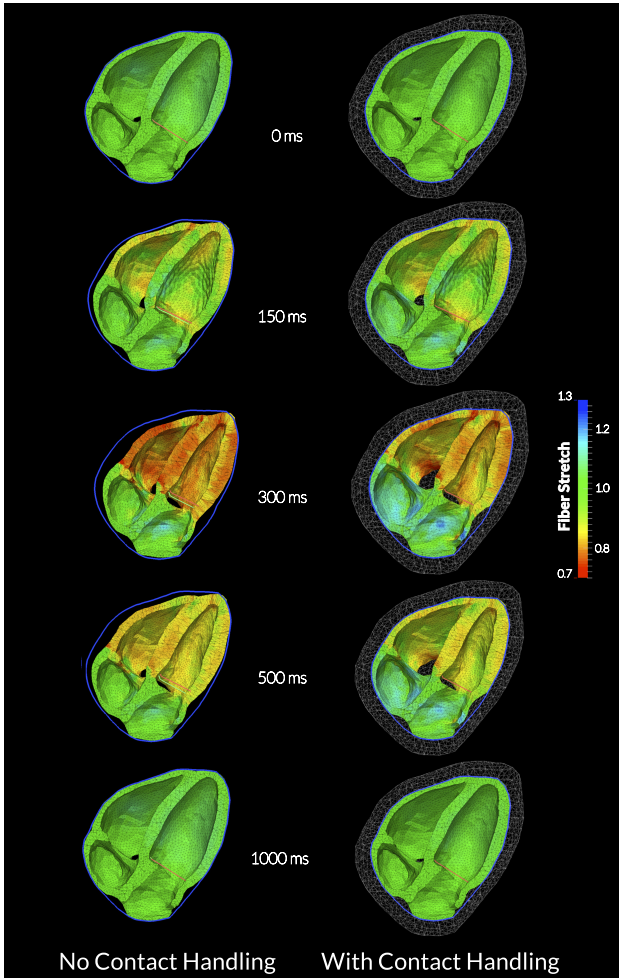


Figure 17.3: Simulation of the contraction with pericardium and contact handling (left) and simulation without pericardium (right). The blue contour represents the contact interface with contact handling of pericardium and myocardium. The same contour is also shown in the simulation without pericardium in order to visualize the differences between the two simulations. The red and green line represent the atrioventricular plane of the simulation with and without pericardium. The fiber stretch is color-coded.

To evaluate the impact of the pericardium on the atrial volume during the ventricular contraction, the percentage increase of the cavity volume from diastole to the maximal volume was measured. In the simulations with pericardium, the cavity volume of the right atrium (diastolic 77.5 ml) was increased by 46.3%. The cavity volume of the left atrium (diastolic: 55.1 ml) was increased by 30.6% (Fig. 17.6). The maximal AVPD was 1.04cm (Fig. 17.7). For the simulation without the pericardium, the outer contour of the heart was noticeably deformed, especially the right ventricle and the right atrium. Apart from that, the heart showed a slight sideways movement. The atria were still stretched, but the change of cavity volume was smaller compared to the simulation with pericardium. The relative change of the cavity volume of the right atrium was decreased by 3.8% and of the left atrium was increased by 8.1% (Fig. 17.6). The maximal AVPD was 0.63cm and therefore, distinctively smaller than in the simulation with pericardium. However, the maximal AVPD in both simulations was considerably smaller than the measured maximal AVPD of 1.70cm from the cine MRI data (Fig. 17.7.)

Two slices of the cine MRI data (4-chamber, left ventricle long axis), at diastole and maximal systole are shown in Fig. 17.8 and Fig. 17.9. Further, the corresponding slices from the simulation results are visualized in these figures. However, the slices from the cine MRI data and the diastolic MRI data, used for the generation of the geometrical models, were displaced relatively to each other. The patient had presumably moved a little bit between the two acquisitions. Therefore, the corresponding slices in the simulation data was adjusted manually, until they matched optimally to the MRI data. The blue contour represents the contact interface during the contraction in the simulation with pericardium. The same contour is shown in the simulation without pericardium in order to visualize the differences between the two simulations. The atrioventricular plane of the simulation with pericardium and without pericardium is represented by the red and green line, respectively. The deformation of the ventricles, the stretching of the atria, the wall thickening and the motion of the atrioventricular plane

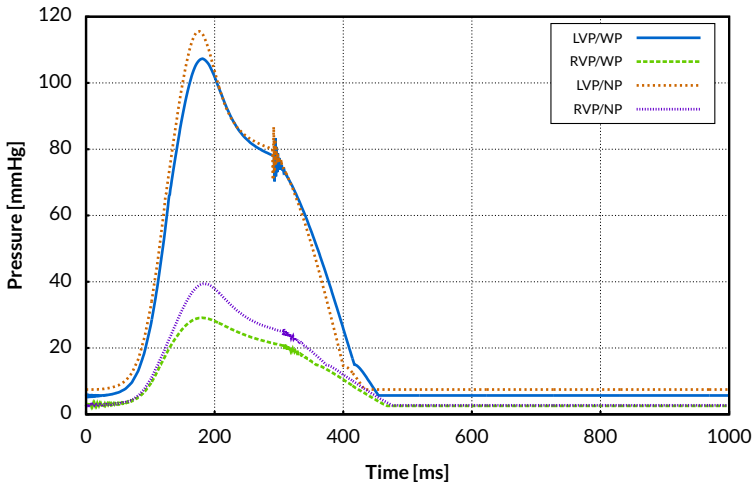


Figure 17.4: Pressure in left (LVP) and the right (RVP) ventricular cavity with pericardium (WP) and without pericardium (NP)

matched qualitatively to the MRI for both simulations. However, in the simulation with pericardium, the outer contour of the heart matched better to the MRI. Especially, the right atrium and the right ventricle showed here a better match than in the simulation without pericardium. Furthermore, the AVPD in the simulation with pericardium matched also better to the MRI.

17.5 Discussion

In the simulations, the pericardium reduced the maximal systolic pressure and the ejection fraction for both ventricles. In particular, the ejection fraction of the right ventricle was distinctively reduced. In all simulations, the ratio of left and right ventricular stroke volume was very unphysiological, since in reality both stroke volumes have to be equal due to the continuity

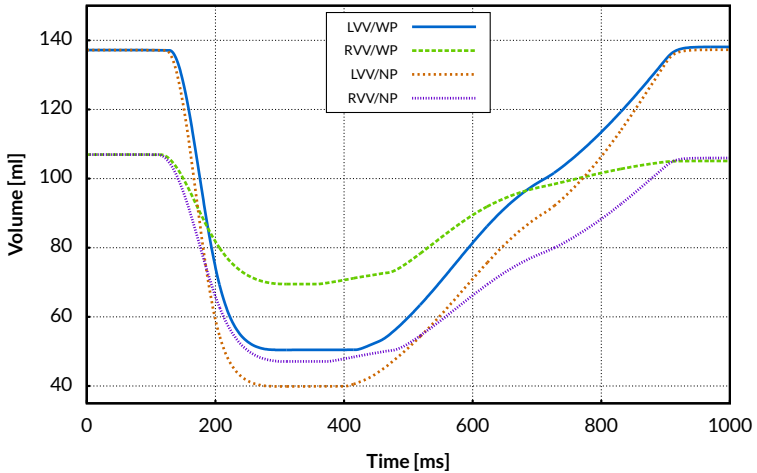


Figure 17.5: Left (LVV) and right ventricular volume time course (RVV) with pericardium (WP) and without pericardium (NP)

of flow. However, the right ventricular cavity was already smaller than the left cavity in the initial geometry which was generated from the MRI data. In reality actually, the opposite is usually the case (Sechtem et al., 1987; Alfakih et al., 2003). Some reasons therefore are: In both ventricles, the papillary muscles were not segmented, although these would reduce the volume of ventricles considerably, in particular that of the left ventricle. The right ventricle was difficult to segment in the MRI data. An overestimated wall thickness can also result in a wrong cavity volume. Apart from that, it was not so easy to define a closed surface for the right ventricle without adding additional points. The surface which we finally used did not enclose the complete right ventricular cavity.

Since the pericardium surrounds both ventricles, it is assumed that it promotes the interaction of both cavities and thus supports the synchronization of the contraction of both ventricles (Richardson et al., 2009; Nielsen et al., 1983, ch. 8, p.128). This synchronizing effect on the systole of the left and

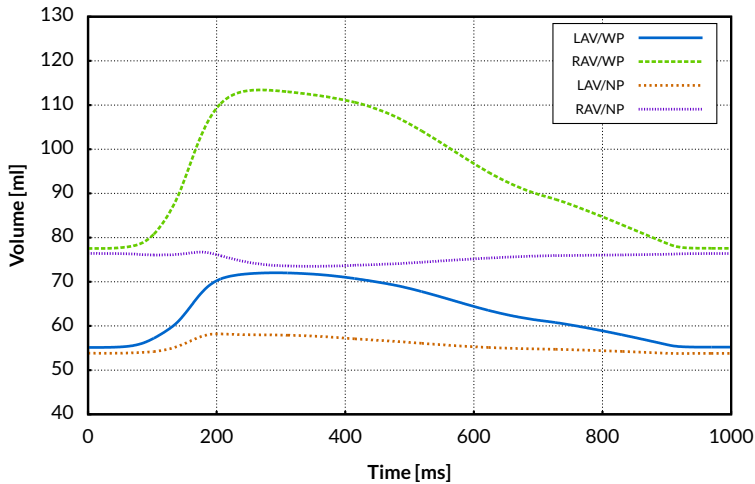


Figure 17.6: Left (LAV) and right atrial volume time course (RAV) with pericardium (WP) and without pericardium (NP)

right ventricle was also found in the simulation with pericardium. Different studies (Willenheimer et al., 1997; Carlsson et al., 2007) have shown that the AVPD is an important factor for the filling of the atria and also for the ventricular pumping function. Both simulations showed a distinct AVPD. However, in the simulation with pericardium, the heart surface slid on the inner surface of the pericardium with permanent contact. This supported the downward movement of the atrioventricular plane and resulted in a more pronounced AVPD. Due to the downward motion of the atrioventricular plane during the contraction, the atria were stretched and their volume increased. Afterwards, the atrioventricular plane moved upwards again during the relaxation phase. However, in both simulations, the AVPD was smaller than the value determined from the MRI data. This value matched well to the measurements of Carlsson et al. (16 ± 0 mm, range: 14 – 19 mm, control group N=12). We assume that this is caused by several factors. An improper parameterization of the material law of the atria can cause

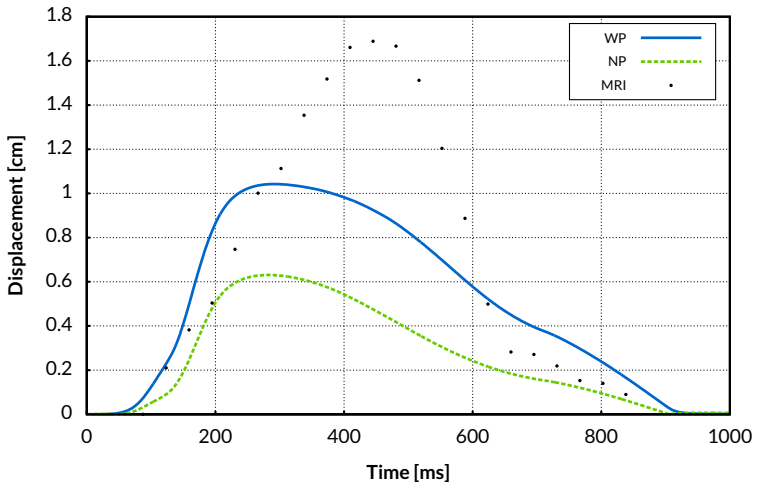


Figure 17.7: AVPD from simulation and measurement (MRI) each for the simulation with pericardium (WP) and without Pericardium (NP). The measured AVPD was determined manually from the MRI data for 22 time steps. Here, the timing was adapted in such a way that the beginning of the contraction and the end of the relaxation phase of left ventricle of the MRI data and simulation matched to each other

a too stiff behavior. The pressure in the atria was zero throughout the simulation. However, atrial pressure would also support the AVPD. The wall thickness was difficult to recognize and the atria were difficult to segment. An overestimated wall thickness might cause that, the atria could not be stretched sufficiently and thereby, the downward movement of the ventricles was impeded. The contraction of the ventricles depends strongly the fiber orientation. The used rule-based fiber orientation may not allow an optimal contraction. A further point, which should not be neglected, is that the model does not consider the momentum of the blood. However, this might also contribute to the AVPD. The Guccione *et al.* model was used for the simulations. This model is transversal isotropic and hence does not consider the sheet orientation. However it is assumed that the sheet orientation is a very relevant factor for the wall thickening and thus

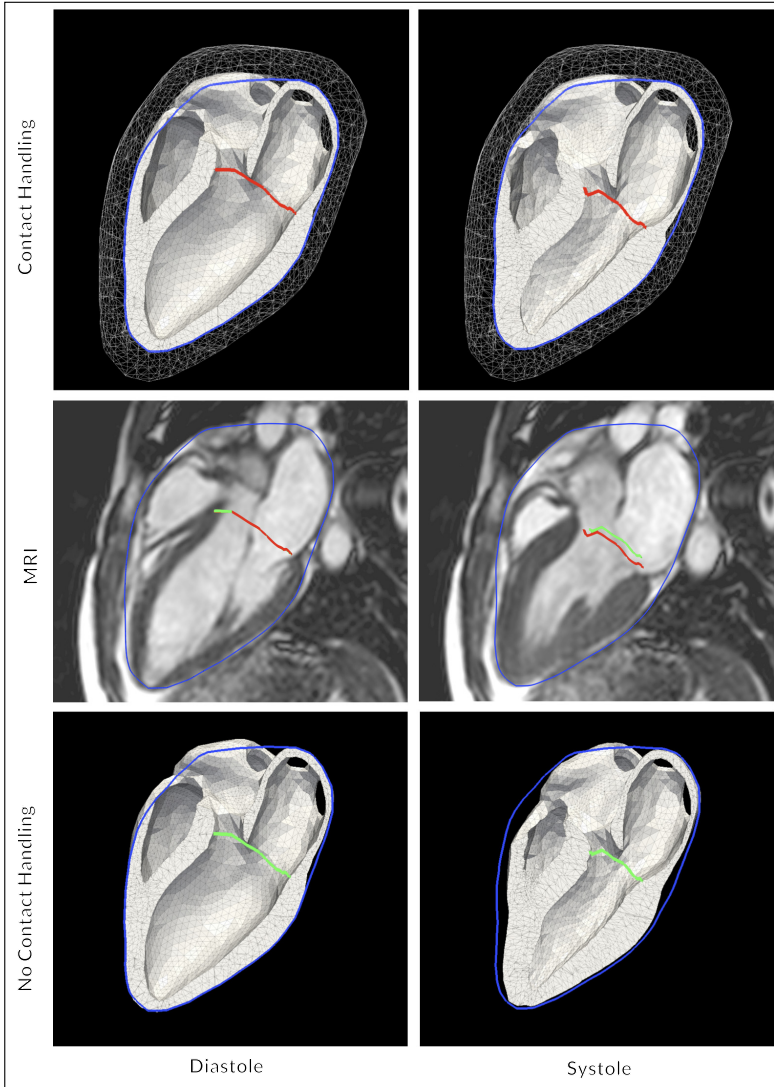


Figure 17.8: Comparison of cine MRI data with the simulation with pericardium (top) and without pericardium (bottom). The blue contour represents the contact interface in the simulation with pericardium. The same contour is also shown in the results of the simulation without pericardium in order to visualize the differences between the two simulations. The green and the red line represent the atrioventricular plane.

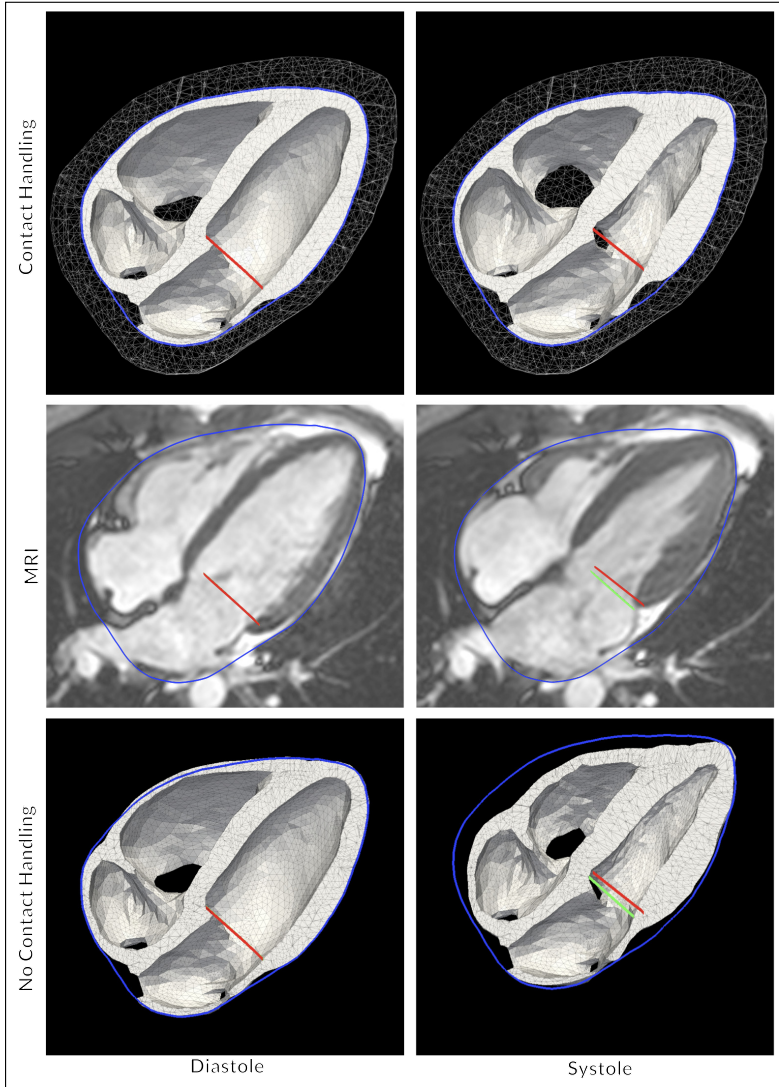


Figure 17.9: Comparison of cine MRI data with the simulation with pericardium (top) and without pericardium (bottom). See Fig. 17.8. The right atrium appears to have no contact to the pericardium. This is not the case. The atria lie underneath the pericardium, but due to the wireframe visualization, they are still visible

for the heart function (LeGrice et al., 1995).

The pericardium had a strong impact on the atrial cavity volume. The atria were stretched during the ventricular contraction, but due to the enforced contact to the pericardium their cavity volume increased. The same behavior can be observed in the cine MRI data. It is assumed that this mechanism causes a reduction of the atrial pressure and thus supports the influx of blood from the pulmonary veins and venae cavae into the atria (Holt, 1970). Sato et al. (2012) published measurement data of the left and right atrial volume index (volume per body surface area [ml/m^2]). They obtained for the right atrium (control group $N=21$) an average maximal volume index (V_{max}) of $40\text{ml}/\text{m}^2$ and an average reservoir volume index (V_{res} : Difference between the atrial maximum volume and the smallest atrial volume in mid-diastole) of $13\text{ml}/\text{m}^2$ for the left atrium and $V_{max} = 35\text{ml}/\text{m}^2$ and $V_{res} = 12\text{ml}/\text{m}^2$ for the right atrium. This corresponds to an average increase from the diastolic volume ($V_{max} - V_{res}$) to V_{max} of 48% for the right atrium and of 52% for the left atrium. While their findings for the right atrium matches well to the result of the simulation with pericardium, the increase in volume which we observed for the left atrium was distinctively smaller. The simulation without pericardium did not reproduce a realistic atrial volume change. But here, it has also to be considered that the used model did not include the central venous and atrial blood pressure.

In reality, the outer contour of the heart varies only minimally during the ventricular contraction (Emilsson et al., 2001). In the simulation without pericardium, the heart showed a noticeable radial contraction, in particular of the right ventricle. The outer contour was significantly deformed during the cardiac cycle. In the simulation with pericardium, the contour of the heart was only slightly deformed during the contraction and the whole deformation of the heart appeared to be more equable and smoother compared to the simulation without pericardium. These results match well to the echocardiography findings for patients with congenital absence of the pericardium (Mantovani et al., 2011; Psychidis-Papakyritsis et al., 2007; Topilsky et al., 2010). The *tear-drop* shape of the heart is clearly visible in the simulation without pericardium. It would be interesting to compare the simulation results with the echocardiogram

of a patient with congenital absence of the pericardium. However, in this context, the boundary conditions have to be reconsidered. While in our simulation the apex was defined to be fixated, the apex of a heart with congenital absence of the pericardium shows a significant movement (Psychidis-Papakyritsis et al., 2007).

This electromechanical model of the human heart, based on the biomechanical framework which has been developed in context of its work, is to the best of my knowledge the first one which takes into account the interaction of the ventricles with the atria and moreover the interaction with the pericardium and the surrounding elastic tissue in which the heart is embedded. Most of the present biomechanical models of the heart include only the ventricles and ignore the interplay with the atria. A common method to apply boundary conditions, is to constraint the motion of the atrioventricular plane. In 2012, Krishnamurthy et al. from the group of Andrew McCulloch and Jeffrey Omens presented an approach to create patient-specific models of the ventricular biomechanics of failing hearts. Their geometrical model included only the ventricles and the base was prevented from displacement and rotation along the long axis. Gurev et al. from the lab of Natalia Trayanova had presented a methodology to create electromechanical models with a ventricular geometry based on MRI and DTMRI data. Here, the motion of the heart was restricted by fixing some nodes near the orifice of the pulmonary artery and additionally restricting the motion of the posterior wall surface as well as the atrioventricular plane. This approach inhibits any AVPD and results therefore in an unphysiological motion of the heart. While one might argue, that only the relative motion of base and apex is relevant, it certainly makes a difference for the heart mechanics whether to stretch the atria or to lift the apex. Marchesseau et al. (2013a) from the group of Nicolas Ayache presented an electromechanical model of the left and right ventricle which they used for fast parameter calibration. The mesh of the ventricles was attached at the level of the four valves. The valves were connected by linear springs to their reference position. This allowed for some movement of the atrioventricular plane. This could be a good emulation of the atria if the springs are parametrized well, but nevertheless it can be assumed that a geometrical representation of the atria is able to reproduce

the mechanical behavior of the atria and its impact on the motion of the ventricles in a more realistic way. Different methods for considering the pericardium have been presented. Kerckhoffs et al. (2007) modeled the influence of the pericardium by an external pressure depending on the volume encompassed by the pericardium. This pressure was added to the atrial cavity pressure of the circulatory model and thus also considered an atrioventricular interaction. Marchesseau et al. modeled the pericardium by using a fixed surface surrounding the ventricles in combination with a collision detection algorithm, which limited the ventricular displacements by applying a force to those epicardium vertices which got too close to the pericardial surface. However, this does not prevent inward radial motion. In the work of Di Martino et al. (2011a), a computational model of a left porcine atrium is presented. Here a simplified fixed rigid model of the pericardium is used to constrain the motion of the atria. In contrast to these approaches, the contact handling algorithm which has been used in this project ensures frictionless and permanent contact. Moreover, it also considers the deformation of the pericardium and the surrounding tissue.

17.6 Limitations

The geometrical model of the heart did not contain the aorta and pulmonary arteries. Including them would have probably a considerable influence on the heart contraction. The electrophysiology, excitation propagation and tension development were computed in the reference configuration in advance and only for the ventricles, thus no feedback from the mechanics on the electrophysiology was considered. Apart from that, the model did not consider sheet orientation. The same parameter set was used for the Windkessel model of the pulmonary and systemic circulation and the atria were not linked to a circulatory system model. The parameterization of the material model used for the pericardium mesh was not based on experimental data. While experimental data of the pericardium is available (Freeman and Little, 1986; Lee and Boughner, 1985), it can not be directly applied to the model, since the model does not contain a volumetric representation of the pericardium. The unloaded state of the pericardium was taken from the end-diastolic MRI data. While in reality, the pericardium is under stress in

the enddiastolic state, this was not considered for this project.

17.7 Future work

A sensitivity analysis will be the next step with the objective to analyze how the mechanical properties of the pericardium mesh as well as preloading the pericardium affect the contraction of the heart. It will be necessary to validate the contact pressure with experimental data. The AVPD in the simulations was smaller than the measured one and therefore not yet satisfying. It has to be determined how this can be improved. Furthermore, it has to be evaluated how the elastic properties and the fiber orientation of the atria as well as the mechanical properties and the fiber orientation of the ventricles influence the AVPD. In particular, the incorporation of a realistic sheet orientation in combination with a suitable anisotropic material model e.g. the model presented by Costa et al. (1996) will presumably improve the simulation results. In the presented model, the same mechanical properties were used for the atria and for the ventricles. However, a better modeling of the atrial material properties will certainly provide better results. Bellini et al. (2012) presented a detailed mechanical analysis of the human atria. In a future work, their findings should be used for the atrial mechanics.

Chapter 18

Biomechanical Modeling of the Human Atria

Analysis of the Impact of Atrial Ablation Patterns on the Cardiac Pumping Performance

18.1 Introduction

Atrial Fibrillation

In the European Union (Fuster et al., 2006), approximately 4.5 million patients suffer from atrial fibrillation (AF). AF can often be treated pharmacologically, but more and more often, catheter ablation is the treatment of choice. However, the success rate of catheter ablation is not yet completely satisfying. Often the procedure has to be repeated several times until the AF finally terminates and often large areas of the atrial myocardial tissue are destroyed and replaced by scar tissue. This may come along with an impairment of the atrial mechanical function. Thomas et al. (2000) evaluated the effect of radio frequency ablation (RFA) on the atrial biomechanical function. They came to the conclusion, that multiple linear radiofrequency lesion may impair the atrial contractility due to the loss of myocardial tissue in the atria as well as the altered electrical activation of the atria. We

assume that in addition to that, ablation scar in the atria may also affect the ventricular systole. When the ventricles contract, the atrioventricular plane moves towards the apex, the atria are stretched and the cavity volume is increased. This mechanism supports the filling of the atria with blood from the venae cavae and the pulmonary veins. Eventually, this blood is available for the ventricular filling when the heart relaxes. If now, the mechanical behavior of the atria is altered due to the stiffer ablation lesion, this will also impede the atrioventricular plane displacement (AVPD).

Accordingly, two effects may have a negative impact of ablation scars on the ventricular filling: First, a reduced filling capacity of the atrium during the ventricular systole and hence less blood available for the filling of the ventricles. Second, a reduced active contribution of the atrium due to altered mechanical properties and an altered activation due to the ablation scars. Different ablation strategies with the aim to prevent AF exist but their respective impact on the heart function has not been completely understood. In this context, cardiac electromechanical modeling can be a tool which allows for a better understanding of how RFA can affect the mechanical behavior and the pumping function of the heart.

In this project, an electromechanical model was used to analyze different ablation scar patterns in the left atrium regarding their impact on the heart pumping function. In this context, the impact of the ablation scar patterns on the atrial contraction due to an altered activation and an increased stiffness of the ablated tissue was evaluated. Moreover, it was analyzed how the increased stiffness of the atria affects the AVPD, the ventricular ejection fraction and the volume increase of the atria during the ventricular systole. Five commonly used ablation patterns and one setting without ablation scar as control case were simulated. For each setting, the ventricular and atrial contraction was simulated separately. To evaluate how the stiffness of the ablation scar affects the deformation of the heart, three simulation settings with different stiffness parameters were defined for each ablation pattern.

This work has been conducted in a cooperation with Martin Krueger, Lisa Mareike Busch and Jan Richter. The latter two, were students who worked on this project in context of their bachelor and diploma thesis, respectively. They had been supervised by Martin and me. Some preliminary results

of an early state of this project were presented by Lisa Mareike Busch on the conference *Dreiländertagung der Deutschen, Schweizerischen und Österreichischen Gesellschaft für Biomedizinische Technik, Graz 2013* (Busch et al., 2013).

Biomechanical Modeling of the Atria

While in the past, most attention had been paid to the ventricles, modeling of the atria has moved into focus the recent years. However, most studies deal with atrial electrophysiology and there are only a few addressing atrial mechanics (Dössel et al., 2012).

Jernigan et al. (2007) published a study on the mechanical properties of porcine left atrium, which were assessed using uniaxial tests. In 2011, Di Martino et al. (2011a) presented a computational model of the porcine left atrium, which he used to analyze the wall stress due to the mitral valve movement, obtained from raw MDCT data. He modeled the mechanical properties of the atria based on biaxial tests with porcine atrial tissue. In a further study, he evaluated how ventricular tachypacing affects the spatial and temporal stress distribution of the left atrial wall (Di Martino et al., 2011b). Bellini et al. (2012) provided a comprehensive characterization of the passive biomechanics of the left human atria based on a Fung-type elastic strain energy potential. While the presented models deal with the passive mechanical properties, no model of the active contraction of the atria has been presented yet, as far as we know. A reason therefore, may be the fact that the atrial contribution to the function of the heart is often underestimated. Alhogbani et al. (2013) assessed the contribution of the left atrium to the filling of the left ventricle using cardiac magnetic resonance imaging (MRI) for 120 normal subjects. His findings show that the contribution of the atria to the ventricular filling increase with age and is in the range 10% – 40%. Considering that primarily elderly people have AF (70% of the patients are between 65 and 85 years old) (Fuster et al., 2011), the implications of RFA on the atrial contraction should not be disregarded.

18.2 Methods

The geometrical model and the generation of the fiber orientation are described in Sec. 10. The electrophysiology and the active tension development were simulated using the acCELLerate framework as described in Sec. 11. For the modeling on cellular level, the ten Tusscher model was used for the ventricles, while the heterogeneous Courtemanche model was used for the atria (Sec. 3.3). The contraction of the atria and the ventricles were simulated in the whole heart model including the pericardium. The Mooney-Rivlin model was used to describe the material properties of the atria and the Guccione *et al.* model was used for the ventricles. The parameters for the ventricles were set according the findings of Omens *et al.* (1993), while for the atria the parameters presented in (Di Martino *et al.*, 2011a) were used. All the parameters are given in Tab. 18.2. The ventricles and the atria were both coupled with Windkessel models as described in Sec. 13. For the ventricles, the parameter were taken from Stergiopoulos *et al.* (1999). The atrial Windkessel model was parametrized in such a way, that with an initial left atrial pressure of 10 mmHg, the maximal pressure was about 15 mmHg for the control case. All parameters are given in Tab. 18.1. For the atrial contraction, the valves between atria and ventricles were defined to be open.

In Fig. 18.1 an overview of the simulation workflow is given.

Active tension development of the atria

No active tension model was available for the atria. Therefore, the existing hybrid tension development model (HTD) (Sec. 11) was adjusted by Martin Krueger and Jan Richter (see also (Krueger, 2012, sec. 5.3, p.93-98), (Richter, 2012)) to reproduce the atrial tension development. In a first step, they identified 16 parameters from the original HTD model, which have a significant influence on the shape and duration of the simulated tension curve. In a next step, these parameters were optimized using the Powell algorithm (Sachse *et al.*, 2003b) such that the HTD model reproduced experimental data from atrial force development (Schotten *et al.*, 2002).

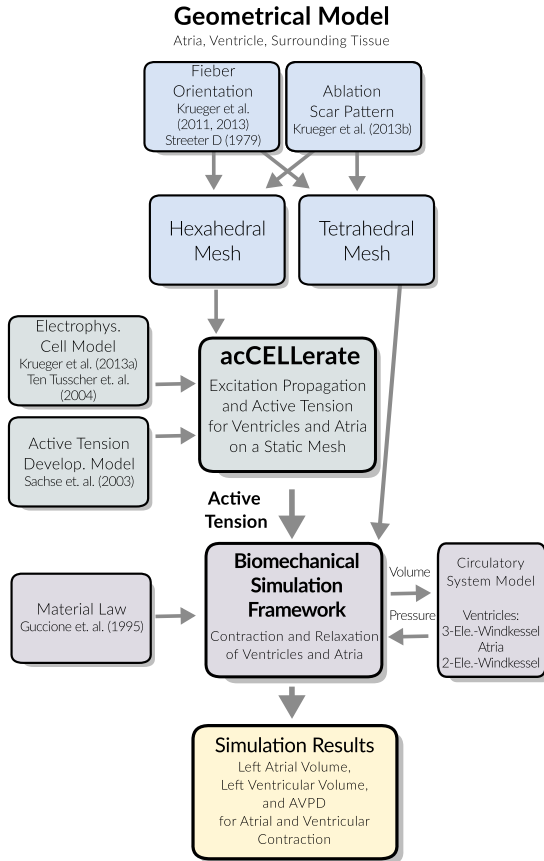


Figure 18.1: Schematic description of the simulation workflow. Whole heart MRI data is used as input to generate the geometrical models: A hexahedral mesh for the electrophysiological modeling and a tetrahedral mesh for the biomechanical modeling. These are used in the electromechanical simulation framework to calculate the electrical activation of the heart, the active tension development and the resulting mechanical deformation.

Modeling of Ablation Scars

Five patterns of RFA (see Fig. 18.2) were introduced into the left atrial model using the rule-based approach described in (Krueger et al., 2013).

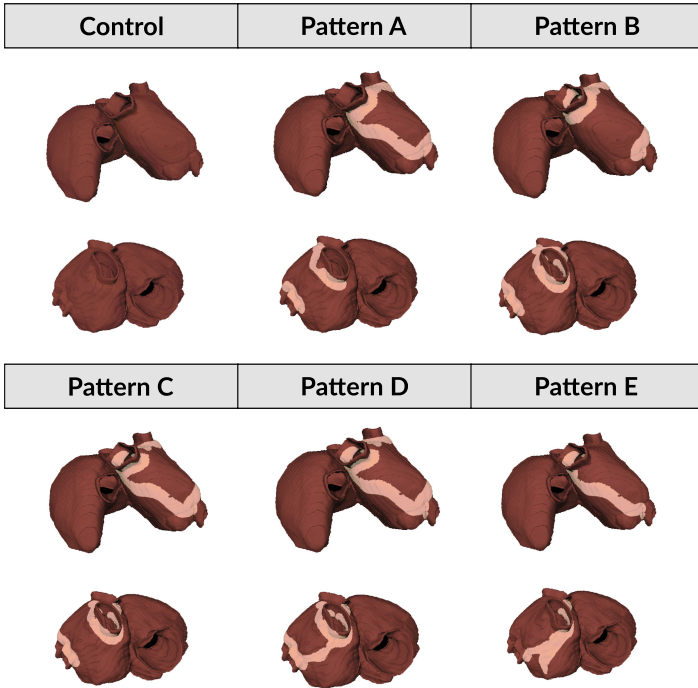


Figure 18.2: Five different ablation patterns on the left atrium. A: two partial lesions around the pulmonary veins, one linear lesion on the superior side of the left atrium. B: 4 circular lesions around each pulmonary vein. C: Like pattern B plus a lesion on the superior side of the left atrium. D: Like pattern C plus a linear lesion on the posterior side of the left atrium. E: One lesion around all pulmonary veins isolating the whole upper part of the left atrium plus a linear lesion towards the atrioventricular plane on the posterior side of the left atrium.

Table 18.1: Parameters used for the Windkessel models.

Ventricles	
C	5.16 ml/mmHg
R ₁	0.030 mmHg s/ml
R ₂	0.63 mmHg s/ml
Initial aortic pressure	67.5 mmHg
Initial pulmonary artery pressure	15.0 mmHg
Atria	
C _a	4 ml/mmHg
R ₁	0.016 mmHg s/ml
R ₂	0 mmHg s/ml
Initial left atrial pressure	10 mmHg
Initial right atrial pressure	5 mmHg

The patterns were named *A* to *E* and were selected to cover a wide range of commonly used ablation patterns. Pattern *A* is a set of three linear ablation lesions along the pulmonary veins and along the left atrial roof and was proposed by (Earley and Schilling, 2006). Pattern *B* reflects an individual circumferential pulmonary vein isolation (Marine et al., 2005). Pattern *C* was like pattern *B* plus a linear lesion along the roof of the left atrium. Pattern *D* was like pattern *C* plus a linear lesion on the inferior posterior side of the left atrium. It was similar to the pattern used in (Pappone et al., 1999). Pattern *E* consisted of a single circumferential lesion around all pulmonary veins isolating the complete area between the four pulmonary veins and an additional mitral isthmus line (Benussi et al., 2000). In the affected elements of the heart geometry used for the electrophysiological simulations, the tissue conductivity was set to zero and the cells were defined to be inexcitable. Consequently, no active tension was generated in these elements. For the biomechanical modeling, the stiffness value c_1 of the Mooney-Rivlin model was changed according to Tab. 18.2 for the different simulation settings.

Simulation setups and initialization

Setups

The electrical activation and tension development were simulated using *acCELLerate* for the five ablation patterns and the control case. The

Table 18.2: Parameters used for the Guccione and Mooney-Rivlin model for different tissue types and different simulation setting.

	C	b ₁	b ₂	b ₃	K
	[kPa]				[kPa]
Ventricles	1.2	26.7	2.0	14.7	$2 \cdot 10^3$

	c ₁	c ₂		K
	[kPa]			[kPa]
Atria	7.45	0	–	$2 \cdot 10^3$
Abl. scar [1x]	7.45	–	–	$2 \cdot 10^3$
Abl. scar [4x]	29.8	–	–	$2 \cdot 10^3$
Abl. scar [8x]	59.6	–	–	$2 \cdot 10^3$
Surrounding tissue	1	0	–	10

ventricular activation and tension development was simulated once. The resulting tension development data was interpolated to elements of the geometrical model used for the biomechanical simulations. The atrial contraction in the simulation with ablation pattern is affected by two aspects: The altered activation and the altered mechanical properties of the ablation scar. To assess the respective impact on the atrial contraction, three simulations were conducted for each ablation pattern, one with an unaltered stiffness, one with $4\times$ and one with $8\times$ increased stiffness of the ablation scar tissue (see Tab. 18.2). In total, 16 simulations of the atrial contraction were conducted: 15 with ablation patterns and one for the control case. The ventricular contraction is affected only by the altered mechanical properties of the ablation scar. For each ablation pattern, two simulations of the ventricular contraction were conducted, one with a $4\times$ and one with an $8\times$ increased stiffness of ablation scar tissue. Apart from that one simulation for the control case was conducted.

Initialization

In the MRI data, the atria and the ventricles were not stress-free in diastolic state. Therefore, the stress-free configuration had to be found as described in Sec. 13.3. The initial pressure in the atria was about 5 mmHg in the right atrium and 10 mmHg in the left atrium. To avoid a deflation of the atria at

the beginning of the simulation, first a negative pressure was applied to the atria which caused a shrinking. The deformed atria were used as the reference geometry. The negative pressure was adapted in such a way, that the volume of the atria after applying the initial pressure was approximately equal to that of the original geometry. The altered mechanical properties of the ablation scar would cause, that the initial stress-free configuration of the different models were not identical. To obtain the same stress-free configuration for all ablation patterns, the material properties of the ablation scars were defined to be transiently the same as of the healthy atrial tissue during the initialization phase.

18.3 Results

Model of Atrial Tension Development

The result of the parameter optimization which was conducted in order to adapt the HTD model to the data of Schotten et al. (2002) is shown in Fig. 18.3. The time course of the active tension obtained from the adapted tension development model matched well to the measured atrial tension developments. The adapted parameter set is given in Tab. 18.3. The activation time maps of the tension development for all the different ablation patterns are shown in Fig. 18.4. The tension development starts about 60ms after the electrical activation in the sinus node and propagates from the right atrium to the left atrium.

In the control case, the activation propagates from the superior side over the ridge between the orifices downwards the posterior side. The linear lesions in Pattern A changed the propagation path: Here, first the superior side was activated but then the activation propagated upwards the posterior side. Eventually, it reached the lateral ridge between the orifices of the pulmonary veins of the left atrium. The lesions did not isolate the region of the pulmonary veins completely. This caused a partial activation in that region.

The circular lesions of pattern B around the pulmonary veins had almost no effect on the propagation path. As expected, the isolated pulmonary veins were not activated. Pattern C resulted in an almost identical activation as

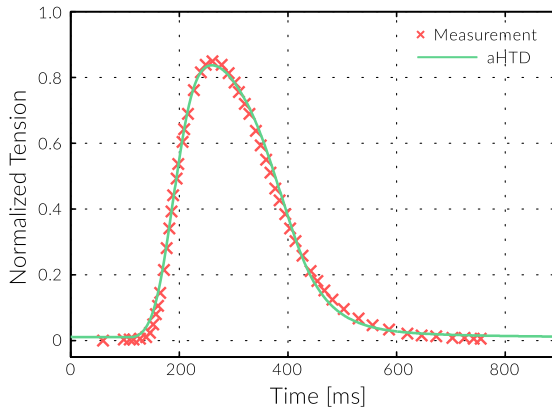


Figure 18.3: Comparison of normalized tension simulated the adapted Hybrid model and the measurement of Schotten et al. (2002). $RMSE = 1.68 \cdot 10^{-2}$.

that of pattern A. The only difference was, that the pulmonary veins in pattern C were not activated due to the complete isolation. In pattern D and E, the two linear lesions caused a complete isolation of the lateral ridge between the orifices. Their activation time maps were very similar.

Simulations of Atrial Contraction

The left atrial volume and pressure for all ablation patterns with an unaltered stiffness of the ablation scar are shown in Fig. 18.5.

The altered activation resulted in significant differences of the change in volume and of the atrial pressure. Measures of the results are given in Tab. 18.4. Pattern D and E with the two linear lesions showed the biggest reduction of contractility of the left atrium in comparison to the other patterns.

In the control case, the left atrial cavity volume was reduced by 31.0% during the atrial contraction. For pattern D and E, the volume change was reduced to 16.2% and 15.0%, respectively. Also, the maximal pressure of

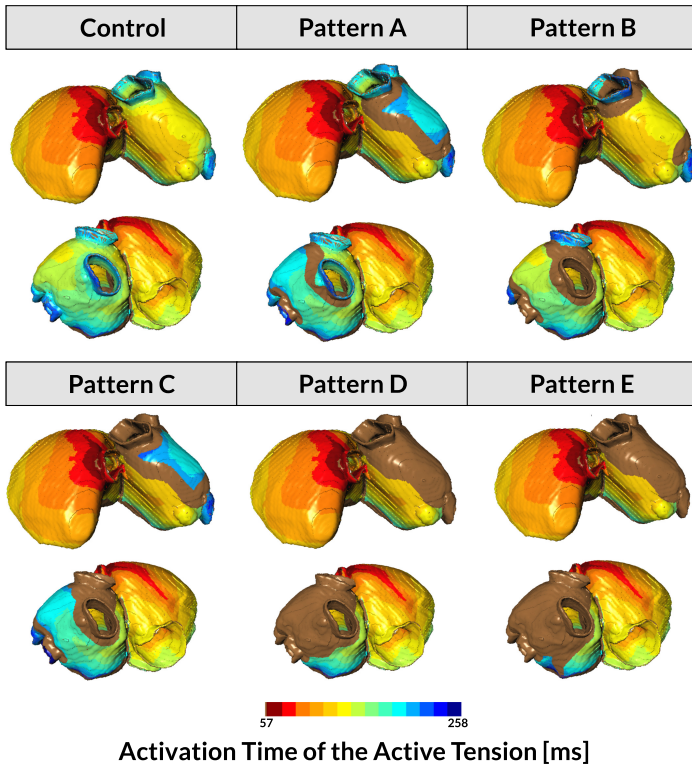


Figure 18.4: Visualization of the beginning of local atrial tension development (activation time) for the different ablation patterns. Brown: no activation at all.

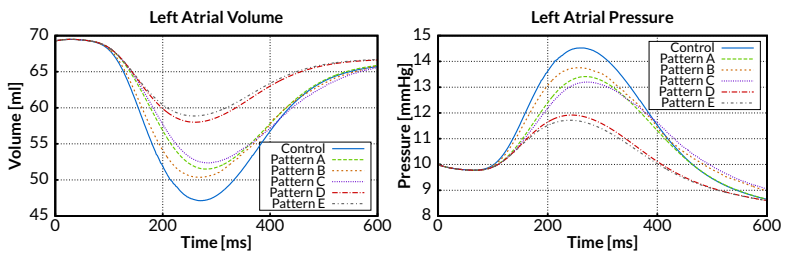


Figure 18.5: Atrial volume and pressure curves for different ablation patterns during the atrial contraction with an unaltered stiffness of the ablation scar.

Table 18.3: Parameter set of the ventricular hybrid tension development model (HTD) and the adapted atrial model (aHTD).

Parameter	HTD	aHTD
k_{on}	40	26.6
k_{off}	40	55.1
tm_{on}	12	28.9
tm_{off}	35	56.9
$TMon_{coop}$	2	5.31
$TMon_{pow}$	4	1.66
k_5	25	9.4
k_{m5}	8	$2.6 \cdot 10^4$
$k5_{stretch}$	1	3.37
$k5_{xb}$	1.5	4.65
k_6	50	$9.8 \cdot 10^4$
k_{m6}	20	585
k_7	30	13.2
$k7_{base}$	2.25	2.18
$k7_{stretch}$	1	1.41
$k7_{force}$	1	$6.0 \cdot 10^{-7}$

pattern D (11.87 mmHg) and E (11.67 mmHg) was reduced in comparison to the maximal pressure of the control case (14.52 mmHg).

Pattern A and C with one linear lesion also caused a reduced change in volume and the maximal pressure, but less distinctive. The isolation of only the pulmonary veins of pattern B had only a minor effect on the activation time. However, it caused a recognizable reduction of the change in volume and the maximal pressure.

The simulation with an increased stiffness of the ablation scar tissue showed similar results (see Fig. 18.6 and Fig. 18.7). The increased stiffness resulted in a further reduction of the change in volume and the maximal pressure for all patterns, depending on the stiffness and the amount of ablated tissue (see Tab. 18.4). But the main effect of the ablation scar on the contraction was definitely caused by the altered activation.

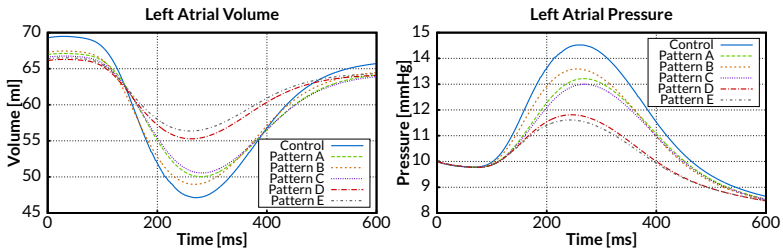


Figure 18.6: Atrial volume and pressure curves for different ablation patterns during the atrial contraction with $4\times$ increased stiffness of the ablation scar.

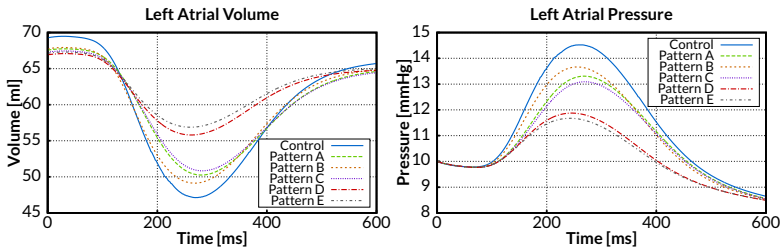


Figure 18.7: Atrial volume and pressure curves for different ablation patterns during the atrial contraction with $8\times$ increased stiffness of the ablation scar.

Simulations of Ventricular Contraction

Fig. 18.8 and Fig. 18.9 show the results of the simulation of the ventricular contraction with an $4\times$ and $8\times$ increased stiffness of the ablation scars. Here the ablation scars had almost no effect on the ventricular pressure and ejection fraction. However, the increased stiffness caused a small reduction of the atrioventricular plane displacement (AVPD) and the change in volume of the atria. Pattern D and E in the simulation with $8\times$ increased stiffness with the two linear lesions showed again the largest effect. Here, the AVPD was reduced from 1.14 mm in the control case to 1.02 mm and 1.04 mm for pattern D and E, respectively. In Fig. 18.10, a visualization of the deformation of the heart during atrial and ventricular contraction is shown exemplarily for pattern A with $8x$ increased stiffness and the control

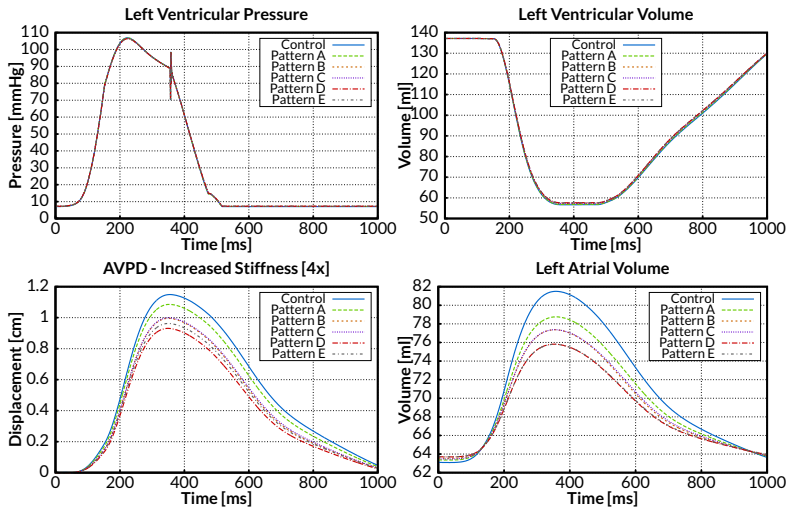


Figure 18.8: Atrial and ventricular volume and pressure curves with different ablation patterns during the ventricular contraction with an $4\times$ increased stiffness of the ablation scar.

case.

18.4 Discussion

To the best of our knowledge, this is the first study where the active atrial contraction is simulated in a model of the whole heart. The hybrid tension development model presented by Sachse et al. (2003a), which was initially developed to model the tension development in human ventricles was adapted to measurement data of the atria presented by Schotten et al. (2002). The output of the adapted model matched well to the measurement data. However, it was not evaluated, if the adapted parameters with physical meaning and a physiological correspondence lie in a realistic range. In the work of Di Martino et al. (2011a), only left atrium is modeled. The atrial pressure was obtained from measurements and applied as loading

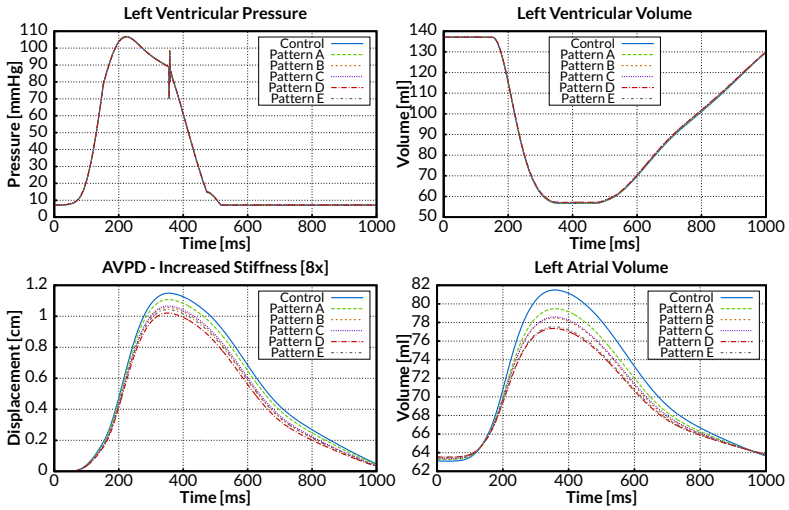


Figure 18.9: Atrial and ventricular volume and pressure curves with different ablation patterns during the ventricular contraction with an $8\times$ increased stiffness of the ablation scar.

Table 18.4: Model outcome of the different simulations: Initial left atrial volume $LA V_0$, percentage change in volume of the left atrium $rel.\Delta V$, left atrial maximal pressure $LA P_{max}$, left ventricular ejection fraction $LV EF$, atrioventricular plane displacement $AVPD$.

	Control	Pattern A	Pattern B	Pattern C	Pattern D	Pattern E
Stiffness 1x						
Atrial Contraction						
LA V_0 [ml]	69.27	69.27	69.27	69.27	69.27	69.27
LA EF [%]	31.9	25.6	27.2	24.4	16.2	15.0
LA P_{max} [mmHg]	14.52	13.3	13.66	13.08	11.87	11.67
Stiffness 4x						
Atrial Contraction						
LA V_0 [ml]	69.27	67.56	67.75	67.28	66.91	67.13
LA EF [%]	31.9	25.6	27.4	24.4	16.6	15.2
LA P_{max} [mmHg]	14.52	13.3	13.66	13.08	11.87	11.67
Ventricular Contraction						
LV EF [ml]	58.7	58.6	58.4	58.5	58.3	58.3
Atrial $rel.\Delta V$ [%]	29.1	25.5	23.7	24.0	21.7	22.0
AVPD [cm]	1.14	1.1	1.05	1.06	1.02	1.04
Stiffness 8x						
Atrial Contraction						
LA V_0 [ml]	69.27	66.95	67.28	66.59	66.13	66.35
LA EF [%]	31.9	25.2	27.2	24.0	16.4	15.0
LA P_{max} [mmHg]	14.52	13.3	13.66	13.08	11.87	11.67
Ventricular Contraction						
LV EF [ml]	58.7	58.5	58.2	58.2	57.9	58.0
Atrial $rel.\Delta V$ [%]	29.1	24.2	21.7	21.8	19.0	18.9
AVPD [cm]	1.14	1.1	1.05	1.06	1.02	1.04

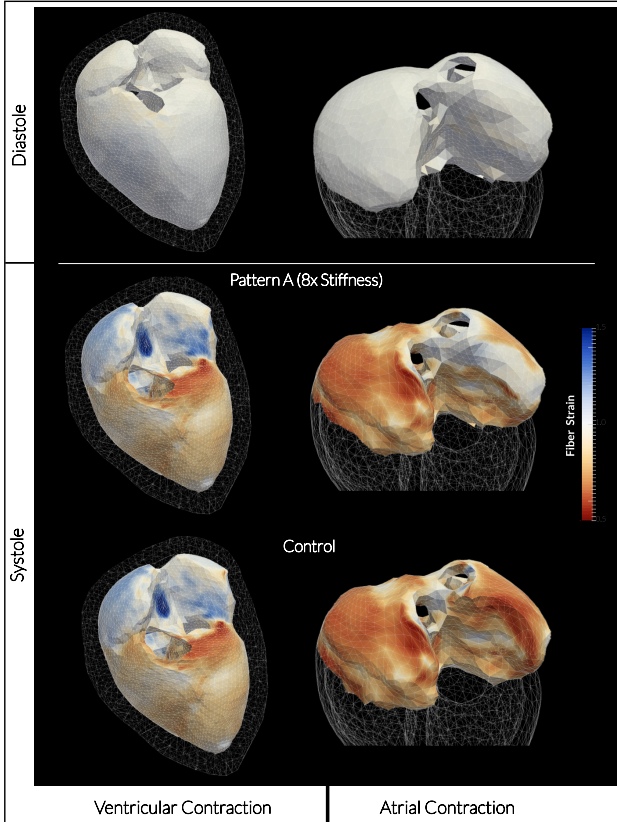


Figure 18.10: Visualization of atrial and ventricular contraction of the heart with ablation pattern A and an $8\times$ increased stiffness and the control case at systole and diastole. The fiber strain is color-coded.

condition to the simulation. The ventricular contraction was modeled by a defined prescription of the displacement of the mitral valve annulus. In this project, the contraction of the atria and the ventricles was simulated in a model of the whole heart. The atrial blood pressure model allowed to evaluate the effect of the ablation scars on the pressure development. In the work of Di Martino et al. (2011a), a rigid pericardium with a *soft surface-to-surface contact* constrained the motion of the atrium. In our model, the implemented contact handling algorithm ensured permanent contact and allowed the heart to slide on the pericardium without friction. The permanent contact of atria and pericardium caused an increase in volume of the atria during the ventricular systole (see Sec. 17.5).

The motion of the atria in our model is constrained by fixating the orifices of the pulmonary veins and venae cavae. The geometrical model of the left atrium used by Di Martino et al. (2011a) included the pulmonary veins. This certainly enabled them to define more realistic boundary conditions, since the elasticity of the vessels allows for some movement of the vessel orifices. In this project, we used the findings of Di Martino et al. (2011a) from the biaxial experiments with porcine atrial tissue to model the passive mechanical properties of the atria.

To the best of our knowledge, this study is the first in-silico evaluation of the impact of scar tissue resulting from RFA on the contraction of atria and ventricles in a model of the whole heart. In the simulations, the altered activation was the main reason for the differences between the different patterns. The stiffness of the ablation scar played a minor role (see Tab. 18.4). All ablation scars reduced the maximal pressure and the stroke volume of the left atrium.

The reduction of the atrial stroke volume was related to the amount of ablation scar tissue. The linear lesions had the strongest impact on atrial contraction. *In-vivo* observations by Takahashi et al. (2007) found a reduced left atrial ejection fraction after ablation procedures. Also Thomas et al. (2000) found that RFA can cause an impairment of the atrial contractility.

We were not able to find any information about the elastomechanical properties of ablation scars in the atria in the literature. Takahashi et al. (2007) suggest that RFA scars in the ventricle behave elastomechanically

like tissue in zones of chronic myocardial infarction. In other simulation studies, the stiffness of cardiac scar tissue was set to be 10 times stiffer than healthy myocardium (Tang et al., 2008; Yang et al., 2012). In this project, we analyzed how the stiffness of the ablation scar affects the results. For that purpose, we conducted simulations with $4\times$ and $8\times$ increased stiffness in comparison to the control case.

In the simulation of the ventricular contraction, the ablation scars reduced the AVPD. Moreover, they reduced the increase in volume of the atria. The linear lesions showed the strongest effect. In 2012, Sato et al. (2012) published measurement data of the left and right atrial volume index (volume per body surface area [ml/m^2]) for the whole heart cycle of a healthy control group ($N=21$) (see Sec. 17.5). They measured an average ejection fraction during atrial systole (defined as the ratio of atrial stroke volume to the volume at the onset of atrial systole) of $36 \pm 4\%$. This matches well to the result of the simulation where we obtained a value of 31.9% for the control case. For the ventricular contraction, they measured an average maximal volume index (V_{max}) of $40\text{ml}/\text{m}^2$ and an average reservoir volume index (V_{res} : Difference between the atrial maximum volume and the smallest atrial volume in mid-diastole) of $12\text{ml}/\text{m}^2$ for the left atrium. This is equivalent to an average increase from the diastolic volume ($V_{max} - V_{res}$) to V_{max} of 52% for the left atrium. The increase in volume which we obtained from the simulations was considerably smaller. This results presumably from the fact, that our model does not include a description of the inflow from the venous system into the atria. Hence, only the stretching of the atria due to the downward movement of the atrioventricular plane could be reproduced in the simulation. However, we assume that if active filling of the atria was taken into account, the relative differences between the different ablation patterns would still be similar. An additional reason for the reduced increase in volume are the restrictive boundary conditions at the vessels orifices. These are actually elastic in reality. The used boundary conditions in our simulations might hinder the deformation of the atria. A further point is the wall thickness of the atria was almost impossible to be recognized from the MRI data. An overestimated wall thickness could also reduce the increase in volume during the contraction.

The ablation scars had almost no impact on the ventricular ejection fraction and ventricular pressure. However, it should not be concluded that therefore, the ablation scars have no negative impact on the pumping functionality of the heart at all. It has to be considered, that in this project, the circulatory system models of the atria and the ventricles were not coupled. In reality, the atria are filled with blood during the ventricular contraction. If the ablation scars reduce the capability of the left atrium to increase its volume, less blood volume is finally available for the ventricular filling. If also the atrial contraction is impaired, this causes a further negative impact on the filling of the ventricles. Consequently, less blood is available to be ejected into the aorta. This effect is even more relevant for elderly people and in general at higher heart rates, where the atrial contraction plays a bigger role (Fuster et al., 2011). For a quantitative evaluation of the impact of the ablation scar on the ventricular ejection fraction, a full description of the whole blood flow from the venous system into the atria and from the atria into the ventricles would be needed. This could probably be achieved only with a fluid mechanical model and in combination with fluid-structure coupling.

18.5 Limitations

The biomechanical model is almost identical to that of Sec. 17. Accordingly, most limitations mentioned in Sec. 17.6 apply also for this project. The geometrical model of the heart did not contain the aorta and pulmonary arteries and apart from that, the orifices of the pulmonary veins and venae cavae were defined to be fixated. In reality, the elasticity of the vessels allows some range of movement. In this project, we simulated the electrical activation and tension development of the ventricles and the atria separately. Atrial and ventricular circulatory system models were not coupled and the atrial model was deactivated during the ventricular contraction and the ventricular model was deactivated during the atrial contraction. The biomechanical properties of the atria and the ablation scars were described with an isotropic material law (Mooney-Rivlin model). However, it can be assumed that the anisotropic material properties strongly influence the atrial contraction. For the simulation, healthy electrophysiology, tension

developed and atrial fiber orientation was chosen. In reality, ongoing AF can lead to electrical, contractile and structural remodeling processes in the atria (Allessie et al., 2002). However, after a successful ablation treatment these processes are often reverted (reverse remodeling). Further, they play rather a minor role for paroxysmal AF. For this project, the geometrical data of only one volunteer was available. For a statistic profound evaluation of the different ablation strategies, it is inevitable to conduct the whole analysis with an adequate number of different geometrical models.

18.6 Future work

In order to obtain a better description of the interplay of atria and ventricles, a coupled circulatory system model of ventricles and atria has to be implemented. A further point is to improve the mechanical modeling of the atria. In 2012 Bellini et al. (2012) presented an advanced material model of the human atria. Based on her work, the description of the biomechanics of the atria in the biomechanical framework could be improved enormously. Furthermore, it should not be forgotten, that every simulation study has its limitations and that the validation of the results based on clinical data is essential. For that purpose, we want to discuss with our clinical partners, if it is possible to obtain clinical data e.g. from cardiac MRI of patients who underwent a RFA, ideally before and after treatment.

Chapter 19

Reconstructon of Left Ventricular Active Tension Distributon from Wall Motion

Simulation Study of The Inverse Problem of Cardiac Mechanics

19.1 Introduction

Medical imaging techniques e.g. MRI, CT or cardioechography allow to evaluate the deformation of the heart, for example by tracking the motion of the heart surfaces. Moreover, techniques like Strain Encoded MRI (SENC) and Tagging MRI allow to obtain direct information on strain and strain rate. However, it has to be considered, that the deformation of the heart results from the active tension development within the cardiac muscle cells. Apart from that, it depends on the passive mechanical properties of the cardiac tissue, the boundary conditions e.g. intraventricular pressure and also the heart geometry. In general, it is not possible to determine internal variables like the active tension or mechanical properties directly from the deformation. If, for example, a particular area of the ventricle does not contract actively anymore, e.g. as consequence of a myocardial infarction,

then this area will still be deformed passively due to the deformation of the adjoining tissue. However, the deformation will certainly differ from that of the healthy case. Apart from that, if a region is identified, which shows an unusual deformation behavior, it is in general very difficult to determine the underlying reason, since it could be caused by a reduced contractility or by altered mechanical properties or a combination of both. Here, a model based approach can help to get a better insight and to reconstruct these hidden parameters. In context of this work, I have developed an inverse solving algorithm (inverse solver - see Sec. 15.1), which is able to reconstruct the active tension development from the motion of heart surfaces.

In this project, the inverse solver is evaluated in a simulation study. The objectives are: Is the inverse solver able to reproduce the heart motion and does it reconstruct the active tension distribution in the ventricles satisfactorily? What happens, if the active tension pattern is altered, e.g. due to electrical inactive regions resulting from a ventricular infarction? In this case, is the algorithm still able to reconstruct the active tension and to identify those regions with no active tension development which are only deformed indirectly by the surrounding myocardium? For that purpose, the acCELLerate framework was used to simulate the active tension development in the ventricles for three different left ventricular transmural infarctions and a control case with a regular electrical activation. This provided the input for the biomechanical simulation framework, which was used to calculate the corresponding contraction of the heart (*forward simulations*). From the results, the left ventricular and right ventricular endocardial surfaces were extracted for each timestep, which provided the synthetic clinical data. This data was used as input for the inverse solver, which then was requested to reconstruct the active tension based on the provided motion of the endocardial surfaces (*inverse simulation*) for each time step. Finally, the reconstructed heart motion and the reconstructed active tension data (inverse solution) were compared with that of the forward simulation in order to evaluate the inverse solver.

19.2 Methods

Geometrical Model

The geometrical models, which were used for the electrophysiological simulation (ventricles) and biomechanical simulation (whole heart) are described in Sec. 10. However, since the inverse solver is very numerically demanding, the model of the pericardium was not included in order to reduce the complexity and thus the simulation time. For the electromechanical simulations, a stimulation profile was generated as described in Sec. 3.3. Here, the impact of the infarction scar on the Purkinje network was not taken into account.

Four different simulation settings were generated for the electrophysiological simulation: One for the control case and three with an infarction scar. The infarction scar areas had been assigned manually in the geometrical model. They were all located in the left ventricle (Fig. 19.1). The first on the anterior side of the ventricle (*infarction 1*), the second on the posterior side (*infarction 2*) and the third infarction was located in the septum (*infarction 3*).

Simulation Settings

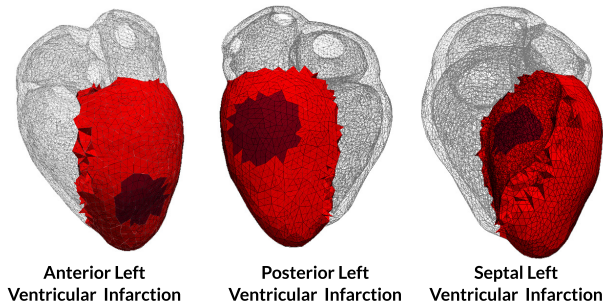


Figure 19.1: Three different simulation setups with transmural left ventricular infarctions were generated: *infarction 1*: anterior, *infarction 2*: posterior, *infarction 3*: septal. The tissue of the infarction scar area (dark red) was defined to be not excitable.

The electrophysiology on cellular level was simulated using the ten Tusscher model (Sec. 3.2). The infarction areas were defined to be not excitable.

The active tension development was simulated using the HTD model (Sec. 3.3). The monodomain model was used to simulate the excitation propagation (Sec. 3.4). The resulting tension development data was interpolated to the elements of the left and right ventricle for the biomechanical simulation.

For the biomechanical simulation, the material properties of the ventricles were described using the Guccione *et al.* model while the Mooney-Rivlin model was used for the atria. The parameters were set according to the findings of Omens *et al.* (1993) for the ventricles, while for the atria the parameters presented in (Di Martino *et al.*, 2011a) were used (average of the values for left atrium anterior (LA_{ant}) and left atrium posterior (LA_{ant})). The parameters are given in Tab. 19.1. The elastic properties of the infarction areas were not changed.

Table 19.1: Material parameters for the Guccione *et al.* and Mooney-Rivlin model

C [Pa]	b_1	b_2	b_3	K [Pa]
1200	26.7	2.0	14.7	1e6

c_1 [Pa]	c_2 [Pa]	K [Pa]
7450	0	0
		1e6

For the forward simulation, each ventricle was coupled with a 3-element Windkessel model. The parameters for the Windkessel model were taken from (Stergiopoulos *et al.*, 1999) and are given in Tab. 19.2.

Table 19.2: Parameters used for the Windkessel models.

C	5.16 ml/mmHg
R_1	0.030 mmHg s/ml
R_2	0.63 mmHg s/ml
Initial aortic pressure	67.5 mmHg
Initial pulmonary artery pressure	15.0 mmHg

In reality, the contraction of the heart is delayed regarding the active tension development due to the mass inertia. However, the current version of the inverse solver does not consider mass inertia yet. In order to analyse, how

this affects the inverse solution, the contraction of the heart was calculated twice for each infarction scar and the control case, once with the static solver and once with the dynamic solver. Here, the Rayleigh damping parameter were set to $\alpha_1 = 100$ and $\alpha_2 = 0.005$.

From the results of the forward calculation, the endocardial surfaces of the right and left ventricle were extracted for each time step and used as target surfaces for the inverse solver (see Sec. 15.1). The epicardial surface was not considered.

For each of the eight forward simulations, two inverse simulations were conducted: One with spatial regularization only, where $\lambda_6 = 10^{-14}$ (Eq. 15.11) and all remaining parameters λ_X were set to zero and a second inverse simulation with additional temporal regularization with $\lambda_4 = 10^{-20}$. The parameter λ_6 controls the smoothness of the active tension distribution. If the value is too small, the solution gets very inhomogeneous. On the other side, if the value is too big, the details of the active tension pattern vanish. The parameter λ_4 controls the temporal smoothness. If the value is too small, the solution shows strong oscillations, while if the value is too large, the original active tension time course can not be reproduced satisfactorily. A suitable compromise had to be found for both parameters, which was done manually by trying different combinations of values. The active tension was reconstructed for the ventricles only and the distance between the source and target surfaces was evaluated at approximately 900 location on the endocardial surfaces. The passive mechanical properties, the fiber orientation and the boundary conditions were identical to those of the forward simulation. While the pressure for the forward simulation was calculated using the Windkessel models, the pressure for the inverse simulation was directly taken from the results of the forward simulation and applied to the ventricular cavities.

19.3 Results

Control Case

A visualization of the epicardial and the endocardial surfaces of the static forward simulation and the inverse simulation for the control case at four

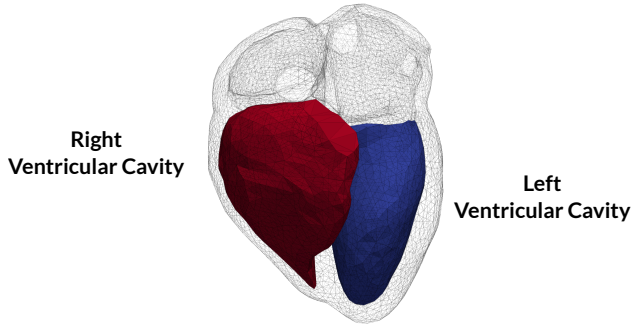


Figure 19.2: The left and right endocardial surface which enclose the ventricular cavities were extracted from the results of the forward simulations and provided the input for the inverse reconstruction of the cardiac deformation and the active tension development

different time steps is given in Fig. 19.3. The source and target surfaces (endocardium) match very well to each other. Moreover, also the epicardial surfaces of forward and inverse simulation show a very good match. That is remarkable, since the inverse solver did only consider the endocardial surfaces for the optimization of the active tension. The average distance between target and source surfaces of the inverse solution for the control case is given in Fig. 19.4. One stop criterion for the inverse solver was an average distance between source and target surface of less than 0.4 mm. For the reconstruction of active tension of the static forward simulation for the control case, this criterion was always fulfilled. For the reconstruction of the active tension of the dynamic forward simulation, this criterion was not fulfilled for only a few time steps. For these steps either the maximal number of estimation steps or the relative change of the distance between two steps was the relevant criterion. However, the maximal average distance between source and target surfaces is 0.54 mm for the reconstruction of the dynamic forward simulation with Laplacian regularization and 0.44 mm for the reconstruction with additional time regularization. The static forward simulation for the control case took 58 min while the inverse solver needed 11 : 03 h for the reconstruction.

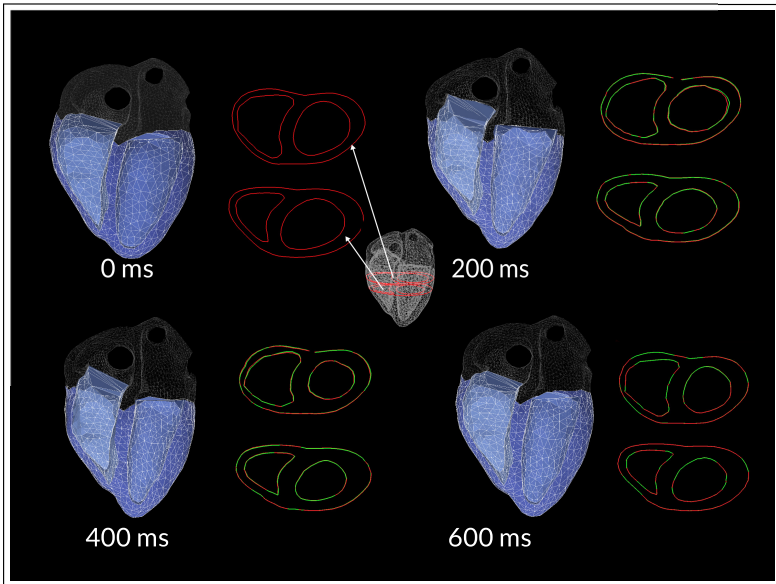


Figure 19.3: Visualization of the surfaces obtained the forward simulation (wire-frame/red) and the surfaces obtain from the inverse reconstruction and (solid/green) at four different time steps in a cutaway view and in two slices (control case)

Both simulations were conducted on a desktop computer using one CPU and a simulation time step size of 10 ms.

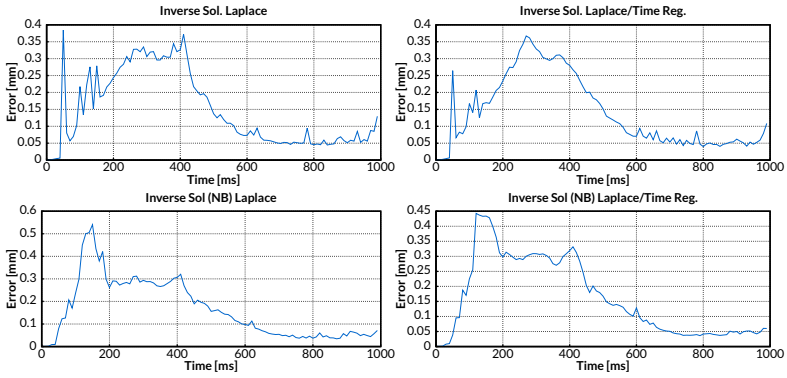


Figure 19.4: Distance between source and target surfaces for the control case

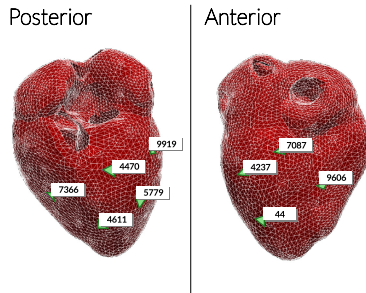


Figure 19.5: Element indices for which the time course of the active tension is given in Fig. 19.6

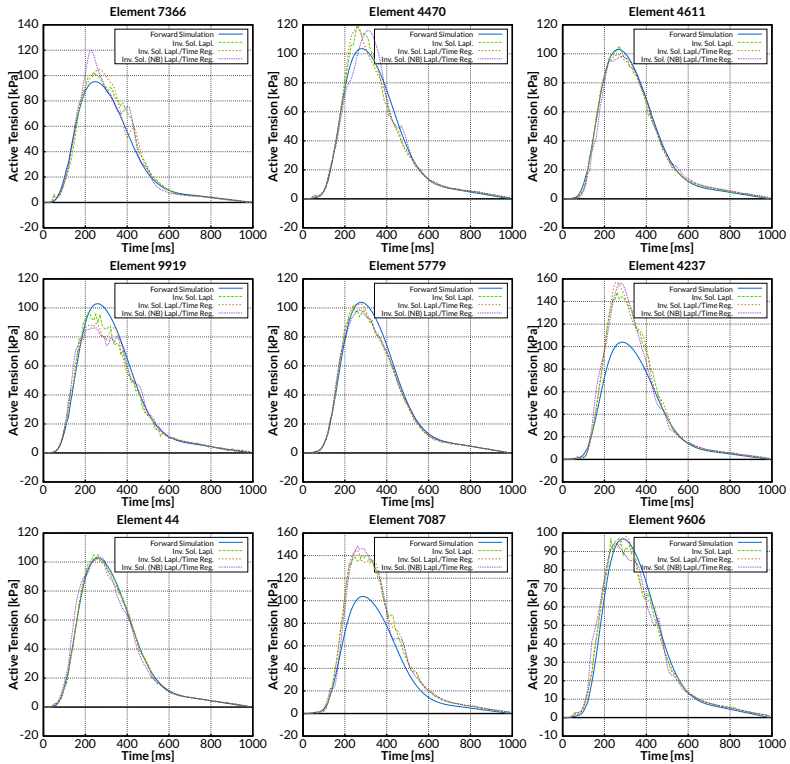


Figure 19.6: Time course of the reconstructed active tension in eight selected elements for the control case

In Fig. 19.7 and Fig. 19.8, the original active tension distributions of the forward simulation (static and dynamic) for the control case and their inverse reconstruction are visualized for four time steps. On the left, the active tension and the resulting deformation of the forward simulation are shown. In the middle, the inverse reconstruction using spatial Laplacian regularization is shown. On right, the results for additional time regularization are shown. For the static forward simulation, both inverse reconstructions match very well to the forward simulation. By optical inspection, it is difficult to tell which result is better. However, a look on the time course of the reconstructed active tension within the elements reveals, that the

time regularization has a distinct temporal smoothing effect. The inverse reconstructions of the active tension from the surface motion obtained from the dynamic forward simulation show also a good match to the forward simulation. However, the active tension is sometimes significantly overestimated or underestimated in some regions.

In Fig. 19.5 time courses of the active tension, which were reconstructed from the surface motion obtain from the static forward simulation (control case) are shown for an exemplarily selection of elements. The elements were selected more or less randomly (as random as possible for a human) without knowing the active tension time course of these elements beforehand (no pick and chose of optimal results). For most of the elements, the original active tension time course and the reconstructed time course match well to each other. However, for two elements (4337 and 7087), the maximal active tension was significantly overestimated. Some curves show strong oscillations near to the peak, in particular those of the inverse reconstruction without time regularization. The temporal smoothing effect of the time regularization is clearly recognizable.

Infarction Settings

The results for the distances between source and target surface for the simulations with infarction scar were similar to those of the control case. Here the maximal average distance (0.57 mm) is found for the reconstruction of the active tension based on the endocardial surface motion obtained from the dynamic forward simulation for infarction setting 2. Visualizations of the reconstructed active tension from the heart motion of the dynamic and static forward simulation for the different infarction settings are given in Fig. 19.9 to Fig. 19.14. In all reconstructions, the infarction area is clearly visible. The active tension in this area is significantly reduced and almost zero around the center. Due to the smoothing effect of the spatial regularization, the sharp edge between active and inactive areas of the forward simulation is considerably blurred in the solution of the inverse solver. In the reconstruction of the active tension based on the surface motion of the dynamic forward simulation, the infarction scar is also clearly visible.

However, the inverse solver again overestimates the active tension in some regions.

19.4 Discussion

The inverse solver performed very well on the reproduction of the deformation of the heart. Not only the endocardial surface matched well to the forward simulation, but also the epicardial surface showed a good match. This was the case even though the epicardial surface was not chosen as target surface and therefore was not considered for the inverse solution. Due to the incompressibility of the myocardial tissue, a good match of the endocardial surfaces comes along with a good match of the epicardial surface.

Moreover, also the reconstruction of the active tension was remarkably good considering the fact, that only the motion of the endocardial surfaces of the ventricles and the blood pressure were used as input data. If it can be confirmed that it is in general sufficient to provide the endocardial surfaces for the reconstruction, this would mean a great advantage for the application of the inverse solver on to clinical data. Due to the high contrast between blood and myocardial tissue in most of the medical imaging modalities, the automatic tracking of the endocardial surface is much easier to accomplish than for the epicardial surface.

The time regularization helped to obtain a stable and temporal smooth solution. Without time regularization, the active tension had some strong oscillations, in particular near its peak. The oscillations could probably also be reduced by decreasing the stop criterion for the average distance between source and target surfaces but this would come along with significant increase of the simulation time.

The reconstruction of the active tension for the dynamic forward simulation showed a good match to the original active tension as well. However, the

inverse solver does not consider mass inertia effects. Therefore, the active tension is sometimes distinctly over- or underestimated. If for example the active tension starts to increase at the beginning of simulation, the motion of the wall follows with a delay. Accordingly, the inverse solver will underestimate the active tension at that point of time. Later, when the active tension starts to decline, again the mass inertia causes that the movement of the ventricular tissue does not instantaneously follow the active tension time course. Now, the inverse solver will overestimate the active tension. This could be solved by considering the mass inertia for the inverse solution, but in reality it is not so trivial to determine the damping parameters of the myocardium. Apart from that, it would introduce a further uncertainty into the inverse simulation. Apart from that, the mass inertia of the blood volume will probably play an even more important role and is not considered in the biomechanical model yet.

The reconstruction of motion and active tension for the infarction scars showed also a good match to the forward simulation and the active tension in the area of the infarction scar was significantly reduced and almost zero near its center. Here, the smoothing effect of the spatial regularization caused a strong blurring of the edge between scar tissue and myocardial tissue.

To the best of my knowledge, this is the first time, that spatial and temporal Tikhonov regularization, a method well established for solving the inverse problem of ECG imaging (Farina, 2008), is applied to the *inverse problem of cardiac mechanics* in order to reconstruct the time course of the active tension distribution from the motion of the heart surfaces in a whole heart model. The inverse solver estimates the complete time course of the active tension distribution for each FEM element of the left and right ventricle. In this project, the active tension was estimated for 7469 elements and the discrepancy of source and target surfaces was assessed at approximately 900 locations. The gradient matrix \mathbf{A} (Eq. 15.9) was determined by calculating a reduced inverse of the gradient stiffness matrix. Here, using T10 tetrahedral elements for the static solver step but T4 tetrahedral elements for the estimation step (Sec. 15.2) reduces the numerical complexity massively for the estimation step, while it retains the excellent convergence behaviour of the T10 elements for the static solver step. The dimension

of the reduced inverse of the gradient stiffness matrix was 2508×6411 . Using only T10 elements would result with the same settings in a matrix with a dimension of 2508×40665 .

Delingette et al. (2012) used a variational data assimilation approach to estimate the maximal contractility in three predefined regions (left ventricle, right ventricle, scar region). Marchesseau et al. (2013b) used unscented Kalman filtering from regional volumes to estimate the maximal contractility from cardiac cine-MRI. Global parameters were estimated with an automatic calibration algorithm, based on the Unscented Transform. Eventually, in all 17 AHA (American Heart Association) zones of the left ventricle, the maximal contractility was estimated using the reduced-order unscented Kalman filtering. Wong et al. (2014) presented a derivative-free optimization approach based on a velocity-based objective function and estimated additionally to the maximal contractility, contraction and relaxation rates. He tested the method with three different types of zone partitioning (3 zones, 5 zones and 17 AHA zones).

To my understanding, all these approaches parameterize a complete electromechanical model considering parameters for the electrophysiology, circulation and contractility e.g. maximal contractility and contractility rate. In contrast to that, the inverse solver reconstructs for every time step that active tension distribution, which results in the same surface motion as of the provided input data. While this works excellent, the inverse solver does not consider the cardiac electrophysiology. If for example the boundary conditions are not set carefully, the inverse solver would certainly still reconstruct a motion which matches well to the input data (as long as it is possible with the given boundary conditions), but the reconstructed active tension could be completely unphysiological. It is thinkable, that this could be improved by using an electrophysiological model for a further regularization.

19.5 Limitations

For the inverse solution in this study, the boundary conditions, the blood pressure in the cavities, the fiber orientation and the passive mechanical properties were all known. However, if this method is applied on real

clinical data, these parameters have either to be measured, which comes along with measurement uncertainties, or have to be estimated which is even worse. It is very likely, that inaccuracies of these parameters will distort the reconstruction of the active tension. It will probably still provide a solution where the deformation of the heart matches well to the measurement data, but with a strong deviation of the active tension reconstruction from *real* active tension. If for example the heart tissue in a certain area of the ventricle is stiffer than in the rest of the tissue, e.g. due to fibrosis, and this is not considered for the inverse solution, the inverse solver will mistakenly assume, that this region has a reduced active tension development. Inaccuracies of the measured blood pressure or the fiber orientation will in the same way falsify the active tension. Moreover, the motion of the heart depends strongly on the boundary conditions. If the biomechanical model does not consider these boundary conditions accurately enough, this will also have a strong falsifying impact on the reconstruction.

19.6 Outlook

The first step has to be a sensitivity analysis in order to evaluate how inaccuracies of fiber orientation, passive mechanical properties, blood pressure and boundary conditions affect the reconstruction of the active tension. As mentioned above, locally altered passive mechanical properties which are not considered in the model will be reflected in the reconstruction of the active tension. In this context, it would be interesting to evaluate if it is possible to define a measure which does not directly correspond to a physical parameter like the stiffness or the active tension development of the tissue but holds information about the ability of the tissue to contract and thus is of diagnostic value for the cardiologist.

Another point is the fiber orientation. It is definitely thinkable, that also the fiber orientation can be reconstructed from the heart motion in a similar way as the active tension. For the active tension reconstruction, one step is to calculate a Jacobian matrix which holds the information on how the nodal forces depend on the magnitude of the active tension. In the same way, a Jacobian matrix could be calculated which additionally contains

the information on how the nodal forces depend on the *direction* of the active tension. Eventually, the inverse solver would reconstruct an active tension vector field which reproduces the measured deformation of the heart under consideration of the regularization requirements. Since in reality, the active tension acts along the fiber orientation, this active tension vector field could be used to estimate the fiber orientation. A further aspect is the consideration of further measurement data for the inverse solution. For example strain, which can be measured using SENC MRI is definitely a promising candidate which can further improve the solution.

After the inverse solver has sufficiently been evaluated on simulation data, the next step will be the application on clinical data. Here, an interesting project would be to apply the inverse solver on medical imaging data of a patient with a known infarction scar, that is also visible in the late enhancement MRI. This would allow to evaluate, if that scar tissue is also identifiable in the inverse solution. If this is the case, then the inverse solver might also be able to identify impairments of the contractility e.g. due to cardiomyopathy which can directly be measured with current medical imaging technology. The imaging of the cardiac strain is a standard clinical procedure in order to assess the cardiac performance. If additionally to that, also information about the contractility can be estimated, then this would be certainly a further valuable information for the cardiologist.

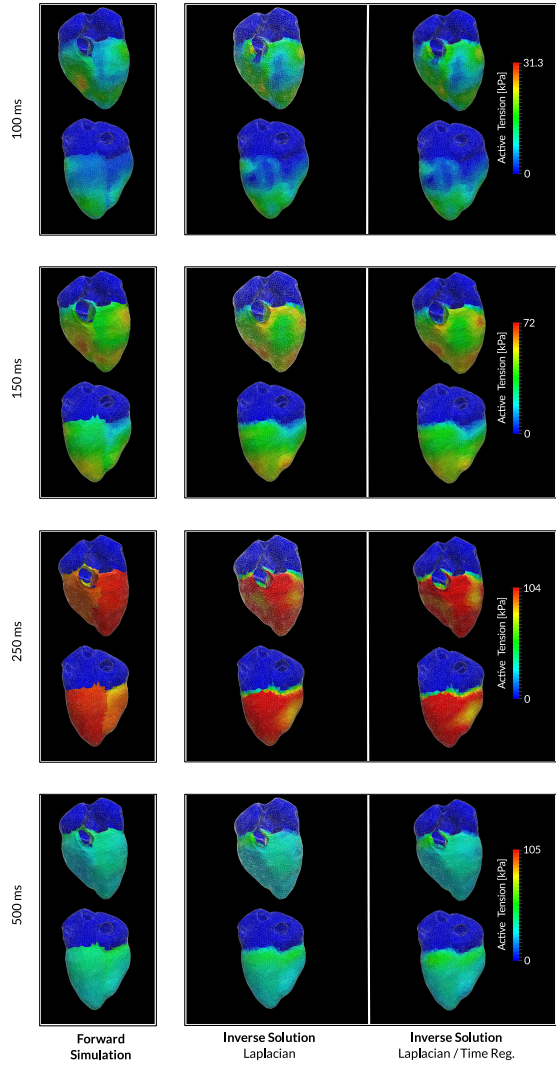


Figure 19.7: Static forward simulation for the control case at four different time steps (left) and the associate inverse reconstruction of deformation and active tension development using spatial Laplacian regularization (middle) and additional time regularization (right)

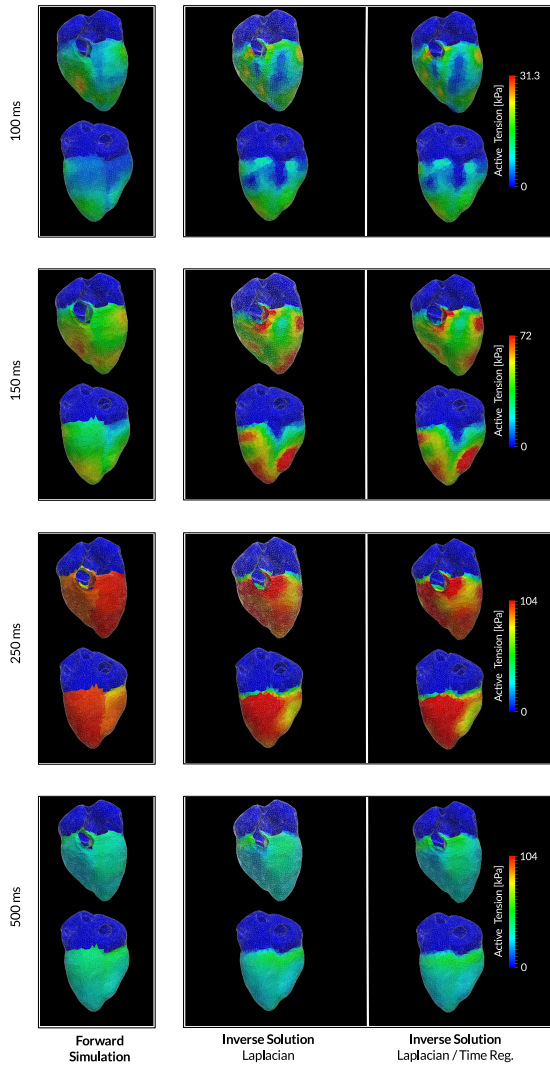


Figure 19.8: Dynamic forward simulation (Newmark Beta) for the control case at four different time steps (left) and the associate inverse reconstruction of deformation and active tension development using spatial Laplacian regularization (middle) and additional time regularization (right)

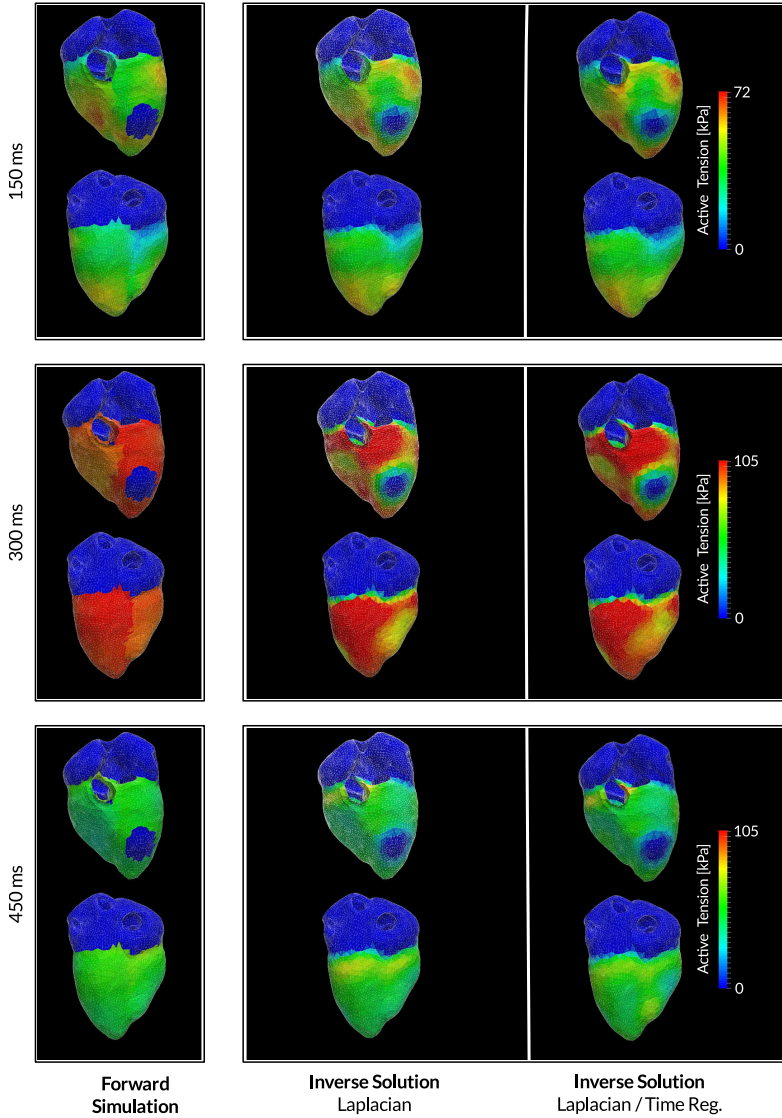


Figure 19.9: Static forward simulation for infarction setting 1 at three different time steps (left) and the associate inverse reconstruction of deformation and active tension development using spatial Laplacian regularization (middle) and additional time regularization (right)

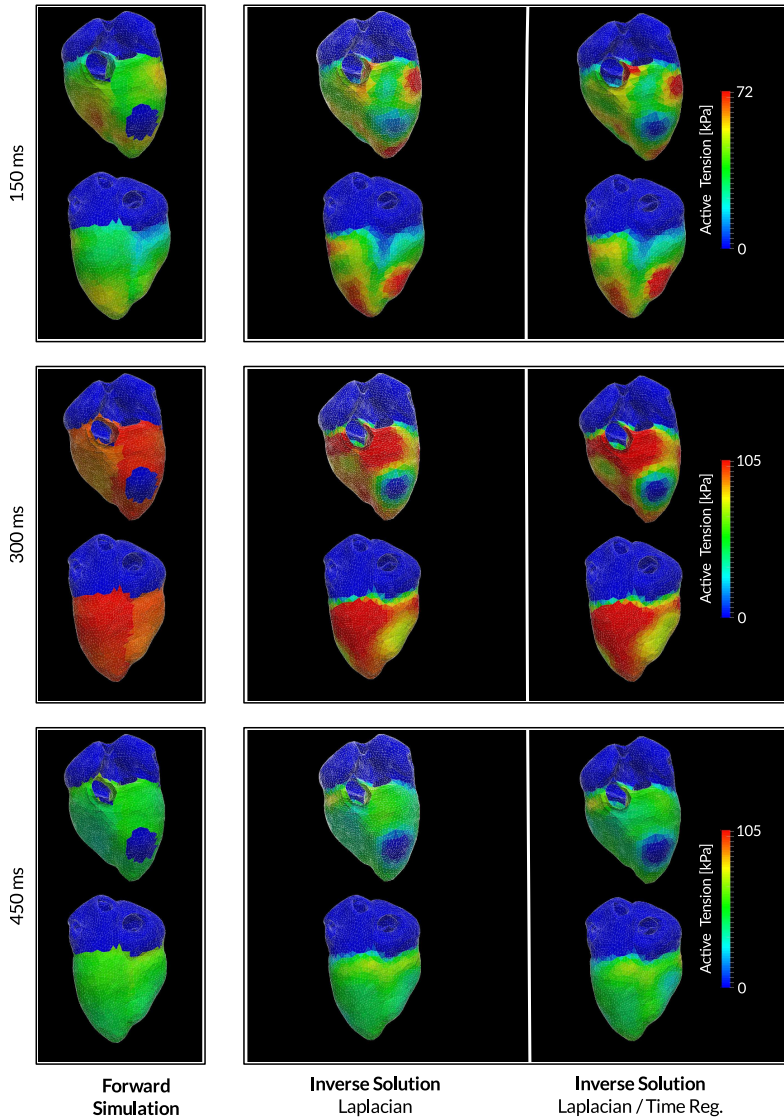


Figure 19.10: Dynamic forward simulation (Newmark Beta) for the infarction setting 1 at three different time steps (left) and the associate inverse reconstruction of deformation and active tension development using spatial Laplacian regularization (middle) and additional time regularization (right)

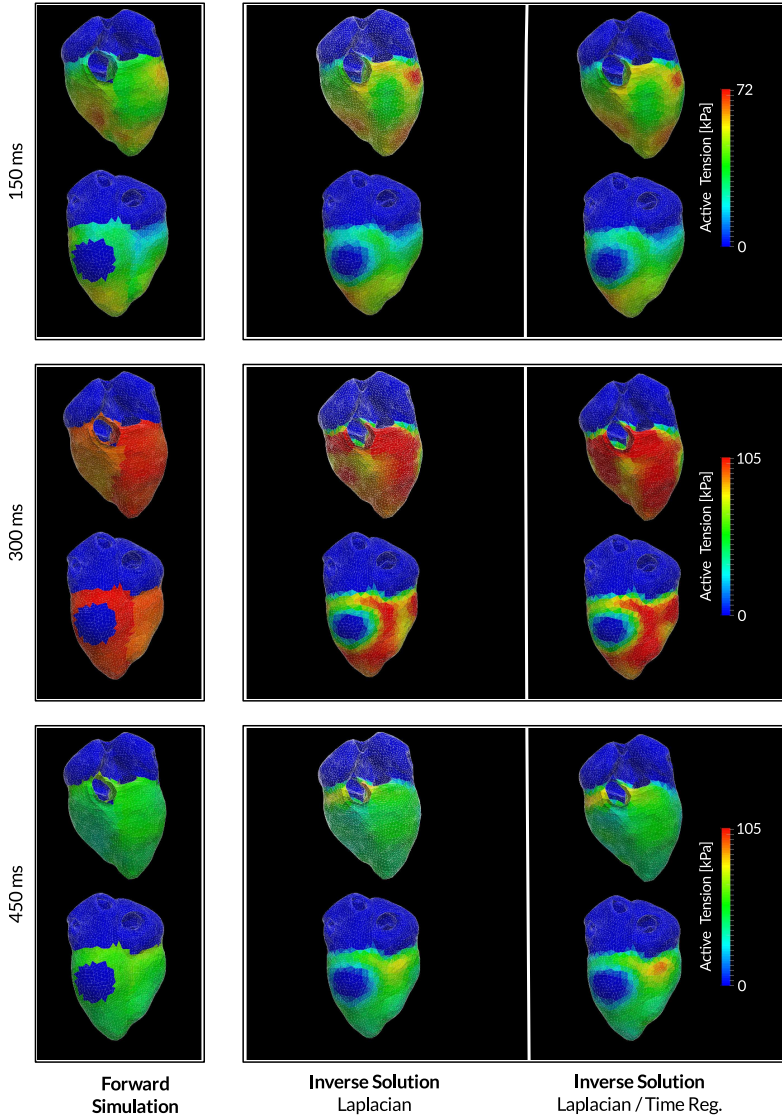


Figure 19.11: Static forward simulation for infarction setting 2 at three different time steps (left) and the associate inverse reconstruction of deformation and active tension development using spatial Laplacian regularization (middle) and additional time regularization (right)

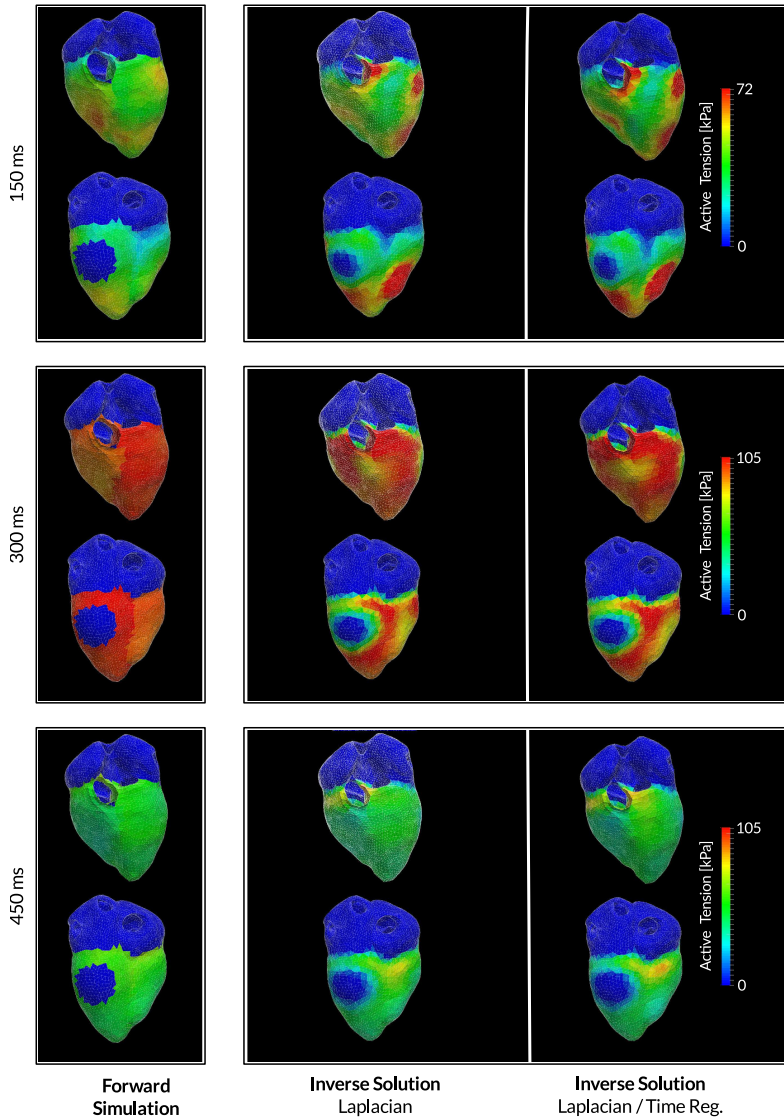


Figure 19.12: Dynamic forward simulation (Newmark Beta) for the infarction setting 2 at three different time steps (left) and the associate inverse reconstruction of deformation and active tension development using spatial Laplacian regularization (middle) and additional time regularization (right)

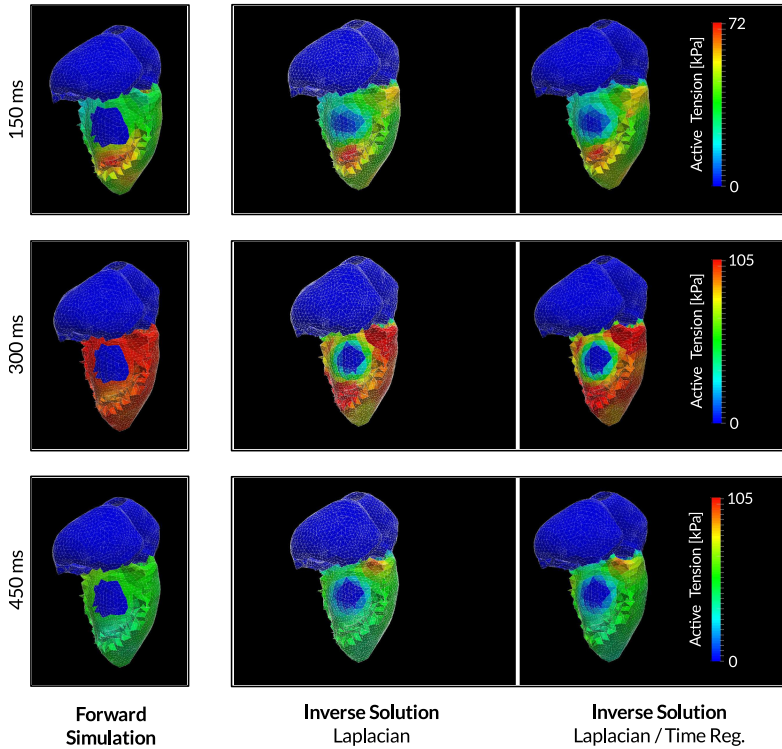


Figure 19.13: Static forward simulation for infarction setting 3 at three different time steps (left) and the associate inverse reconstruction of deformation and active tension development using spatial Laplacian regularization (middle) and additional time regularization (right)

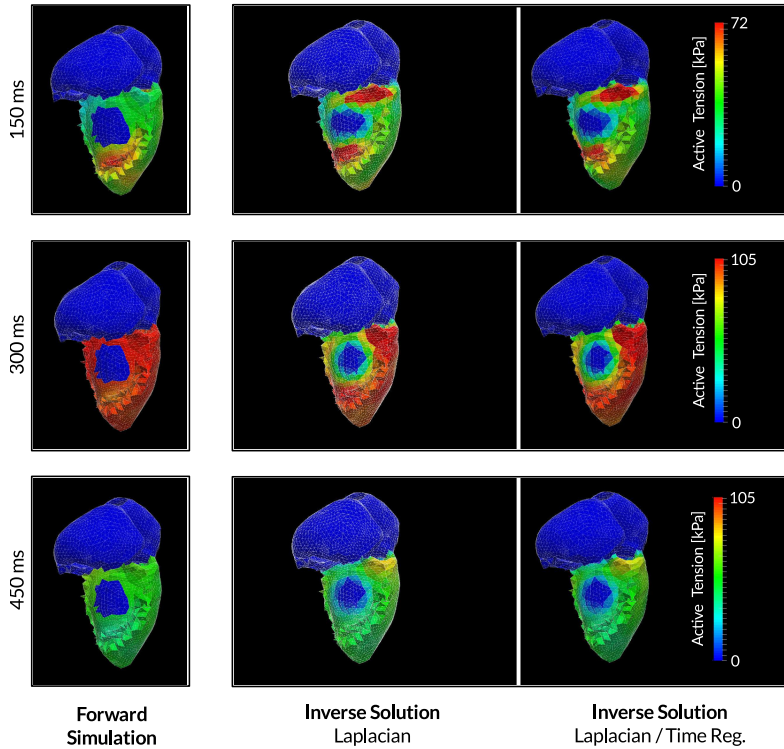


Figure 19.14: Dynamic forward simulation (Newmark Beta) for the infarction setting 3 at 3 different time steps (left) and the associate inverse reconstruction of deformation and active tension development using spatial Laplacian regularization (middle) and additional time regularization (right)

Chapter 20

Summary and Conclusions

In context of this thesis, a simulation framework for modeling the human cardiac biomechanics has been developed. In the first part of this thesis, an overview of the basic fundamentals of the cardiac anatomy and physiology, nonlinear continuum mechanics and the finite element method as well as some aspects of cardiac modeling have been given. Part two has described the biomechanical simulation framework and the implemented algorithm. In part three, the validation of the framework was presented. Furthermore, three selected projects which were conducted using the biomechanical simulation framework have been presented.

The simulation delivered correct results for all of the validation tests and also the preliminary results for the benchmark study were almost identical to those of the other participating groups.

In the first project, the interplay of the ventricles with the atria and of the whole heart with the pericardium was analyzed. The results showed, that for the simulation with pericardium, the contraction of the heart showed a better match to the MRI data than for the simulation without pericardium. Moreover, the whole deformation was smoother and the outer contour was only slightly deformed, as it is also case for a healthy heart in reality. Moreover, the pericardium synchronized the contraction of the left and right ventricle, as it is also assumed to be the case in reality. In contrast to that, in the simulation without pericardium, the heart showed an unphysiological deformation while the outer contour was significantly deformed during the

cardiac cycle. These results match well to the echocardiography findings for patients with congenital absence of the pericardium. Furthermore, the interplay of atria and ventricles is crucial in order to obtain a realistic AVPD. Considering the fact, that the AVPD plays an essential role for the ventricular filling, the atria should be taken into account for the simulation of the heart contraction in order to obtain a realistic result, even if the focus of the study lies only on the ventricles.

In the second project, five different commonly used ablation patterns in the left atrium have been analyzed regarding their impact on the atrial and ventricular contraction. In the simulations, the ablation scars caused a reduction of the change in volume and reduced the maximal pressure of the left atrium for the atrial systole depending on the applied ablation pattern. The major effect of the ablation scar on the contraction was caused by the altered activation. Here, the linear lesions had the strongest influence. During the ventricular contraction, the increased stiffness of the ablation scar resulted in a reduction of the change in volume of the left atria and the AVPD. Again, the linear lesions showed the strongest effect. If the available blood volume in the left atrium is reduced due to an impaired filling and a reduced AVPD and moreover, the active contraction of the atrium is impaired, then this can be a reason for a reduced filling of the left ventricle and therefore, have a negative impact on the heart pumping function. One should always avoid to derive statement about reality to quickly from simulation results. However, the simulations support the hypothesis, that RFA can have a negative effect on the pumping function of the heart and that the effect depends on the chosen ablation pattern. The third project evaluated the algorithm of the inverse solver on synthetic data obtained from forward simulations of the contraction of a healthy heart and from three forward simulations of the contraction of the heart with different infarction scar areas. The inverse solver did a good job on the reconstruction of the active tension distribution and the reproduction of the deformation. The active tension matched well regarding spatial distribution and the time course. Moreover, the infarction scar areas were clearly visible and the active tension in these areas was almost zero as it was also the case for the forward simulation. This is remarkable, considering the fact, that the inverse solver had only information about

the motion of the endocardial surface and the blood pressure time course. However, one should not forget, that the simulation settings regarding geometry, boundary conditions and passive mechanical properties were identical for the forward and inverse simulation. It has to be evaluated, how uncertainties regarding these parameters affect the reconstruction.

Danksagung

Diese Arbeit hätte in der gegebenen Form niemals ohne den vielseitigen Beitrag Dritter entstehen können. Diesen möchte ich im Folgenden aufs Herzlichste danken.

Zu allererst bedanke ich mich bei Prof. Dr. rer. nat. Olaf Dössel, für die Möglichkeit in seiner Arbeitsgruppe zu arbeiten, für die hervorragende und geduldige Betreuung und stete Unterstützung. Desweiteren danke ich Assoz. Prof. Priv.-Doz. Dipl.-Ing. Dr.techn. Gernot Plank für die Übernahme des Korreferats. Bei Dr.-Ing. Gunnar Seeman bedanke ich mich für die hervorragende und für den Erfolg dieser Arbeit massgebliche Betreuung in seiner Arbeitsgruppe Herzmodellierung. Darüberhinaus danke ich all meinen Kollegen, den Studenten und Mitarbeitern des Instituts für die produktive Zusammenarbeit, die gute Arbeitsatmosphäre und den ausgeprägten Unterhaltungswert. Zu guter Letzt danke ich von Herzen meiner Familie und Alex für die stete Unterstützung und Geduld.

Bibliography

- K. Alfakih, S. Plein, H. Thiele, T. Jones, J. P. Ridgway, and M. U. Sivananthan. Normal human left and right ventricular dimensions for MRI as assessed by turbo gradient echo and steady-state free precession imaging sequences. *Journal of Magnetic Resonance Imaging*, 17(3):323–329, 2003. ISSN 1522-2586. doi: 10.1002/jmri.10262.
- T. Alhogbani, O. Strohm, and M. G. Friedrich. Evaluation of left atrial contraction contribution to left ventricular filling using cardiovascular magnetic resonance. *J Magn Reson Imaging*, 37(4):860–864, Apr 2013.
- M. Alessie, J. Ausma, and U. Schotten. Electrical, contractile and structural remodeling during atrial fibrillation. *Cardiovascular Research*, 54: 230–246, 2002. ISSN 0008-6363.
- S. Balay, J. Brown, K. Buschelman, W. D. Gropp, D. Kaushik, M. G. Knepley, L. Curfman McInnes, B. F. Smith, and H. Zhang. PETSc Web page, 2012. <http://www.mcs.anl.gov/petsc>.
- C. Bellini, E. S. Di Martino, and S. Federico. Mechanical behaviour of the human atria. *Ann Biomed Eng*, pages 1–13, 2012.
- T. Belytschko, W. K. Liu, B. Moran, et al. *Nonlinear finite elements for continua and structures*. Wiley New York, 2000.
- S. Benussi, C. Pappone, S. Nascimbene, G. Oreto, A. Caldarola, P. L. Stefano, V. Casati, and O. Alfieri. A simple way to treat chronic atrial fibrillation during mitral valve surgery: the epicardial radiofrequency approach. *European Journal of Cardio-Thoracic Surgery : Official*

- Journal of the European Association for Cardio-Thoracic Surgery*, 17: 524–529, 2000. ISSN 1010-7940.
- D. Bers. *Excitation-Contraction Coupling and Cardiac Contractile Force*. Kluwer Academic Publishers, Dordrecht, 1991.
- Blender, 2014. URL <http://www.blender3d.org>.
- J. Bonet. *Nonlinear continuum mechanics for finite element analysis*. Cambridge university press, 1997.
- L.-M. Busch, T. Fritz, M. Krueger, G. Seemann, and O. Dössel. Impact of different ablation patterns on the biomechanics of the human left atrium. In *Biomedical Engineering/Biomedizinische Technik, Proceedings BMT Band 58, Heft SI-1 Track-N*, 2013.
- M. Carlsson, M. Ugander, H. Mosén, T. Buhre, and H. Arheden. Atrioventricular plane displacement is the major contributor to left ventricular pumping in healthy adults, athletes, and patients with dilated cardiomyopathy. *Am J Physiol-Heart C*, 292(3):1452–1459, 2007.
- J. Constantino, Y. Hu, and N. A. Trayanova. A computational approach to understanding the cardiac electromechanical activation sequence in the normal and failing heart, with translation to the clinical practice of crt. *Progress in biophysics and molecular biology*, 110(2):372–379, 2012.
- K. Costa, P. Hunter, J. Wayne, L. Waldman, J. Guccione, and A. McCulloch. A three-dimensional finite element method for large elastic deformations of ventricular myocardium: Ii-prolate spheroidal coordinates. *Journal of Biomechanical Engineering*, 118:464–472, 1996.
- M. Courtemanche, R. J. Ramirez, and S. Nattel. Ionic mechanisms underlying human atrial action potential properties: Insights from a mathematical model. *Am. J. Physiol.*, 275:H301–H321, 1998.
- H. Delingette, F. Billet, K. Wong, M. Sermesant, K. Rhode, M. Ginks, C. Rinaldi, R. Razavi, and N. Ayache. Personalization of cardiac motion and contractility from images using variational data assimilation. *Biomedical Engineering, IEEE Transactions on*, 59(1):20–24, Jan 2012. ISSN 0018-9294. doi: 10.1109/TBME.2011.2160347.

- E. S. Di Martino, C. Bellini, and D. S. Schwartzman. In vivo porcine left atrial wall stress: Computational model. *J Biomech*, 44(15):2589–2594, 2011a.
- E. S. Di Martino, C. Bellini, and D. S. Schwartzman. In vivo porcine left atrial wall stress: Effect of ventricular tachypacing on spatial and temporal stress distribution publisher = Elsevier, volume = 44,. *J Biomech*, 44(15):2755–2760, 2011b.
- O. Dössel, M. Krueger, F. Weber, M. Wilhelms, and G. Seemann. Computational modeling of the human atrial anatomy and electrophysiology. *Medical & Biological Engineering & Computing*, 50(8):773–799, 2012. ISSN 0140-0118. doi: 10.1007/s11517-012-0924-6.
- M. J. Earley and R. J. Schilling. Catheter and surgical ablation of atrial fibrillation. *Heart (British Cardiac Society)*, 92:266–274, 2006. ISSN 1355-6037.
- M. D. Eggen and C. M. Swingen. Cardiovascular magnetic resonance imaging. In P. A. Iaizzo, editor, *Handbook of Cardiac Anatomy, Physiology, and Devices*, pages 341–362. Humana Press, 2009. ISBN 978-1-60327-371-8.
- K. Emilsson, L. Brudin, and B. Wandt. The mode of left ventricular pumping: is there an outer contour change in addition to the atrioventricular plane displacement? *Clin Physiol*, 21(4):437–446, 2001.
- T. S. E. Eriksson, A. J. Prassl, G. Plank, and G. A. Holzapfel. Modeling the dispersion in electromechanically coupled myocardium. *International Journal for Numerical Methods in Biomedical Engineering*, 29(11):1267–1284, 2013. ISSN 2040-7947. doi: 10.1002/cnm.2575.
- D. Farina. *Forward and inverse problems of electrocardiography: Clinical investigations*. Dissertation, Institut für Biomedizinische Technik, Universität Karlsruhe (TU), 2008.
- G. L. Freeman and W. C. Little. Comparison of in situ and in vitro studies of pericardial pressure-volume relation in dogs. *Am J Physiol-Heart C*, 251(2):H421–H427, 1986.

- T. Fritz, C. Wieners, G. Seemann, H. Steen, and O. Dössel. Simulation of the contraction of the ventricles in a human heart model including atria and pericardium. *Biomech Model Mechanobiol*, 2013. doi:doi:10.1016/j.jcp.2012.09.015.
- Y. Fung. *Biomechanics: Mechanical Properties of Living Tissues*. Springer, New York, Berlin, Heidelberg, 1993.
- V. Fuster, L. E. Rydén, D. S. Cannom, H. J. Crijns, A. B. Curtis, K. A. Ellenbogen, J. L. Halperin, J.-Y. Le Heuzey, G. N. Kay, J. E. Lowe, et al. Acc/aha/esc 2006 guidelines for the management of patients with atrial fibrillation: full text a report of the american college of cardiology/american heart association task force on practice guidelines and the european society of cardiology committee for practice guidelines (writing committee to revise the 2001 guidelines for the management of patients with atrial fibrillation) developed in collaboration with the european heart rhythm association and the heart rhythm society. *Europace*, 8(9):651–745, 2006.
- V. Fuster, L. E. Ryden, D. S. Cannom, H. J. Crijns, A. B. Curtis, K. A. Ellenbogen, J. L. Halperin, G. N. Kay, J. Y. Le Huezey, J. E. Lowe, S. B. Olsson, E. N. Prystowsky, J. L. Tamargo, L. S. Wann, S. C. Smith, S. G. Priori, N. A. Estes, M. D. Ezekowitz, W. M. Jackman, C. T. January, J. E. Lowe, R. L. Page, D. J. Slotwiner, W. G. Stevenson, C. M. Tracy, A. K. Jacobs, J. L. Anderson, N. Albert, C. E. Buller, M. A. Creager, S. M. Ettinger, R. A. Guyton, J. L. Halperin, J. S. Hochman, F. G. Kushner, E. M. Ohman, W. G. Stevenson, L. G. Tarkington, C. W. Yancy, T. E. Arend, A. B. McDougall, M. D. Stewart, S. A. Keller, E. A. Barrett, K. Petrie, P. Christiansen, M. C. Wheeler, R. M. Robertson, K. A. Taubert, A. J. Howard, K. H. McGregor, and V. L. Dean. 2011 ACCF/AHA/HRS focused updates incorporated into the ACC/AHA/ESC 2006 guidelines for the management of patients with atrial fibrillation: a report of the American College of Cardiology Foundation/American Heart Association Task Force on practice guidelines. *Circulation*, 123(10):269–367, Mar 2011.

- A. Gordon and E. Regnier, M. Homsher. Skeletal and cardiac muscle contractile activation: Tropomyosin "rocks and rolls". *News Physiol. Sci.*, 16:H49–H55, 2001.
- J. Guccione, A. McCulloch, and L. Waldman. Passive material properties of intact ventricular myocardium determined from a cylindrical model. *J Biomech Eng*, 113:42–55, 1991.
- V. Gurev, T. Lee, J. Constantino, H. Arevalo, and N. A. Trayanova. Models of cardiac electromechanics based on individual hearts imaging data. *Biomech Model Mechanobiol*, 10(3):295–306, 2011.
- M. Hadjicharalambous, R. Chabiniok, L. Asner, E. Sammut, J. Wong, G. Carr-White, J. Lee, R. Razavi, N. Smith, and D. Nordsletten. Analysis of passive cardiac constitutive laws for parameter estimation using 3d tagged MRI. *Biomechanics and Modeling in Mechanobiology*, pages 1–22, 2014. ISSN 1617-7959. doi: 10.1007/s10237-014-0638-9.
- A. L. Hodgkin and A. F. Huxley. A quantitative description of membrane current and its application to conduction and excitation in nerve. *J Physiol*, 117(4):500–544, 1952.
- J. P. Holt. The normal pericardium. *Am J Cardiol*, 26(5):455–465, 1970.
- G. A. Holzapfel and R. W. Ogden. Constitutive modelling of passive myocardium: a structurally based framework for material characterization. *Philosophical Transactions of the Royal Society A: Mathematical, Physical and Engineering Sciences*, 367(1902):3445–3475, 2009.
- P. Hunter, M. Nash, and G. Sands. Computational electromechanics of the heart. In A. Panfilov and A. Holden, editors, *Computational Biology of the Heart*, pages 345–408. John Wiley & Sons, Chichester, 1997a.
- P. Hunter, B. Smaill, P. Nielsen, and I. Le Grice. A mathematical model of cardiac anatomy. In A. Panfilov and A. Holden, editors, *Computational Biology of the Heart*, pages 171–213. John Wiley & Sons, Chichester, 1997b.

- S. R. Jernigan, G. D. Buckner, and J. W. Eischen. Finite element modeling of the left atrium to facilitate the design of an endoscopic atrial retractor. *J Biomech Eng*, 129(6):825–837, 2007. doi: 10.1115/1.2801650.
- J. Keener and J. Sneyd. Mathematical Physiology II: Systems Physiology. In S. Antman, J. Marsden, and L. Sirovich, editors, *Interdisciplinary Applied Mathematics*, volume 8/2. Springer New York, 2009a. ISBN 978-0-387-79387-0.
- J. Keener and J. Sneyd. Mathematical Physiology I: Cellular Physiology. In S. Antman, J. Marsden, and L. Sirovich, editors, *Interdisciplinary Applied Mathematics*, volume 8/1. Springer New York, 2009b. ISBN 978-0-387-75846-6.
- D. U. J. Keller. Detailed anatomical and electrophysiological modeling of human ventricles based on diffusion tensor MRI. Diplomarbeit, Institut für Biomedizinische Technik, Universität Karlsruhe (TH), Karlsruhe, 2006.
- D. U. J. Keller, R. Kalayciyan, O. Dössel, and et. al. Fast creation of endocardial stimulation profiles for the realistic simulation of body surface ecgs. In *IFMBE Proceedings World Congress on Medical Physics and Biomedical Engineering*, volume 25/4, pages 145–148. Springer, 2009.
- R. C. P. Kerckhoffs, A. D. McCulloch, J. H. Omens, and L. J. Mulligan. Effect of pacing site and infarct location on regional mechanics and global hemodynamics in a model based study of heart failure. In *Functional Imaging and Modeling of the Heart*, pages 350–360. Springer, 2007.
- B. C. Knollmann and D. M. Roden. A genetic framework for improving arrhythmia therapy. *Nature*, 451:929–936, 2008.
- A. Krishnamurthy, C. T. Villongco, J. Chuang, L. R. Frank, V. Nigam, E. Belezzuoli, P. Stark, D. E. Krummen, S. Narayan, J. H. Omens, A. D. McCulloch, and R. C. P. Kerckhoffs. Patient-specific models of cardiac biomechanics. *J Comput Phys*, 2012. doi: 10.1016/j.jcp.2012.09.015.
- M. Krueger, V. Schmidt, C. Tobón, F. Weber, C. Lorenz, D. Keller, H. Barschdorf, M. Burdumy, P. Neher, G. Plank, et al. Modeling atrial

- fiber orientation in patient-specific geometries: a semi-automatic rule-based approach. *Functional Imaging and Modeling of the Heart*, 6666: 223–232, 2011.
- M. Krueger, W. Schulze, K. Rhode, R. Razavi, G. Seemann, and O. Dössel. Towards personalized clinical in-silico modeling of atrial anatomy and electrophysiology. *Medical & Biological Engineering & Computing*, 51 (11):1251–1260, 2013. ISSN 0140-0118.
- M. W. Krueger. *Personalized Multi-Scale Modeling of the Atria: Heterogeneities, Fiber Architecture, Hemodialysis and Ablation Therapy*. Dissertation, Institute for Biomedical Engineering, Karlsruhe Institute of Technology (KIT), Karlsruhe, 2012.
- S. Land, S. Niederer, P. Lamata, and N. Smith. Improving the stability of cardiac mechanical simulations. *Biomedical Engineering, IEEE Transactions on*, PP(99):1–1, 2014. ISSN 0018-9294. doi: 10.1109/TBME.2014.2373399.
- T. Laske, M. Shrivastav, and P. Iaizzo. The cardiac conduction system. In P. A. Iaizzo, editor, *Handbook of Cardiac Anatomy, Physiology, and Devices*, pages 159–175. Humana Press, 2009. ISBN 978-1-60327-371-8.
- J. M. Lee and D. R. Boughner. Mechanical properties of human pericardium. differences in viscoelastic response when compared with canine pericardium. *Circ Res*, 57(3):475–481, 1985.
- I. J. LeGrice, Y. Takayama, and J. W. Covell. Transverse shear along myocardial cleavage planes provides a mechanism for normal systolic wall thickening. *Circ Res*, 77(1):182–193, 1995.
- K. Loushin, J. Quill, and P. Iaizzo. Mechanical aspects of cardiac performance. In P. A. Iaizzo, editor, *Handbook of Cardiac Anatomy, Physiology, and Devices*, pages 271–296. Humana Press, 2009. ISBN 978-1-60327-371-8.
- F. Mantovani, A. Barbieri, and M. G. Modena. Congenital complete absence of the pericardium: A multimodality imaging diagnostic approach. *Echocardiogr J*, 28(1):E21–E22, 2011.

- S. Marchesseau, H. Delingette, M. Sermesant, and N. Ayache. Fast parameter calibration of a cardiac electromechanical model from medical images based on the unscented transform. *Biomech Model Mechanobiol*, 12:815–831, 2013a.
- S. Marchesseau, H. Delingette, M. Sermesant, R. Cabrera-Lozoya, C. Tobon-Gomez, P. Moireau, R. Figueras i Ventura, K. Lekadir, A. Hernandez, M. Garreau, et al. Personalization of a cardiac electromechanical model using reduced order unscented kalman filtering from regional volumes. *Medical image analysis*, 17(7):816–829, 2013b.
- J. E. Marine, J. Dong, and H. Calkins. Catheter ablation therapy for atrial fibrillation. *Progress in Cardiovascular Diseases*, 48:178–192, 2005. ISSN 0033-0620.
- F. H. Martini, M. J. Timmons, and R. B. Tallitsch. *Human anatomy*. Pearson Education, 7 edition, 2011.
- A. McCulloch. Cardiac biomechanics. In J. Bronzino, editor, *The Biomedical Engineering Handbook*, pages 28–1. CRC Press, 2000.
- P. Moireau and D. Chapelle. Reduced-order unscented kalman filtering with application to parameter identification in large-dimensional systems. *ESAIM: Control, Optimisation and Calculus of Variations*, 17(02):380–405, 2011.
- MPI-Forum. MPI: A message-passing interface standard. Technical report, University of Tennessee, Knoxville, TN, USA, 1994.
- P. Nielsen, I. Le Grice, B. Smaill, and P. Hunter. The role of the pericardium in interactions between the cardiac chambers. *Am Heart J*, 106:1377–1783, 1983.
- P. Nielsen, I. Le Grice, B. Smaill, and P. Hunter. Mathematical model of geometry and fibrous structure of the heart. *Am. J. Physiol*, 260(29): H1365–H1378, 1991.
- J. H. Omens, D. A. MacKenna, and A. D. McCulloch. Measurement of strain and analysis of stress in resting rat left ventricular myocardium. *J Biomech*, 26(6):665–676, 1993.

- C. Pappone, G. Oreto, F. Lamberti, G. Vicedomini, M. L. Loricchio, S. Shpun, M. Rillo, M. P. Calabro, A. Conversano, S. A. Ben-Haim, R. Cappato, and S. Chierchia. Catheter ablation of paroxysmal atrial fibrillation using a 3d mapping system. *Circulation*, 100:1203–1208, 1999. ISSN 0009-7322.
- E. R. Pfeiffer, J. R. Tangney, J. H. Omens, and A. D. McCulloch. Biomechanics of cardiac electromechanical coupling and mechanoelectric feedback. *Journal of biomechanical engineering*, 136(2):021007, 2014.
- P. Psychidis-Papakyritsis, A. de Roos, and L. Kroft. Functional MRI of congenital absence of the pericardium. *American Journal of Roentgenology*, 189(6):W312–W314, 2007.
- J. Rice, R. L. Winslow, and W. C. Hunter. Comparison of putative cooperative mechanisms in cardiac muscle: Length dependence and dynamic responses. *Am. J. Physiol.*, 276:H1734–H1754, 1999.
- E. S. Richardson, A. Hill, N. Skadsberg, M. Ujhelyi, Y.-F. Xiao, and P. Iaizzo. The pericardium. In P. A. Iaizzo, editor, *Handbook of Cardiac Anatomy, Physiology, and Devices*, pages 125–136. Humana Press, 2009. ISBN 978-1-60327-371-8.
- J. Richter. Modeling the tension development and the active contraction of the human atria. Diplomarbeit, Institute of Biomedical Engineering, Karlsruhe Institute of Technology (KIT), Karlsruhe, 2012.
- F. Sachse, K. Glänzel, and G. Seemann. Modeling of protein interactions involved in cardiac tension development. *Int. J. Bifurc. Chaos*, 13: 3561–3578, 2003a.
- F. Sachse, G. Seemann, K. Chaisaowong, and M. Mohr. Modeling of electro-mechanics of human cardiac myocytes: parameterization with numerical minimization techniques. In *Engineering in Medicine and Biology Society, 2003. Proceedings of the 25th Annual International Conference of the IEEE*, volume 3, pages 2810–2813 Vol.3, Sept 2003b. doi: 10.1109/IEMBS.2003.1280502.

- F. B. Sachse, A. P. Moreno, G. Seemann, and et. al. A model of electrical conduction in cardiac tissue including fibroblasts. *Annals of Biomedical Engineering*, 37:874–889, 2009. ISSN 1521-6047.
- T. Sato, I. Tsujino, N. Oyama-Manabe, H. Ohira, Y. Ito, A. Yamada, D. Ikeda, T. Watanabe, and M. Nishimura. Right atrial volume and phasic function in pulmonary hypertension. *Int J Cardiol*, 2012. doi: 10.1016/j.ijcard.2012.09.133.
- H. Schmid. *Passive myocardial mechanics : constitutive laws and materials parameter estimation*. PhD thesis, The University of Auckland, 2006.
- R. Schmidt and F. Lang. *Physiologie des Menschen*. Springer, 30 edition, 2007.
- V. Schmidt. Semi-automatische Methode zur Modellierung der Faserorientierung in patienten-spezifischen Vorhofgeometrien. Diplomarbeit, Institut für Biomedizinische Technik, Karlsruher Institut für Technologie (KIT), Karlsruhe, 2010.
- U. Schotten, M. Greiser, D. Benke, and et. al. Atrial fibrillation-induced atrial contractile dysfunction: a tachycardiomyopathy of a different sort. *Cardiovascular Research*, 53:192–201, 2002. ISSN 0008-6363.
- U. Sechtem, P. W. Pflugfelder, R. G. Gould, M. Cassidy, and C. B. Higgins. Measurement of right and left ventricular volumes in healthy individuals with cine mr imaging. *Radiology*, 163(3):697–702, 1987.
- G. Seemann. *Modeling of Electrophysiology and Tension Development in the Human Heart*. Dissertation, Institut für Biomedizinische Technik, Universität Karlsruhe, 2005.
- G. Seemann, F. Sachse, M. Karl, D. Weiss, V. Heuveline, and O. Dössel. Framework for modular, flexible and efficient solving the cardiac bidomain equations using petsc. *Progress in Industrial Mathematics at ECMI 2008*, 15(2):363–369, 2010.

- M. Sermesant, R. Chabiniok, P. Chinchapatnam, T. Mansi, F. Billet, P. Moireau, J. Peyrat, K. Wong, J. Relan, K. Rhode, M. Ginks, P. Lambiase, H. Delingette, M. Sorine, C. Rinaldi, D. Chapelle, R. Razavi, and N. Ayache. Patient-specific electromechanical models of the heart for the prediction of pacing acute effects in CRT: A preliminary clinical validation. *Medical Image Analysis*, 16(1):201–215, 2012.
- H. Si. Tetgen: A quality tetrahedral mesh generator and three-dimensional delaunay triangulator (user manual), 2013. URL <http://tetgen.berlios.de/>.
- B. Smaill and P. Hunter. Structure and function of the diastolic heart: Material properties of passive myocardium. In L. Glass, P. Hunter, and A. McCulloch, editors, *Theory of Heart*, Institute for Nonlinear Science, pages 1–29. Springer New York, 1991. ISBN 978-1-4612-7803-0.
- J. Spudich. Timeline: The myosin swinging cross-bridge model. *Nature Reviews Molecular Cell Biology*, 2:H387–H392, 2001.
- N. Stergiopoulos, B. E. Westerhof, and N. Westerhof. Total arterial inertance as the fourth element of the windkessel model. *Am J Physiol-Heart C*, 276(1):H81–H88, 1999.
- D. Streeter. Gross morphology and fiber geometry of the heart. *Handbook of physiology*, pages 61–112, 1979.
- Y. Takahashi, M. D. O’Neill, M. Hocini, and et. al. Effects of stepwise ablation of chronic atrial fibrillation on atrial electrical and mechanical properties, 2007. ISSN 1558-3597.
- D. Tang, C. Yang, T. Geva, and et. al. Patient-specific MRI-based 3d fsi RV/LV/patch models for pulmonary valve replacement surgery and patch optimization. *Journal of Biomechanical Engineering*, 130:041010, 2008. ISSN 0148-0731.
- K. ten Tusscher, D. Noble, P. Noble, and A. Panfilov. A model for human ventricular tissue. *Am J Physiol-Heart C*, 286(4):1573–1589, 2004.

- S. P. Thomas, I. A. Nicholson, G. R. Nunn, A. Rees, L. Trieu, M. P. Daly, E. M. Wallace, and D. L. Ross. Effect of atrial radiofrequency ablation designed to cure atrial fibrillation on atrial mechanical function. *Journal of cardiovascular electrophysiology*, 11(1):77–82, 2000.
- A. Tikhonov and V. Arsenin. *Solutions of ill-posed problems*. Scripta series in mathematics. Winston, 1977. ISBN 9780470991244.
- Y. Topilsky, N. Tabatabaei, W. K. Freeman, H. Saleh, H. Villarraga, and S. L. Mulvagh. Pendulum heart in congenital absence of the pericardium. *Circulation*, 121(10):1272–1274, 2010.
- N. A. Trayanova. Whole-heart modeling: Applications to cardiac electrophysiology and electromechanics. *Circulation Research*, 108(1): 113–128, 2011. doi: 10.1161/CIRCRESAHA.110.223610.
- N. A. Trayanova, J. Constantino, and V. Gurev. Electromechanical models of the ventricles. *American Journal of Physiology - Heart and Circulatory Physiology*, 301(2):H279–H286, 2011. doi: 10.1152/ajp-heart.00324.2011.
- L. Tung. *A bidomain model for describing ischemic myocardial d-c potentials*. PhD thesis, Massachusetts Institute of Technology, 1978.
- J. V. Tyberg, G. C. Taichman, E. R. Smith, N. W. Douglas, O. A. Smiseth, and W. J. Keon. The relationship between pericardial pressure and right atrial pressure: an intraoperative study. *Circulation*, 73(3):428–432, 1986.
- V. Wang, H. Lam, D. Ennis, B. Cowan, A. Young, and M. Nash. Modelling passive diastolic mechanics with quantitative MRI of cardiac structure and function. *Medical Image Analysis*, 13(5):773–784, 2009.
- M. W. Watkins and M. M. LeWinter. Physiologic role of the normal pericardium. *Annu Rev Med*, 44(1):171–180, 1993.
- N. Westerhof, G. I. J. S. Elzinga, and P. Sipkema. An artificial arterial system for pumping hearts. *J Appl Physiol*, 31(5):776–781, 1971.

- R. Willenheimer, C. Cline, L. Erhardt, and B. Israelsson. Left ventricular atrioventricular plane displacement: an echocardiographic technique for rapid assessment of prognosis in heart failure. *Heart*, 78(3):230–236, 1997.
- C. Wong, M. Sermesant, K. Rhode, M. Ginks, C. Rinaldi, R. Razavi, H. Delingette, and N. Ayache. Velocity-based cardiac contractility personalization from images using derivative-free optimization. *Journal of the Mechanical Behavior of Biomedical Materials*, 2014. doi: <http://dx.doi.org/10.1016/j.jmbbm.2014.12.002>.
- P. Wriggers. *Computational contact mechanics*. Springer, 2006.
- J. Xi, P. Lamata, J. Lee, P. Moireau, D. Chapelle, and N. Smith. Myocardial transversely isotropic material parameter estimation from in-silico measurements based on a reduced-order unscented kalman filter. *Journal of the Mechanical Behavior of Biomedical Materials*, 4(7):1090–1102, 2011. cited By 23.
- C. Yang, D. Tang, T. Geva, and et. al. Using contracting band to improve right ventricle ejection fraction for patients with repaired tetralogy of fallot, a modeling study using patient-specific cmr-based 2-layer anisotropic models of human right and left ventricles. *The Journal of Thoracic and Cardiovascular Surgery*, 2012. ISSN 0022-5223.

List of Publications and Supervised Theses

Journal Articles

- **Fritz, T.** Wieners, C. Seemann, G. Steen, H. Dössel, O., *Simulation of the contraction of the ventricles in a human heart model including atria and pericardium : Finite element analysis of a frictionless contact problem*, Biomechanics and Modeling in Mechanobiology, 13, 627-641, 2014
- Keller, D. U. J. and Jarrousse, O. and **Fritz, T.** and Ley, S. and Dössel, O. and Seemann, G. *Impact of physiological ventricular deformation on the morphology of the T-wave: a hybrid, static-dynamic approach*, IEEE Transactions on Biomedical Engineering, 58, 2109-2119, 2011

Conference Contributions

- **Fritz, T.** Seemann, G. Dössel, O., *Reconstruction of Left Ventricular Active Tension Distribution from Wall Motion - Simulation Study of the Inverse Problem of Cardiac Mechanics*, Biomedizinische Technik / Biomedical Engineering, 59 (s1), 2014
- **Fritz, T.** Dössel, O. Krueger M.W., *Electromechanical modeling of the human atria*, Biomedizinische Technik / Biomedical Engineering, 58 (s1), 2013

- **Fritz, T.** Krueger M.W., Busch, L.-M. Dössel, O., *FEM-Analysis of the Impact of Different Atrial Ablation Patterns on the Cardiac Pumping Performance*, 1st International Workshop on Latest Advances in Cardiac Modeling, Garching near Munich, 2013
- **Fritz, T.** Dössel, O. Krueger M.W., *Simulating the beating heart within the pericardium using finite element analysis*, Biomedizinische Technik / Biomedical Engineering 57 (s1), 2012
- **Fritz, T.** Dössel, O., *Finite Element Analysis of the Beating Heart within the Pericardium: A Frictionless Contact Problem*, European Solid Mechanics Conference, Graz, 2012
- **Fritz, T.** Seemann, G. Dössel, O., *Analyzing transmural myocardial infarction of the left ventricle using computer modeling*, 4th Cardiac Physiome Workshop, Oxford, 2011
- **Fritz, T.** Jarrousse, O Keller, D.U.J. Seemann, G. Dössel, O., *In silico analysis of the impact of transmural myocardial infarction on cardiac mechanical dynamics for the 17 AHA segments*, Proceedings of the 6th International Conference on Functional Imaging and Modeling of the Heart (FIMH), LNCS 6666, 241-249, 2011
- **Fritz, T.** Dössel, O., *Finite Element Based Electromechanical Modeling of the Heart Dynamics with Left Ventricular Transmural Infarction*, Biomedizinische Technik / Biomedical Engineering; 56 (s1), 2011
- **Fritz, T.** Jarrousse O. Seemann G. Dössel O., *Elastomechanical Modeling of the Human Heart - From Ion Channels to Contraction*, 3rd GAMM Seminar on Continuum Biomechanics, Freudenstadt-Lauterbad, 2010
- **Fritz, T.** Jarrousse O. Seemann G. Dössel O., *Analyzing the transmural electromechanical heterogeneity of the left ventricle in a computer model.*, Biomedizinische Technik / Biomedical Engineering; 55 (s1), 2010

- **Fritz, T.** Jarrousse, O. Dössel, O., *Adapting a mass-spring system to energy density function describing myocardial mechanics*, Proceedings of the 4th European Congress for Medical and Biomedical Engineering 2008. 23-27 November 2008, Antwerp, Belgium, 22, 2003-2006, 2008
- Schulze, W. H. W. **Fritz, T.** Potyagaylo, D. Trächtler, J. Schimpf, R. Papavassiliu, T. Tülümen, E. Rudic, B. Liebe, V. Doesch, C. Borggrefe, M. Dössel, O., *Effect of mesh resolution on forward calculations of the electrocardiogram in a simplified thorax model*, Biomedizinische Technik / Biomedical Engineering, 59 (s1), 945-948, 2014
- Baron, L. **Fritz, T.** Seemann, G. Dössel, O., *Sensitivity study of fiber orientation on stroke volume in the human left ventricle*, Computing in Cardiology, 2014
- Busch, L.-M. **Fritz, T.** Krueger, M. W. Seemann, G. Dössel, O., *Impact of different ablation patterns on the biomechanics of the human left atrium*, Biomedizinische Technik / Biomedical Engineering, 58 (s1), 2013
- Krueger, M. W. Schmidt, V. Keller, D. U. J. **Fritz, T.** Seemann, G. Dössel, O., *Comparison of Methods for Visualization of 3D Myocardial Fiber Structure in Printed Images*, KIT PhD Symposium 2010
- Jarrousse, O. **Fritz, T.** Dössel, O., *Modeling breast tissue mechanics from prone to supine positions with a modified mass-spring system*, Proceedings BMT 2010, 44. DGBMT Jahrestagung, 3-Länder-Tagung D-A-CH, Rostock, 55, 87-90, 2010
- Jarrousse, O. **Fritz, T.** Dössel, O., *Implicit time integration in a volumetric mass-spring system for modeling myocardial elastomechanics*, IFMBE Proceedings World Congress on Medical Physics and Biomedical Engineering, 25/4, 876-879, 2009
- Jarrousse, O. **Fritz, T.** Dössel, O., *A volumetric mass-spring system for modeling myocardial elastomechanics*, The Cardiac Physiome:

Multi-scale and Multi-physics Mathematical Modelling Applied to the Heart, 2009

- Jarrousse, O. **Fritz, T.** Dössel, O., *A modified mass-spring system for myocardial mechanics modeling*, Proceedings of the 4th European Congress for Medical and Biomedical Engineering 2008. 23-27 November 2008, Antwerp, Belgium, 22, 1943-1946, 2008

Thesis

- **Thomas Fritz**, *Analyzing the electro-mechanical heterogeneity of the heart using computer modeling*, Diplomarbeit, Universität Karlsruhe (TH), Karlsruhe, 2009

Supervised Student Theses

- Tobias Hauser, *Eine Sensitivitätsanalyse zum Einfluss von Faserorientierung und elektrophysiologischem Stimulationsprofil auf die Biomechanik des Herzens*, Diplomarbeit, Institute of Biomedical Engineering, Karlsruhe Institute of Technology (KIT), Karlsruhe, 2014
- Lisa-Mareike Busch, *Modeling of the elastomechanical properties of radio-frequency ablation scars: influence of different lesion patterns on cardiac contraction*, Bachelor Thesis, Institute of Biomedical Engineering, Karlsruhe Institute of Technology (KIT), Karlsruhe, 2012
- Jan Richter, *Modeling the tension development and the active contraction of the human atria*, Diplom Arbeit, Institute of Biomedical Engineering, Karlsruhe Institute of Technology (KIT), Karlsruhe, 2012
- Mesud Zaimovic, *In silico analysis of the velocity vector field of the human ventricles and comparison with PC-MRI data*, Bachelor Thesis, Institute of Biomedical Engineering, Karlsruhe Institute of Technology (KIT), Karlsruhe, 2012

Awards

- DGBMT Student Award 2008 for *Adapting a Mass-Springsystem to energy density function describing myocardial mechanic*
- Poster Prize Winner, 2012 Cardiac Physiome Workshop, San Diego, California, USA for *Finite Element Analysis of the Contraction of the Heart within the Pericardium: A Frictionless Contact Problem*

